

東京都立大学 博士（理学）学位論文（課程博士）

論文名

Theoretical study on self-propulsion and state transition of micromachines
マイクロマシンの自己推進と状態遷移に関する理論的研究（英文）

著者

安田 健人

審査担当者

主査	准教授	好村 滋行	好村 滋行
委員	教授	伊藤 隆	伊藤 隆
委員	教授	竹川 暢之	竹川 暢之
委員	准教授	兒玉 健	兒玉 健

上記の論文を合格と判定する

年 月 日

東京都立大学大学院理学研究科教授会

研究科長

**DISSERTATION FOR A DEGREE OF
DOCTOR OF PHILOSOPHY IN SCIENCE
TOKYO METROPOLITAN UNIVERSITY**

TITLE :

Theoretical study on self-propulsion and state transition of micromachines

AUTHOR :

Kento Yasuda

EXAMINED BY

Examiner in chief

Associate Professor Shigeyuki Komura

S. Komura

Examiner

Professor Yutaka Ito

Yutaka Ito

Examiner

Professor Nobuyuki Takegawa

Nobuyuki Takegawa

Examiner

Associate Professor Takeshi Kodama

T. Kodama

**QUALIFIED BY THE GRADUATE SCHOOL OF SCIENCE
TOKYO METROPOLITAN UNIVERSITY.**

Dean

Date

Theoretical study on self-propulsion and state transition of micromachines

マイクロマシンの自己推進と状態遷移
に関する理論的研究（英文）

By

Kento Yasuda

Under the Supervision of

Associate Professor Shigeyuki Komura

A Thesis Submitted in Fulfilment of Requirements for
the Degree of Doctor of Philosophy in Science of
Tokyo Metropolitan University



TOKYO METROPOLITAN UNIVERSITY

東京都立大学

Department of Chemistry, Faculty of Science
Tokyo Metropolitan University

March 2021

Abstract

Theoretical study on self-propulsion and state transition of micromachines

(邦題) : マイクロマシンの自己推進と状態遷移に関する理論的研究 (英文)

Kento Yasuda

Micromachines are tiny machines, such as motor proteins, metabolic enzymes or motile bacteria. All of the micromachines show net functions in overdamped situations, and are expected to be relevant to microfluidics and microsystems. By transforming chemical energy into mechanical work, micromachines show various non-equilibrium behaviors. Recently, these behaviors have attracted great interests both experimentally and theoretically.

First, I discuss the locomotion of a three-sphere microswimmer in a viscoelastic medium and propose a new type of active microrheology. I derive a relation that connects the average swimming velocity and the frequency-dependent viscosity of the surrounding medium. In this relation, the viscous contribution can exist only when the time-reversal symmetry is broken, whereas the elastic contribution is present only when the structural symmetry of the swimmer is broken. Purcell's scallop theorem should be generalized for a three-sphere swimmer in a viscoelastic medium.

Next, I propose a model of three-disk micromachine swimming in a quasi two-dimensional supported membrane. I calculate the average swimming velocity as a function of the disk size and the arm length. Due to the presence of the

hydrodynamic screening length in the quasi two-dimensional fluid, the geometric factor appearing in the average velocity exhibits three different asymptotic behaviors depending on the microswimmer size and the hydrodynamic screening length. This is in sharp contrast with a microswimmer in a three-dimensional bulk fluid that shows only a single scaling behavior. The intrinsic drag of the disks on the substrate does not alter the scaling behaviors of the geometric factor.

Then I discuss the locomotion of a three-sphere microswimmer in a viscoelastic structured fluid characterized by typical length and time scales. I derive a general expression to link the average swimming velocity to the sphere mobilities. In this relationship, a viscous contribution exists when the time-reversal symmetry is broken, whereas an elastic contribution is present when the structural symmetry of the microswimmer is broken. As an example of a structured fluid, I consider a polymer gel, which is described by a “two-fluid model”. I demonstrate in detail that the competition between the swimmer size and the polymer mesh size gives rise to the rich dynamics of a three-sphere microswimmer.

After that, I discuss the dynamics of a generalized three-sphere microswimmer in which the spheres are connected by two elastic springs. The natural length of each spring is assumed to undergo a prescribed cyclic change. I analytically obtain the average swimming velocity as a function of the frequency of cyclic change in the natural length. In the low-frequency region, the swimming velocity increases with frequency, and its expression reduces to that of the original three-sphere model. Conversely, in the high-frequency region, the average velocity decreases with increasing frequency. Such behavior originates from the intrinsic spring relaxation dynamics of an elastic swimmer moving in a viscous fluid.

In the latter part of the thesis, I propose a model that describes cyclic state transitions of a micromachine driven by a chemical reaction. I consider the dynamics of variables representing the degree of chemical reaction and the state

of a micromachine. The total free energy of the system is the sum of the tilted periodic potential and the periodic coupling energy. I assume that the reaction variable obeys a deterministic stepwise dynamics characterized by two characteristic times: the mean first passage time and the mean first transition path time. To quantify the functionality of a micromachine, I introduce a physical quantity called “state cyclone” and further discuss its dependency on the properties of the chemical reaction. For example, I show that the state cyclone is proportional to the square of the mean first transition path time. The explicit calculation of these time scales reveals that the state cyclone is inversely proportional to the square of the activation energy of the chemical reaction.

Finally, with the use of the “two-fluid model”, I discuss anomalous diffusion induced by active micromachines in viscoelastic media. Micromachines, such as proteins and bacteria, generate non-thermal fluctuating flows that lead to a substantial increment of the diffusion. Using the partial Green’s function of the two-fluid model, I calculate active (non-thermal) one-point and two-point correlation functions due to active force dipoles. The time correlation of a force dipole is assumed to decay exponentially with a characteristic time scale. I show that the active component of the displacement cross-correlation function exhibits various crossovers from super-diffusive to sub-diffusive behaviors depending on the characteristic time scales and the particle separation.

List of Papers

- K. Yasuda and S. Komura, State cyclone of a micromachine driven by catalytic reaction, arXiv preprint arXiv:2011.14273 (2020).
- K. Era, Y. Koyano, Y. Hosaka, K. Yasuda, H. Kitahata, and S. Komura, Autonomous elastic microswimmer, arXiv preprint arXiv:2010.03210 (2020), to be published in EPL.
- I. Sou, Y. Hosaka, K. Yasuda, and S. Komura, Irreversibility and entropy production of a thermally driven micromachine, Physica A **562**, 125277 (2021).
- K. Yasuda, M. Kuroda, and S. Komura, Reciprocal microswimmers in a viscoelastic fluid, Phys. Fluids **32**, 093102 (2020).
- C.-C. Liang, K. Yasuda, S. Komura, K.-A. Wu, and H.-Y. Chen, Dynamics of a membrane coupled to an active fluid, Phys. Rev. E **101**, 042601 (2020).
- I. Sou, Y. Hosaka, K. Yasuda, and S. Komura, Non-equilibrium probability flux of a thermally driven micromachine, Phys. Rev. E **100**, 022607 (2019).
- M. Kuroda, K. Yasuda, and S. Komura, Hydrodynamic interaction between two elastic microswimmers, J. Phys. Soc. Jpn. **88**, 054804 (2019).
- K. Yasuda, R. Okamoto, and S. Komura, A three-sphere microswimmer in a structured fluid, EPL **123**, 34002 (2018).

-
- Y. Ota, Y. Hosaka, K. Yasuda, and S. Komura, Three-disk microswimmer in a supported fluid membrane, *Phys. Rev. E* **97**, 052612 (2018).
 - K. Yasuda, R. Okamoto, S. Komura, and J.-B. Fournier, Dynamics of a bilayer membrane with membrane-solvent partial slip boundary conditions, *Soft Materials* **16**, 186-191 (2018).
 - T. V. Sachin Krishnan, K. Yasuda, R. Okamoto, and S. Komura, Thermal and active fluctuations of a compressible bilayer vesicle, *J. Phys.: Condens. Matter* **30**, 175101 (2018).
 - Y. Hosaka, K. Yasuda, I. Sou, R. Okamoto, and S. Komura, Thermally driven elastic micromachines, *J. Phys. Soc. Jpn.* **86**, 113801 (2017).
 - K. Yasuda, Y. Hosaka, M. Kuroda, R. Okamoto, and S. Komura, Elastic three-sphere microswimmer in a viscous fluid, *J. Phys. Soc. Jpn.* **86**, 093801 (2017).
 - Y. Hosaka, K. Yasuda, R. Okamoto, and S. Komura, Lateral diffusion induced by active proteins in a biomembrane, *Phys. Rev. E* **95**, 052407 (2017).
 - K. Yasuda, R. Okamoto, and S. Komura, Swimmer-microrheology, *J. Phys. Soc. Jpn.* **86**, 043801 (2017).
 - K. Yasuda, R. Okamoto, and S. Komura, Anomalous diffusion in viscoelastic media with active force dipoles, *Phys. Rev. E* **95**, 032417 (2017).
 - K. Yasuda, R. Okamoto, S. Komura, and A. S. Mikhailov, Localization and diffusion of tracer particles in viscoelastic media with active force dipoles, *EPL* **117**, 38001 (2017).
 - K. Yasuda, S. Komura, and R. Okamoto, Dynamics of a membrane interacting with an active wall, *Phys. Rev. E* **93**, 052407 (2016).

- S. Komura, K. Yasuda, and R. Okamoto, Dynamics of two-component membranes surrounded by viscoelastic media, *J. Phys.: Condens. Matter* **27**, 432001 (2015).

Acknowledgements

First of all, I deeply would like to express thankful to my supervisor, Professor Shigeyuki Komura, for his generous support, advice, foresight and guidance. I have greatly benefitted from his incredible insight, intuition and knowledge. I also would like to thank Professor Tadashi Kato for his great perspective. In addition, I would especially like to thank my collaborators: Dr. Ryuichi Okamoto from Okayama University (Japan), Professor Alexander S. Mikhailov from Kanazawa University (Japan), and Professor Jean-Baptiste Fournier from Université Paris Diderot (France). Finally, I wish to thank my parents and all laboratory members for their support and encouragement throughout my study. This work was supported by JSPS Research Fellowship for Young Scientists (18J21231).

Contents

Abstract	i
List of Papers	iv
Acknowledgements	vii
1 General Backgrounds	1
1.1 Introduction	1
1.1.1 General properties of micromachines	1
1.1.2 Energetics of motor proteins	4
1.1.3 Diffusion enhancement of metabolic enzymes	5
1.1.4 Microswimmers	6
1.2 Basic concepts for micromachines	8
1.2.1 Non-equilibrium statistical mechanics and thermal fluctuations	8
1.2.2 Continuum mechanics	10
1.2.3 Viscoelastic fluids	11
1.2.4 Microrheology	13
1.3 Theory of microswimmers	14
1.3.1 Scallop theorem	14
1.3.2 Gauge theory for a microswimmer	14
1.3.3 Previous models for microswimmers	15
1.3.4 Three-sphere microswimmer	16

1.4	Purpose of the thesis	18
	References	21
2	Three-Sphere Microswimmer in a Homogeneous Viscoelastic Fluid	25
2.1	Introduction	25
2.2	Model	26
2.3	Results	29
2.4	Summary and discussion	32
	Appendix 2.A Derivation of Eq. (2.14)	33
	References	35
3	Three-Disk Microswimmer in a Two-Dimensional Fluid	37
3.1	Introduction	37
3.2	Mobilities in a two-dimensional fluid	40
3.3	Three-disk microswimmer	43
3.4	Geometric factor	44
3.5	Asymmetric microswimmers	48
3.6	Summary and discussion	50
	References	52
4	Three-Sphere Microswimmer in a Structured Fluid	55
4.1	Introduction	55
4.2	Microswimmer in a structured fluid	58
4.3	Two-fluid model for a gel	60
4.4	Average velocities in a two-fluid gel	62
4.5	Summary and discussion	66
	Appendix 4.A Derivation of Eq. (4.3)	68
	Appendix 4.B Mobilities in a two-fluid polymer gel	70
	Appendix 4.C Asymptotic expressions of the average velocity	72

References	74
5 Elastic Three-Sphere Microswimmer in a Viscous Fluid	77
5.1 Introduction	77
5.2 Model	80
5.3 Results	82
5.4 Summary and discussion	87
References	87
6 State Transition of a Micromachine Driven by Catalytic Reaction	89
6.1 Introduction	90
6.2 Model	92
6.3 Dynamics of the state variable	95
6.4 State cyclone of a micromachine	98
6.5 Two characteristic time scales	99
6.5.1 Mean first passage time τ_p	100
6.5.2 Mean first transition path time τ_t	102
6.6 Summary and discussion	104
Appendix 6.A Derivation of Eqs. (6.16) and (6.17)	106
Appendix 6.B Derivation of Eq. (6.22)	107
Appendix 6.C Derivation of Eq. (6.28)	108
References	110
7 Anomalous Diffusion Induced by Micromachines in a Structured Fluid	113
7.1 Introduction	114
7.2 Two-fluid model	117
7.2.1 Model description	117
7.2.2 Partial Green's function	119

7.2.3	Asymptotic expressions	120
7.2.4	Coupling mobilities	121
7.3	Passive two-point correlation functions	121
7.3.1	Fluctuation dissipation theorem	122
7.3.2	Large distance behaviors	125
7.4	Active one-point correlation functions	125
7.4.1	Velocity induced by active force dipoles	126
7.4.2	Active auto-correlation functions	127
7.4.3	Uncorrelated force dipoles	129
7.4.4	Exponentially correlated force dipoles	131
7.5	Active two-point correlation functions	132
7.5.1	Velocity cross-correlation functions	132
7.5.2	Displacement cross-correlation functions	133
7.6	Summary and discussion	135
Appendix 7.A	Partial Green's function	140
Appendix 7.B	Derivation of Eq. (7.34)	141
Appendix 7.C	Full expression of Eq. (7.42)	143
References	143
8	Concluding Remarks	149

Chapter 1

General Backgrounds

1.1 Introduction

1.1.1 General properties of micromachines

Micromachine is a general term for tiny objects that perform a net mechanical function and correspond to biological matter and objects as discussed below. F1-ATPase is known as an ATP synthase whose size is about 10 nm [1.1, 1.2]. It exists in cell membranes and plays a role of synthesizing ATP using a proton concentration gradient and membrane potential. On the other hand, F1-ATPase has a function to catalyze ATP decomposition, just as a general enzyme catalyzes both the forward and the reverse reactions. Here, it is known that the axis of F1-ATPase rotates 120° each time when a single ATP molecule is produced. Such a dynamics has attracted many attentions. Therefore, F1-ATPase is called a rotary motor protein and is one of the subjects of micromachine research.

On the other hand, a group of proteins called kinesin is a rod-shaped protein with a size of 100 nm [1.1, 1.2]. This protein is responsible for intracellular substance transport by moving in one direction on microtubules. Kinesin catalyzes the hydrolysis of one ATP molecule, and undergoes a step-wise motion (about 10 nm/step) during this process. Kinesin has also attracted many attentions as a typical micromachine called as a linear motor protein.

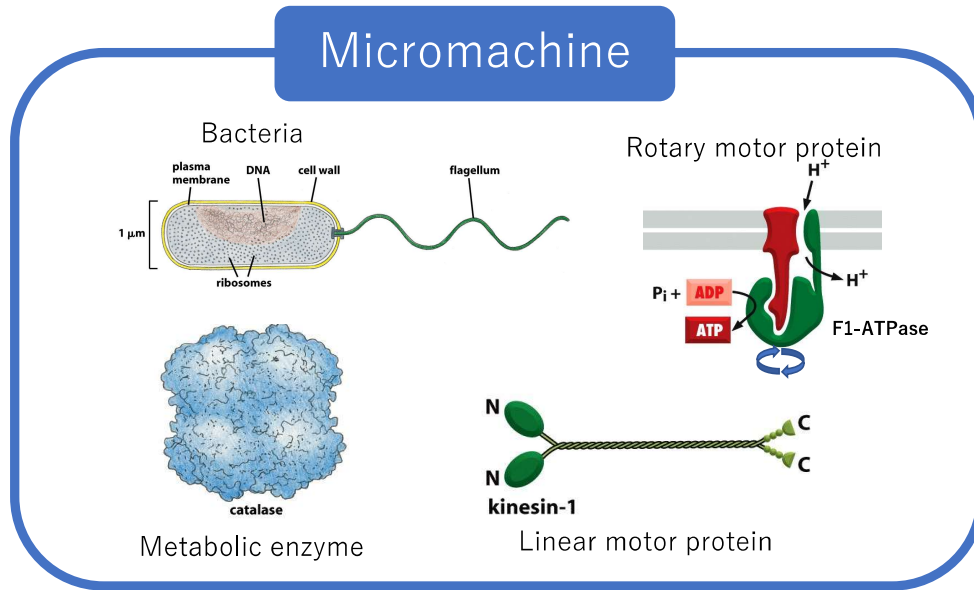


Figure 1.1: Objects and substances targeted by micromachines. Rotating motor proteins such as F1-ATPase, linear motor proteins such as kinesin, metabolic enzymes such as catalase, and microorganisms such as bacteria. Figures are taken from Ref. [1.1].

Moreover, metabolic enzymes such as catalase, that are considered not to have a mechanical function, are also studied as micromachines. Metabolic enzymes play a role in regulating the concentration of chemical substances in cells and maintaining homeostasis. On the other hand, it is known that the structural change of metabolic enzymes is large in the process of catalyzing a chemical reaction [1.1, 1.2], and the mechanical properties associated with this structural change has attracted many attentions.

Furthermore, larger microorganisms with more complicated internal structures can also be treated as micromachines when they swim in viscous fluids. For example, *E. coli* has a size of about $1 \mu\text{m}$ and can swim in water with a speed of about $10 \mu\text{m/s}$ using flagella [1.1, 1.2]. Although their size is 100 times larger than that of micromachines such as enzymes, it is expected that there is something in common both in the hydrodynamic and statistical behaviors.

When we investigate micromachines, we try to extract a universal mechanism of motion by focusing on the mechanical functions of various materials as

described above (Fig. 1.1). Therefore, it is important to consider the physical properties and problems that are universally present in micromachines. For this purpose, I shall briefly describe energetics, fluctuations, hydrodynamics effects, and Brownian ratchets.

Energy supply is essential for micromachines to perform a net function. Energy source varies depending on the micromachine, but most of them use chemical energy. Similar to macroscopic machines, part of the supplied energy is used for mechanical functions, and the rest is dissipated as heat. Hence, energy efficiency can also be discussed for micromachines. In recent years, owing to the progress of the fundamental theory of non-equilibrium statistical mechanics and experimental techniques, the efficiency of micromachines has been measured. It was shown that the efficiency of F1-ATPase is almost 100% [1.3], while that of kinesin is only about 20% [1.4].

Because micromachines are small, thermal fluctuations due to the surrounding molecules cannot be ignored. Moreover, since micromachines always operate in a non-equilibrium environment, they are also affected by non-thermal fluctuations. Hence, it is necessary to take into account these fluctuations when we discuss the dynamics of micromachines. Especially, the mechanism for showing a net mechanical function in the presence of strong fluctuations is interesting, and its relation to the fluctuation control and information processing is important. It has been discussed that fluctuations can be actively used as a power source, which is generally called a Brownian ratchet [1.5]. Note that Feynman's impeller is one of the well-known examples of a Brownian ratchet.

Many micromachines operate in viscous fluids and the surrounding fluid plays useful roles for their dynamics. Important examples are hydrodynamic interactions within a micromachine and between multiple micromachines, or energy dissipation due to hydrodynamic friction. Micromachines change their structure owing to their mechanical function. Hence, we need to consider a hydrodynamic problem with time-dependent boundary conditions, which requires a non-linear

analysis. In recent years, not only homogeneous viscous fluids but also fluids showing complex mechanical responses such as viscoelastic fluids or structural fluids have been discussed [1.6].

1.1.2 Energetics of motor proteins

In 2005, Harada and Sasa proposed a relation connecting the breakdown of the fluctuation dissipation theorem and energy dissipation [1.7], which provides with a framework of how to experimentally discuss energetics. After the theory was proposed, Toyabe *et al.* performed an energy analysis of F1-ATPase in 2010 [1.3] and Ariga *et al.* performed an energy analysis of kinesin in 2018 [1.4].

According to the statistical mechanics, fluctuation-dissipation theorem holds between the response due to an external force and fluctuation in thermal equilibrium. However, fluctuation dissipation theorem does not always hold when the system is in a non-equilibrium state. This has been experimentally confirmed by measuring fluctuations of microparticles introduced into cells [1.8]. Therefore, many attempts to quantitatively evaluate the non-equilibrium properties have been performed by analyzing how the fluctuation dissipation theorem breaks down. Harada and Sasa proposed a relation showing that the breakdown of the fluctuation dissipative theorem corresponds to the steady energy dissipation rate of the system [1.7].

In recent years, using Harada-Sasa equation, Ariga *et al.* performed an analysis of kinesin which is a motor protein moving linearly on microtubules. Microparticles were bound to the kinesin molecule and the translational motion of kinesin was measured as in Fig. 1.2. It was found that the fluctuation dissipation theorem breaks down at low frequencies in the presence of ATP. The energy dissipated by the translational motion was estimated from this measurement. It was found that only 20% of the chemical energy obtained by hydrolyzing ATP was dissipated by the translational motion and the non-equilibrium translational diffusion, although the usage of the remaining 80% was not specified. This result is very different from that of F1-ATPase. Ariga *et al.* pointed out that energy

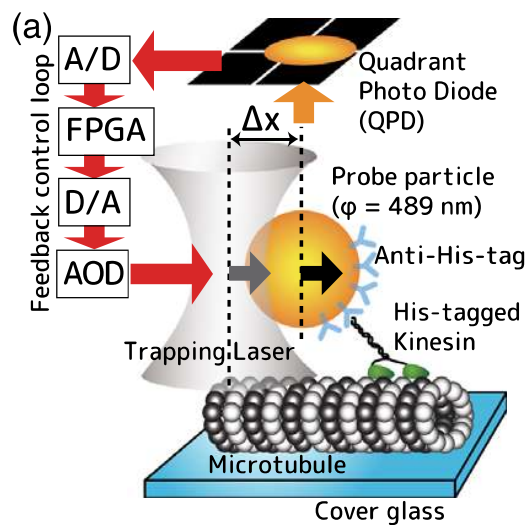


Figure 1.2: Experiments for energy analysis of kinesin. The probe is bound to kinesin and the movement of the probe is analyzed. In particular, they measure fluctuations and responses to external forces when the probe is moving freely, and quantify the violation of the fluctuation-dissipation theorem. Figure is taken from Ref. [1.4].

may be dissipated due to structural changes in kinesin that cannot be extracted in this experiment.

1.1.3 Diffusion enhancement of metabolic enzymes

In recent years, experiments have been conducted to measure the self-diffusion coefficient of metabolic enzymes. There are several works which reported that the diffusion coefficient increases due to the presence of substrate molecules [1.9–1.11].

Since the discovery of the increased diffusion of enzymes, similar experiments have been conducted. Riedel *et al.* measured the diffusion coefficient for various types of enzyme-substrate systems to investigate the conditions under which the increase takes place. Figure 1.3 is a plot of the diffusion coefficient against the reaction rate [(a) catalase, (b) urease, (c) alkaline phosphatase, and (d) triose phosphate isomerase].

The diffusion coefficient of most enzymes increases in proportion to the reaction rate, while no increase in diffusion was observed for triose phosphate

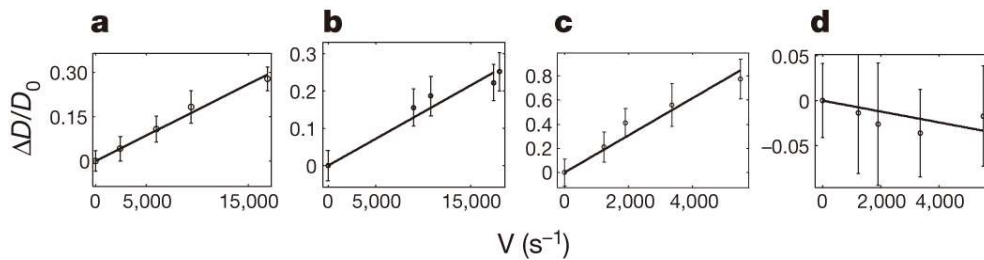


Figure 1.3: Types of enzymes and increased diffusion. The reaction rate is plotted on the horizontal axis, and the magnitude of diffusion increase is plotted on the vertical axis. The results of the enzymes of (a) catalase, (b) urease, (c) alkaline phosphatase and (d) triose phosphate isomerase are shown. It can be seen that in (a), (b) and (c), the diffusion increase is observed in proportion to the reaction rate, but in (d), the diffusion increase is not observed. Figure is taken from Ref. [1.11].

isomerase in (d). Riedel *et al.* argued that an exothermic reaction is important for the increased diffusion [1.11].

On the other hand, Illien *et al.* claimed that an exothermic reaction is not always necessary, and an increase in diffusion was also observed in an enzyme-substrate system showing an endothermic reaction [1.12]. Since different claims have been made in multiple experiments, the actual mechanism has not yet been clarified. Several theoretical mechanisms have been proposed for these observations, but none of them are conclusive yet [1.12–1.14].

When an enzyme catalyzes a chemical reaction, the structure is changed so that it can be treated as a micromachine. It has been pointed out that enzymes can stochastically swim in a viscous fluid due to stochastic structural changes following a chemical reaction. It was suggested that the enzyme shows a ballistic motion, and stochastic swimming is considered to be one of the leading mechanisms [1.15].

1.1.4 Microswimmers

E. coli swim in water by deforming a tail-like organ called flagella. On the other hand, *Paramecium* has a hair-like organ called cilia that covers the body surface, and it can swim by beating cilia. In this way, many microorganisms

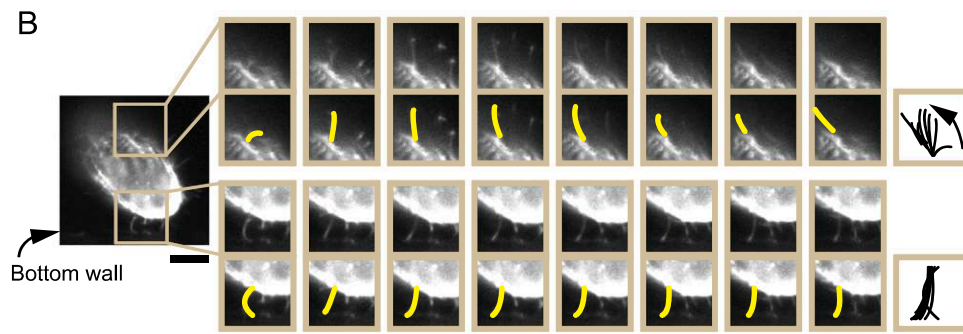


Figure 1.4: Ciliary movement of a ciliate that slides near the wall. The upper row shows the ciliary movement of the body surface that is not in contact with the wall. We can see that the cilia are moving with a large stroke. The lower row shows the ciliary movement of the body surface in contact with the wall. Here, it can be seen that the movement of the cilia is significantly weakened and hardly moves. Figure is taken from Ref. [1.16].

can swim freely in water and are regarded as microswimmers. The concept of microswimmer can be used not only to microorganisms but also to objects and molecules that can move autonomously in fluids using their shape deformation. Therefore, the concept of micromachines can be applied to enzyme molecules in the living body. In recent years, many theoretical and experimental researches have been conducted.

For example, ciliates are known to swim in water using cilia distributed on the body surface. Their swimming behavior near the wall was investigated, and it was observed that they slid along the wall [1.16]. The ciliates touch the wall at an average angle of 13° and slid in a stable way. A more detailed observation revealed that the movement of the cilia in contact with the wall was significantly reduced, as shown in Fig. 1.4, suggesting that it is responsible for the sliding motion on the surface wall.

The physical mechanism of swimming and photoresponse of spherical green alga *Volvox* has also been investigated. A *Volvox* is phototactic when swimming in water and is known to swim in the direction of the light. The relationship between the random walk of a *Volvox* in the absence of light and the response to the light has been investigated. It was found that there is a linear relation be-

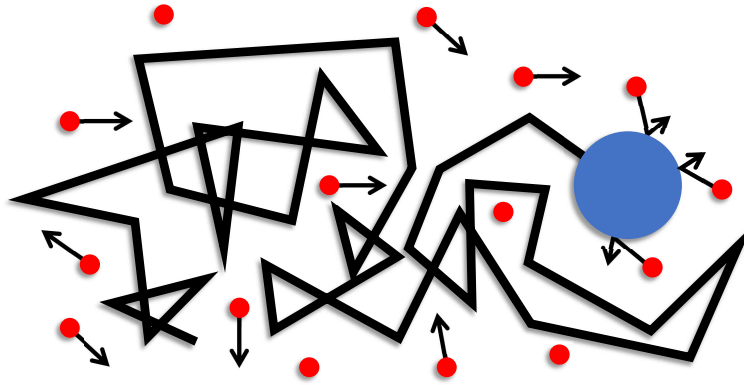


Figure 1.5: Schematic picture of Brownian motion. The blue sphere represents a microparticle and brownian motion in a trajectory like a black line. Brownian motion occurs when surrounding medium molecules (red circles) collide with the microparticle.

tween them. In other words, for Volvox showing large fluctuations, the response to light becomes stronger [1.17].

1.2 Basic concepts for micromachines

1.2.1 Non-equilibrium statistical mechanics and thermal fluctuations

Converting chemical energy to mechanical energy, micromachines exhibit functions such as propulsion. Hence, the system that contains micromachines is essentially non-equilibrium, and the framework of non-equilibrium statistical mechanics that goes beyond equilibrium statistical mechanics is required. Therefore, the introduction of non-equilibrium statistical mechanics is briefly discussed in this section.

First, I discuss thermal fluctuation and Brownian motion (shown in Fig. 1.5) as the simplest subject of non-equilibrium statistical mechanics. In a macroscopic state, even if the system is in thermal equilibrium and behaves stationary, molecules and micro objects continue to move microscopically. These motions should be described deterministically by the equations of motion, but a huge number of variables results in a random situation. These small scale motions

are treated as random thermal fluctuations, and their properties have been investigated.

The Brownian motion of particles is famous as the phenomenon in which this thermal fluctuation can be observed directly. Here the surrounding solvent molecules randomly collide with small particles, causing random motions. The coordinate of the center of mass of the particle, $x(t)$, is used in the Langevin equation as follows [1.18]

$$m\dot{v} = -\zeta v + \xi(t), \quad (1.1)$$

where m is the mass, v is the velocity defined as $v = \dot{x} = dx/dt$, ζ is the drag coefficient, ξ is the random force due to thermal fluctuations.

The statistical property of random force can be written as

$$\langle \xi(t)\xi(0) \rangle = 2\zeta^2 D \delta(t), \quad (1.2)$$

where the bracket indicates the statistical average, $\delta(t)$ is delta function and D is diffusion constant which fixes the magnitude of the fluctuation. The diffusion constant is estimated from the mean squared displacement (MSD), i.e., $\langle [x(t) - x(0)]^2 \rangle$. By solving the Langevin equation, MSD can be given by $\langle [x(t) - x(0)]^2 \rangle = 2Dt$. The diffusion constant D in thermal equilibrium state is determined by the fluctuation dissipation theorem which relates the fluctuation (Brownian motion) and the dissipation (response). The Einstein's relation is the simplest fluctuation dissipation theorem, which can be written as [1.18]

$$D = \frac{k_B T}{\zeta}, \quad (1.3)$$

where $k_B T$ is the thermal energy of the system. Furthermore, we use the Stokes relation, which gives the drag coefficient of a particle with radius a in a viscous fluid of viscosity η , i.e., $\zeta = 6\pi\eta a$. The Stokes-Einstein relation can often be used to estimate the viscosity η of the surrounding fluid.

Next, we describe the framework of dealing with a non-equilibrium state slightly away from the equilibrium state. The thermal equilibrium with a con-

stant temperature is given as the state for which the free energy G is minimized. Consider a state in which the free energy is slightly shifted from the minimum one, and the system evolves so as to decrease the free energy. Since the deviation from the equilibrium state is small, one can assume that the time evolution can be described by a linear relation. This is called the linear response theory. Assuming that free energy G is dissipated by a frictional effect, we consider the following time evolution equation [1.18]

$$\dot{x} = -M \frac{dG}{dx}, \quad (1.4)$$

where M is the Onsager's coefficient. The above equation is called the Onsager's phenomenological equation and has been established as a method for describing the time evolution of non-equilibrium systems.

1.2.2 Continuum mechanics

Micromachines perform their functions in continuum media such as viscous fluids. In some of the mechanisms, the continuous field around micromachines plays an important role and requires a careful handling. In this subsection, I briefly describe pure viscous fluids, pure viscoelastic bodies, and viscoelastic bodies as the basis of continuum mechanics.

We consider a continuous body whose density ρ depends on time and space. Then the continuity equation $\dot{\rho} = -\partial_\alpha(\rho v_\alpha)$ is satisfied, where \mathbf{v} is the flow field of the continuum. The equation of motion is given as follows:

$$\rho(\dot{v}_\alpha + v_\beta \partial_\beta v_\alpha) = \partial_\beta \sigma_{\alpha\beta} + F_\alpha. \quad (1.5)$$

Here, σ is the stress and \mathbf{F} is an external body force. Since the flow is very slow in a system containing micromachines, the inertia term on the left side is often ignored. Then we have the following force balance equation [1.18]

$$0 = \partial_\beta \sigma_{\alpha\beta} + F_\alpha. \quad (1.6)$$

Here, the mechanical properties of the medium are expressed by the constitutive equations that gives the relationship between the stress and deformation.

For a pure viscous fluid, the following constitutive equation is satisfied [1.18]

$$\sigma_{\alpha\beta} = \eta(\partial_{\alpha}v_{\beta} + \partial_{\beta}v_{\alpha}) - p\delta_{\alpha\beta}, \quad (1.7)$$

where η and p indicate shear viscosity and pressure, respectively. In the case of an incompressible fluid (constant ρ), p is an unknown function. Then, the incompressibility condition ($\partial_{\alpha}v_{\alpha} = 0$) and the equation of motion derived from the continuity equation should be solved simultaneously.

For a pure elastic body, on the other hand, the following constitutive equation is satisfied [1.18]

$$\sigma_{\alpha\beta} = \mu(\partial_{\alpha}u_{\beta} + \partial_{\beta}u_{\alpha}) + \lambda\partial_{\gamma}u_{\gamma}\delta_{\alpha\beta}. \quad (1.8)$$

Here, \mathbf{u} represents the displacement field, μ and λ are the Lamé coefficients.

1.2.3 Viscoelastic fluids

Many materials around us do not exhibit uniform behavior such as viscous fluids and elastic bodies, but behave as viscoelastic fluids. For macromolecules, surfactants, biological substances, known as soft matter, viscoelastic behavior can be observed on a larger time scale.

Such viscoelastic fluids often exhibit a non-linear response to stress and strain, and the constitutive equation becomes complicated. Hence, the framework of linear viscoelasticity that deals with a linear response is widely used. This may also be described in various ways, but the following constitutive equation is often used as a uniform linear viscoelastic model [1.18],

$$\sigma_{\alpha\beta}(t) = \int_{-\infty}^t dt' \eta(t-t')[\partial_{\alpha}v_{\beta}(t') + \partial_{\beta}v_{\alpha}(t')] - p(t)\delta_{\alpha\beta}. \quad (1.9)$$

Here, $\eta(t)$ is the time-dependent viscosity, which reflects the mechanical properties of the viscoelastic fluid. In particular, $\eta[\omega]$ defined by $\eta[\omega] = \int_0^{\infty} dt \eta(t)e^{-i\omega t}$ is called the complex viscosity. The real part of the complex viscosity reflects the viscous component and the imaginary part reflects the elastic component. Here, the frequency dependence of $\eta[\omega]$ varies between the viscoelastic models.

In the well-known Maxwell model, for example, we assume the following ω

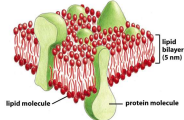
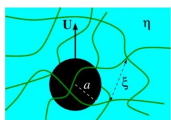
		Length scale	
		No	Yes
Time scale	No	Water 	Membrane 
	Yes	Viscoelastic 	Mesh Gel 

Figure 1.6: Examples of a continuum with an intermediate structure. There is a viscous fluid represented by water as a continuum having no intermediate structure. On the other hand, there are a uniform viscoelastic fluid having a time scale and a two-dimensional fluid having a screening length. Furthermore, a meshed gel is an example of a continuum having both time and space scales. The figure of membrane is taken from Ref. [1.1]. The figure of mesh gel is taken from Ref. [1.6].

dependece [1.18]

$$\eta[\omega] = \eta_0 \frac{1 - i\omega\tau_M}{1 + \omega^2\tau_M^2}, \quad (1.10)$$

where η_0 is zero-frequency viscosity and τ_M is the relaxation time of the Maxwell model. The Maxwell model behaves as a viscous fluid at low frequencies $\omega\tau_M \ll 1$, and an elastic body at high frequencies $\omega\tau_M \gg 1$.

In a homogeneous viscoelastic fluids, switching between viscous and elastic behaviors occurs by changing the frequency such as the Maxwell model. This is because the viscoelastic body has a time scale called the relaxation time. Not only homogeneous viscoelastic fluids, but also continuous materials showing more complicated mechanical responses can be discussed. For example, a gel-like continuum has a length scale, such as the mesh size, which switches between elastic and viscous behaviors depending on the scale. Since the continuous material has such a spatial and temporal structure, the mechanical response becomes complicated. The behavior of these complex structured fluids, which are summarized in Fig. 1.6, can also be analyzed by considering constitutive

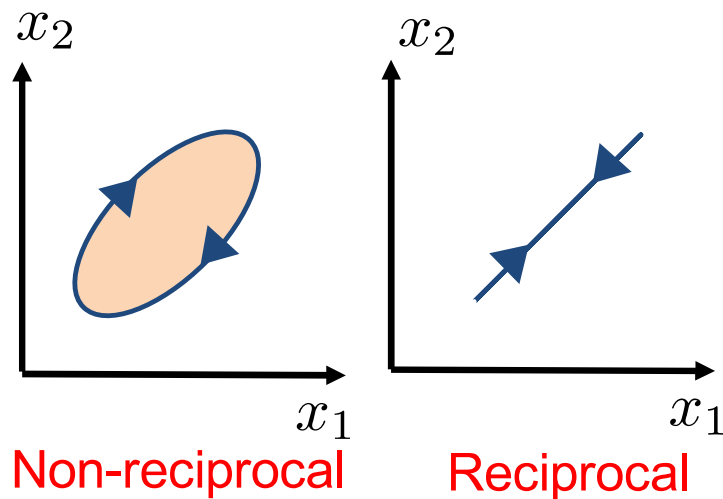


Figure 1.7: (a) Non-reciprocal motion in space of freedom degree of motions. (b) Reciprocal motion.

equations.

1.2.4 Microrheology

Microrheology is one of the most useful techniques for measuring the rheological properties of soft matter and various biological materials including cells [1.19, 1.20]. There are two different methods: passive microrheology and active microrheology. In passive microrheology, both the local and bulk mechanical properties of a medium can be extracted from the Brownian motion of a probe particle [1.21, 1.22]. In this method, the generalized Stokes–Einstein relation (GSER) is used to analyze thermal diffusive motion. In active microrheology, on the other hand, the probe is actively pulled through the fluid with the aims of driving the medium out of equilibrium and measuring mechanical responses [1.23, 1.24]. Within linear response theory, the generalized Stokes relation (GSR) is employed to obtain the frequency-dependent complex shear modulus.

1.3 Theory of microswimmers

1.3.1 Scallop theorem

Theoretical models for micromachines that swim in viscous fluids such as microorganisms has been considered before. When we consider the motion of microorganisms, it is important that one should consider the limit where the Reynolds number vanishes. The Reynolds number is given by the ratio of inertial force to viscous force, and it is about 10^4 for macroscopic swimmers like humans, but it is about 10^{-4} for microorganisms [1.25]. Since the Reynolds number is so small that it can be regarded as zero, a constraint called the Scallop theorem holds for the relation between the shape deformation and the swimming [1.25].

The Scallop theorem holds in a situation where the Reynolds number can be regarded as zero in a viscous fluid, and indicates that an object cannot be propelled by a reciprocal deformation [1.25, 1.26]. Here, the reciprocal deformation is a deformation that reciprocates on a curve in a shape space spanned by the shape variable \mathbf{s} as shown in the Fig. 1.7. On the other hand, the deformation that circulates the closed curve of the shape space is a non-reciprocal deformation, and there is a possibility of swimming even though the Scallop theorem is satisfied.

1.3.2 Gauge theory for a microswimmer

On the basis of the Scallop theorem, a relation using the gauge theory was proposed for the purpose of constructing a general framework for swimming theory [1.27]. The real space in which the swimming body is arranged and the shape space that describes the deformation of the swimming body are defined. Then, the dynamics in the real space is described by projecting the deformation in the shape space onto the real space. Information relation to swimming is included in the way of projection.

Under such situations, the average swimming speed \bar{V} can be expressed by

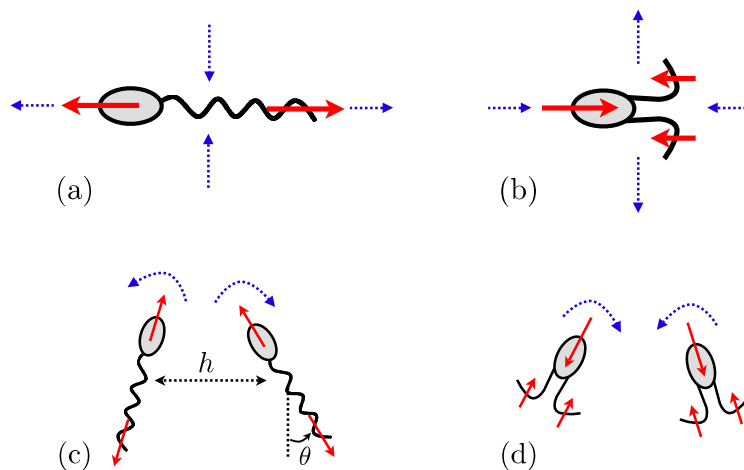


Figure 1.8: (a) Flow field around pusher. A flow field is formed that pushes the fluid in the direction of swimming. (b) Flow field around the puller. A flow field is formed that draws in the fluid in the direction of swimming. (c) Pusher-pusher fluid interaction which shows repulsive interactions. (d) Puller-puller fluid interaction which shows attractive interactions. Figure is taken from Ref. [1.28].

the line integral on the closed curve in the shape space:

$$\bar{V} \sim \oint ds \cdot \mathbf{A}. \quad (1.11)$$

Here \mathbf{A} is called the vector potential. There is a degree of freedom in the definition of the shape space, but the swimming speed should be uniquely determined regardless of the definition of the shape space. This is the expression derived from the gauge universality. The vector potential \mathbf{A} needs to be derived by solving the hydrodynamic equations. The swimming theory using the gauge theory is limited as a formal theory, and it is necessary to analyze the surrounding velocity field in order to investigate the specific swimming behavior.

1.3.3 Previous models for microswimmers

The squirmer model is well-known as a model for investigating the swimming behavior of ciliates [1.16]. In this model, the swimming phenomenon is reproduced by setting the flow field as the boundary condition on the surface of the rigid sphere or the rigid ellipsoidal sphere. Classifications such as puller and

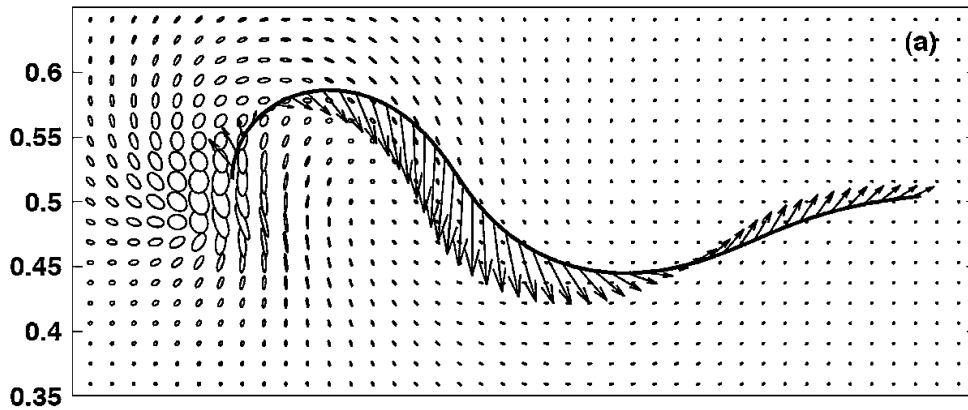


Figure 1.9: A sheet swimmer model that swims due to wavy deformation. It is used as a model for microswimmers that swim with flagella such as *E. coli*. Figure is taken from Ref. [1.30].

pusher are made according to the flow field, and the velocity field and interaction induced by each swimmer have been investigated [see also Fig. 1.8] [1.28].

Microorganisms that swim with flagella, such as *E. coli*, are treated as pushers. A pusher creates a flow field that pushes the fluid in the direction of swimming. As a result, pushers show a repulsive interaction with each other. On the other hand, microorganisms such as *Chlamydomonas* form a flow field called puller that draws in fluid in the direction of swimming. The pullers show an attractive interaction with each other.

A sheet swimmer model, shown in Fig. 1.9, was proposed to represent microswimmers using flagella such as *E. coli* [1.29, 1.30]. This is a model that can be propelled in a fluid by a wavy motion of a sheet-like object. It is necessary to consider the deformation of the object in detail. Hence, one needs to consider moving boundary conditions, and a non-linear analysis is required even for a linear fluid.

1.3.4 Three-sphere microswimmer

Several studies have been reported aiming at extracting the essence of swimming theory by constructing a minimum model of a microswimmer. As an example, I will describe a three-spheres swimmer model which is originally pro-

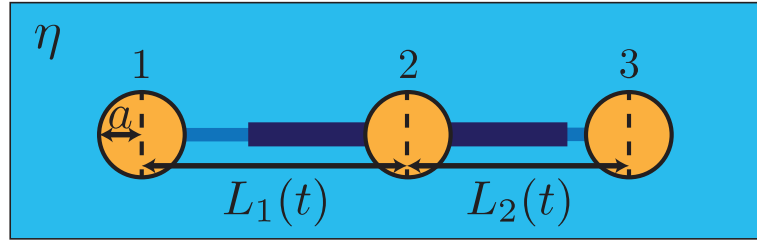


Figure 1.10: Najafi-Golestanian three-sphere swimmer model. Three identical spheres of radius a are connected by arms of lengths $L_1(t)$ and $L_2(t)$ and undergo time-dependent cyclic motion. The swimmer is embedded in a viscous fluid characterized by a shear viscosity η .

posed by Najafi and Golestanian and analyzed in detail by Golestanian and Ajdari [1.31, 1.32]. The three-spheres swimmer model is made up of three spheres that are linearly connected by two rigid arms as shown in Fig. 1.10. The rigid arms can deform mechanically, thereby swimming in the uniaxial direction. Since the deformation of the swimmer is determined by the expansion and contraction of the left and right arms, the deformation of the arms can be identified as the two shape variables. This model is suitable for analytical analysis because it is sufficient to consider only the translational motion, and the tensorial structure of the fluid motion can be neglected.

Let the lengths of the left and right arms be $L_1(t)$ and $L_2(t)$, respectively. The equation of the model can be written by considering the hydrodynamic friction acting on the spheres and the fluid interaction between the spheres. The equation of motion of each sphere can be written as follows

$$V_1 = \mu F_1 + G(L_1)F_2 + G(L_1 + L_2)F_3, \quad (1.12)$$

$$V_2 = G(L_1)F_1 + \mu F_2 + G(L_2)F_3, \quad (1.13)$$

$$V_3 = G(L_1 + L_2)F_1 + G(L_2)F_2 + \mu F_3. \quad (1.14)$$

Here, V_i represents the velocity of the i -th sphere, and F_i represents the force acting on the i -th sphere. The relation between the velocity and force is given by the mobility that characterizes the properties of the surrounding fluid.

There are two types of mobility, $\mu = (6\pi\eta a)^{-1}$, $G(x) = (4\pi\eta x)^{-1}$, and they

are called the self mobility and coupling mobility, respectively. Since no external force is acting, the force free condition $F_1 + F_2 + F_3 = 0$ must be satisfied. In addition, it is assumed that the expansion and contraction of the arm can be described by the deviation from the natural length ℓ , i.e., $L_i(t) = \ell + u_i(t)$ where $\ell \gg u_i$. The average swimming speed of the swimmer is calculated under these conditions and the condition $a \ll \ell$. Then we obtain the original result shown by Golestanian and Ajdari as [1.31, 1.32]

$$\bar{V} = (V_1 + V_2 + V_3)/3 \approx \frac{7a}{12\ell^2 T} \int_0^T dt \dot{u}_1 u_2. \quad (1.15)$$

Here, T represents the period of deformation. By giving the time dependence of arm expansion and contraction $u_1(t), u_2(t)$, integration can be performed to obtain the swimming speed. For example, when $u_1(t) = d_1 \cos(\Omega t)$ and $u_2(t) = d_2 \cos(\Omega t - \phi)$, we have

$$\bar{V} = \frac{7d_1 d_2 a \Omega}{24\ell^2} \sin \phi. \quad (1.16)$$

Since the swimming speed is proportional to $\sin \phi$, the phase difference between the left and right arm expansion and contraction determines the swimming speed. The three-spheres swimmer model has been experimentally reproduced by controlling the magnetic particles with an external magnetic field [1.33].

1.4 Purpose of the thesis

The purpose of micromachine study is to extract universal properties of micromachines. In this thesis, I explore the universal properties of micromachines by considering the propulsion mechanism in the structured fluid of the micromachine and the state transition of the micromachine. For this purpose, I consider the minimum models of a micromachine such as three-sphere microswimmer and force-dipole, etc. Results of the minimum models can be applied to the many concrete objects. Hence, the understanding of the minimum model leads to the universal properties of a micromachine.

In Chaps. 2, 3, and 4, I discuss a three-sphere microswimmer as a minimum

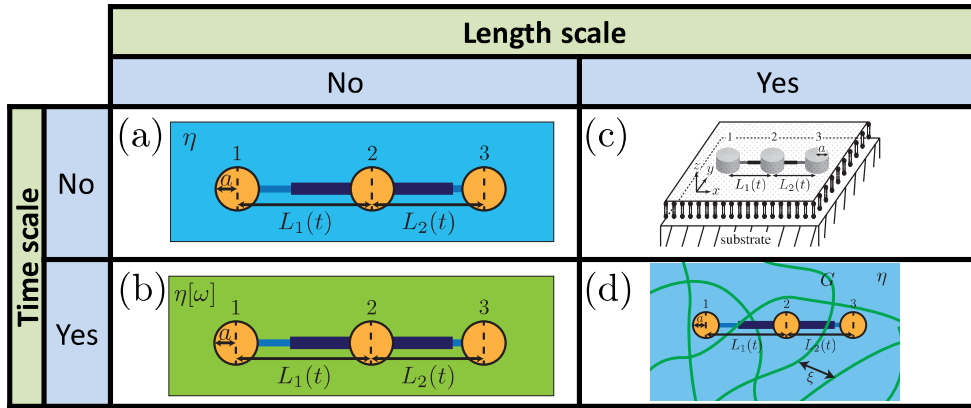


Figure 1.11: Three-spheres swimmer in various structured fluids. (a) Swimmer is in a viscous fluid as a continuum having no intermediate structure. (b) Swimmer in a uniform viscoelastic fluid having a time scale and (c) a two-dimensional fluid having a screening length. (d) Swimmer in mesh gel which is an example of a continuum having both time and space scales.

model of microswimmer and its swimming behavior in a fluid which include time and/or length scales. In Chap. 5, I develop the elastic three-sphere microswimmer as one of the minimum model of microswimmer and discuss its viscoelastic behavior induced by the intrinsic spring relaxation dynamics of an elastic swimmer. In Chap. 6, I suggest a minimum model that describes cyclic state transitions of a micromachine driven by a chemical reaction. In Chap. 7, I discuss anomalous diffusion induced by force-dipole which is the minimum models of micromachine. Purpose of each chapter is described below.

In Chap. 2, I discuss the propulsion of a three-sphere microswimmer in a viscoelastic fluid. I derive a relation that connects the average swimming velocity and the frequency-dependent viscosity of the surrounding medium.

In Chap. 3, a model of three-disk micromachine swimming in a quasi two-dimensional supported membrane is proposed. The hydrodynamic screening length is presence in the quasi two-dimensional fluid as intermediate length scale. I calculate the average swimming velocity as a function of the disk size and the arm length.

In Chap. 4, I discuss the locomotion of a three-sphere microswimmer in a

viscoelastic structured fluid characterized by typical length and time scales. I derive a general expression to link the average swimming velocity to the sphere mobilities. As an example of a structured fluid, I consider a polymer gel, which is described by a “two-fluid model”. Researches in Chaps. 2, 3, and 4 are summarized in Fig. 1.11.

In Chap. 5, I discuss the dynamics of a generalized three-sphere microswimmer in which the spheres are connected by two elastic springs. The natural length of each spring is assumed to undergo a prescribed cyclic change. I analytically obtain the average swimming velocity as a function of the frequency of cyclic change in the natural length.

In Chap. 6, I propose a model that describes cyclic state transitions of a micromachine driven by a chemical reaction. I consider the dynamics of variables representing the degree of chemical reaction and the state of a micromachine. The total free energy of the system is the sum of the tilted periodic potential and the periodic coupling energy. To quantify the functionality of a micromachine, I introduce a physical quantity called “state cyclone” and further discuss its dependency on the properties of the chemical reaction.

In Chap. 7, with the use of the “two-fluid model”, I discuss anomalous diffusion induced by active force dipoles in viscoelastic media. Active force dipoles, such as proteins and bacteria, generate non-thermal fluctuating flows that lead to a substantial increment of the diffusion. I calculate active (non-thermal) one-point and two-point correlation functions due to active force dipoles. The time correlation of a force dipole is assumed to decay exponentially with a characteristic time scale.

Finally, in Chap. 8, I summarize this thesis and discuss the universal property of micromachines from a physical and chemical point of view.

References

- [1.1] B. Alberts, A. Johnson, P. Walter, J. Lewis, and M. Raff, *Molecular Biology of the Cell* (Garland Science, New York, 2008).
- [1.2] R. Phillips, J. Kondev, J. Theriot, and H. G. Garcia, *Physical Biology of the Cell* (Garland Science, New York, 2013).
- [1.3] S. Toyabe, T. Okamoto, T. Watanabe-Nakayama, H. Taketani, S. Kudo, and E. Muneyuki, *Phys. Rev. Lett.* **104**, 198103 (2010).
- [1.4] T. Ariga, M. Tomishige, and D. Mizuno, *Phys. Rev. Lett.* **121**, 218101 (2018).
- [1.5] K. Sekimoto, *Stochastic Energetics* (Springer, Berlin Heidelberg, 2010).
- [1.6] H. Diamant, *Eur. Phys. J. E* **38**, 32 (2015).
- [1.7] T. Harada and S. Sasa, *Phys. Rev. Lett.* **95**, 130602 (2005).
- [1.8] D. Mizuno, C. Tardin, C. F. Schmidt, and F. C. MacKintosh, *Science* **315**, 370-373 (2007).
- [1.9] H. S. Muddana, S. Sengupta, T. E. Mallouk, A. Sen, and P. J. Butler, *J. Am. Chem. Soc.* **132**, 2110 (2010).
- [1.10] S. Sengupta, K. K. Dey, H. S. Muddana, T. Tabouillot, M. E. Ibele, P. J. Butler, and A. Sen, *J. Am. Chem. Soc.* **135**, 1406 (2013).
- [1.11] C. Riedel, R. Gabizon, C. A. M. Wilson, K. Hamadani, K. Tsekourasl, S. Marqusee, S. Presse, and C. Bustamante, *Nature (London)* **517**, 227 (2015).
- [1.12] P. Illien, X. Zhao, K. K. Dey, P. J. Butler, A. Sen, and R. Golestanian, *Nano Lett.* **17**, 4415 (2017).
- [1.13] R. Golestanian, *Phys. Rev. Lett.* **115**, 108102 (2015).

-
- [1.14] P. Illien, T. Adeleke-Larodo, and R. Golestanian, *EPL* **119**, 40002 (2017).
- [1.15] A.-Y. Jee, Y.-K. Cho, S. Granick, and T. Trusty, *Proc. Nat. Acad. Sci. U.S.A.* **115**, 14 (2018).
- [1.16] T. Ohmura, Y. Nishigamia, A. Taniguchi, S. Nonaka, J. Manabe, T. Ishikawa, and M. Ichikawa, *Proc. Nat. Acad. Sci. U.S.A.* **115**, 3231 (2018).
- [1.17] M. Ozaki and Y. Murayama, *Current Physical Chemistry* **5**, 64 (2015).
- [1.18] M. Doi, *Soft Matter Physics* (Oxford University, Oxford, 2013).
- [1.19] T. M. Squires and T. G. Mason, *Annu. Rev. Fluid Mech.* **42**, 413 (2010).
- [1.20] D. T. N. Chen, Q. Wen, P. A. Janmey, J. C. Crocker, and A. G. Yodh, *Annu. Rev. Condens. Matter Phys.* **1**, 301 (2010).
- [1.21] T. G. Mason and D. A. Weitz, *Phys. Rev. Lett.* **74**, 1250 (1995).
- [1.22] T. G. Mason, *Rheol. Acta* **39**, 371 (2000).
- [1.23] F. Gittes, B. Schnurr, P. D. Olmsted, F. C. MacKintosh, and C. F. Schmidt, *Phys. Rev. Lett.* **79**, 3286 (1997).
- [1.24] B. Schnurr, F. Gittes, F. C. MacKintosh, and C. F. Schmidt, *Macromolecules* **30**, 7781 (1997).
- [1.25] E. M. Purcell, *Am. J. Phys.* **45**, 3 (1977).
- [1.26] K. Ishimoto and M. Yamada, *SIAM J. Appl. Math.* **72**, 1686 (2012).
- [1.27] A. Shapere and F. Wilczek, *J. Fluid Mech.* **198**, 557-585 (1989).
- [1.28] E. Lauga and T. R. Powers, *Rep. Prog. Phys.* **72**, 096601 (2009).
- [1.29] H. C. Fu, V. B. Shenoy, and T. R. Powers, *EPL* **91**, 24002 (2010).
- [1.30] J. Teran, L. Fauci, and M. Shelley, *Phys. Rev. Lett.* **104**, 038101 (2010).

-
- [1.31] A. Najafi and R. Golestanian, *Phys. Rev. E* **69**, 062901 (2004).
- [1.32] R. Golestanian and A. Ajdari, *Phys. Rev. E* **77**, 036308 (2008).
- [1.33] G. Grosjean, M. Hubert, G. Lagubeau, and N. Vandewalle, *Phys. Rev. E* **94**, 021101(R) (2016).

Chapter 2

Three-Sphere Microswimmer in a Homogeneous Viscoelastic Fluid

I discuss the locomotion of a three-sphere microswimmer in a viscoelastic medium and propose a new type of active microrheology. I derive a relation that connects the average swimming velocity and the frequency-dependent viscosity of the surrounding medium. In this relation, the viscous contribution can exist only when the time-reversal symmetry is broken, whereas the elastic contribution is present only when the structural symmetry of the swimmer is broken. Purcell's scallop theorem should be generalized for a three-sphere swimmer in a viscoelastic medium.

2.1 Introduction

In this chapter, I propose a new type of active microrheology using a microswimmer. Microswimmers are tiny machines that swim in a fluid such as sperm cells or motile bacteria, and are expected to be applied to microfluidics and microsystems [2.1]. As one of the simplest microswimmers, I consider the Najafi–Golestanian three-sphere swimmer model [2.2, 2.3], where three in-line

spheres are linked by two arms of varying length [see Fig. 2.1]. Recently, such a swimmer has been experimentally realized [2.4]. I investigate its motion in a general viscoelastic medium, and obtain a relation that connects the average swimming velocity and the frequency-dependent complex shear viscosity of the surrounding viscoelastic medium. I show explicitly that the absence of the time-reversal symmetry of the swimmer motion leads to the real part of the viscosity, whereas the absence of the structural symmetry of the swimmer is reflected in the imaginary part of the viscosity. Hence, I shall call the proposed method the “swimmer-microrheology”. My result also indicates that Purcell’s scallop theorem [2.5, 2.6], which states that time-reversible body motion cannot be used for locomotion in a Newtonian fluid, should be generalized for a three-sphere swimmer in viscoelastic media if the structural symmetry is violated.

2.2 Model

The general equation that describes the hydrodynamics of a low-Reynolds-number flow in a viscoelastic medium is given by the following generalized Stokes equation [2.7]:

$$0 = \int_{-\infty}^t dt' \eta(t-t') \nabla^2 \mathbf{v}(\mathbf{r}, t') - \nabla p(\mathbf{r}, t). \quad (2.1)$$

Here $\eta(t)$ is the time-dependent shear viscosity, \mathbf{v} is the velocity field, p is the pressure field, and \mathbf{r} stands for a three-dimensional positional vector. The above equation is further subjected to the incompressibility condition, $\nabla \cdot \mathbf{v} = 0$. From these equations, one can obtain a linear relation between the time-dependent force $F(t)$ acting on a hard sphere of radius a and its time-dependent velocity $V(t)$. In the Fourier domain, this relation can be represented as

$$V(\omega) = \frac{1}{6\pi\eta[\omega]a} F(\omega), \quad (2.2)$$

where I use a bilateral Fourier transform for $V(\omega) = \int_{-\infty}^{\infty} dt V(t) e^{-i\omega t}$ and $F(\omega)$, while I employ a unilateral one for $\eta[\omega] = \int_0^{\infty} dt \eta(t) e^{-i\omega t}$. Equation (2.2) is the GSR, which has been successfully used in active microrheology experiments [2.8],

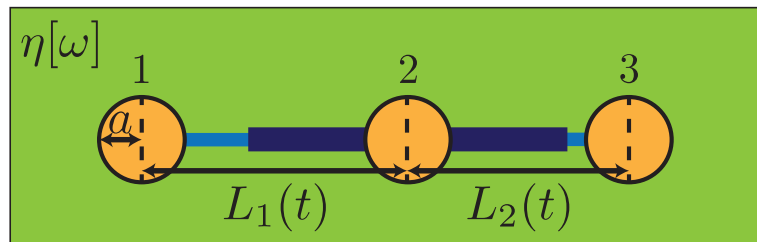


Figure 2.1: Najafi–Golestanian three-sphere swimmer model. Three identical spheres of radius a are connected by arms of lengths $L_1(t)$ and $L_2(t)$ and undergo time-dependent cyclic motion. The swimmer is embedded in a viscoelastic medium characterized by a frequency-dependent complex shear viscosity $\eta[\omega]$.

and its mathematical validity has also been discussed [2.9].

Next, I briefly explain the three-sphere model for a minimum swimmer introduced by Najafi and Golestanian [2.2, 2.3]. As schematically shown in Fig. 2.1, this model consists of three spheres of the same radius a that are connected by two arms of lengths $L_1(t)$ and $L_2(t)$, which undergo time-dependent motion. Their explicit time dependences will be given later. If we define the velocity of each sphere along the swimmer axis as $V_i(t)$ with $i = 1, 2, 3$, we have

$$\dot{L}_1(t) = V_2(t) - V_1(t), \quad (2.3)$$

$$\dot{L}_2(t) = V_3(t) - V_2(t), \quad (2.4)$$

where \dot{L}_1 and \dot{L}_2 indicate time derivatives.

Owing to the hydrodynamic effect, each sphere exerts a force F_i on the viscoelastic medium and experiences a force $-F_i$ from it. To relate the forces and the velocities in the frequency domain, we use the GSR in Eq. (2.2) and the Oseen tensor, in which the frequency-dependent viscosity $\eta[\omega]$ is used instead of a constant one [2.10, 2.11]. Assuming that $a \ll L_1, L_2$, we can write [2.2, 2.3]

$$V_1(\omega) = \frac{F_1(\omega)}{6\pi\eta[\omega]a} + \frac{1}{4\pi\eta[\omega]} \frac{F_2(\omega) * L_1^{-1}(\omega)}{2\pi} + \frac{1}{4\pi\eta[\omega]} \frac{F_3(\omega) * (L_1 + L_2)^{-1}(\omega)}{2\pi}, \quad (2.5)$$

$$V_2(\omega) = \frac{1}{4\pi\eta[\omega]} \frac{F_1(\omega) * L_1^{-1}(\omega)}{2\pi} + \frac{F_2(\omega)}{6\pi\eta[\omega]a} + \frac{1}{4\pi\eta[\omega]} \frac{F_3(\omega) * L_2^{-1}(\omega)}{2\pi}, \quad (2.6)$$

$$V_3(\omega) = \frac{1}{4\pi\eta[\omega]} \frac{F_1(\omega) * (L_1 + L_2)^{-1}(\omega)}{2\pi} + \frac{1}{4\pi\eta[\omega]} \frac{F_2(\omega) * L_2^{-1}(\omega)}{2\pi} + \frac{F_3(\omega)}{6\pi\eta[\omega]a}, \quad (2.7)$$

where we have used bilateral Fourier transforms such as

$$L_1^{-1}(\omega) = \int_{-\infty}^{\infty} dt \frac{e^{-i\omega t}}{L_1(t)}. \quad (2.8)$$

Furthermore, the convolution of two functions is generally defined by $g_1(\omega) * g_2(\omega) = \int_{-\infty}^{\infty} d\omega' g_1(\omega - \omega')g_2(\omega')$ in the above equations.

As in the original study, I am interested in the autonomous net locomotion of the swimmer, and there are no external forces acting on the spheres. If the inertia of the surrounding fluid can be neglected, we have the following force balance condition:

$$F_1(t) + F_2(t) + F_3(t) = 0. \quad (2.9)$$

Since Eqs. (2.5)–(2.7) involve convolutions in the frequency domain, we cannot solve these equations for arbitrary $L_1(t)$ and $L_2(t)$. Here I assume that the two arms undergo the following periodic motion:

$$L_1(t) = \ell + d_1 \cos(\Omega t), \quad (2.10)$$

$$L_2(t) = \ell + d_2 \cos(\Omega t - \phi). \quad (2.11)$$

In the above, ℓ is the constant length, d_1 and d_2 are the amplitudes of the oscillatory motion, Ω is the common arm frequency, and ϕ is the mismatch in the phases between the two arms. In the following analysis, we generally assume that $d_1, d_2 \ll \ell$. The *time-reversal symmetry* of the arm motion is present when $\phi = 0$ and π . Furthermore, I characterize the *structural symmetry* of the swimmer by d_1 and d_2 , i.e., the structure is symmetric when $d_1 = d_2$, while it is asymmetric when $d_1 \neq d_2$.

2.3 Results

Since the arm frequency is Ω , we assume that the velocities and the forces of the three spheres can generally be written as

$$V_i(\omega) = V_{i,0} \delta(\omega) + \sum_{n=1}^{\infty} [V_{i,n} \delta(\omega + n\Omega) + V_{i,-n} \delta(\omega - n\Omega)], \quad (2.12)$$

$$F_i(\omega) = F_{i,0} \delta(\omega) + \sum_{n=1}^{\infty} [F_{i,n} \delta(\omega + n\Omega) + F_{i,-n} \delta(\omega - n\Omega)], \quad (2.13)$$

where $i = 1, 2, 3$ for the three spheres. Substituting Eqs. (2.12) and (2.13) into the six coupled Eqs. (2.3)–(2.9), we obtain a matrix equation with infinite dimensions.

Under the conditions $d_1, d_2 \ll \ell$ and $a \ll \ell$, we are allowed to consider only $n = -1, 0, 1$ and we further use the approximation $F_{i,\pm 2} \approx 0$. Then we can solve for the six unknown functions $V_i(\omega)$ and $F_i(\omega)$, and also calculate the total swimming velocity $V = (V_1 + V_2 + V_3)/3$. Up to the lowest order terms in a , the average swimming velocity over one cycle of motion becomes [see also Appendix 2.A]

$$\bar{V} \approx \frac{7d_1 d_2 a \Omega}{24\ell^2} \frac{\eta'[\Omega]}{\eta_0} \sin \phi - \frac{5(d_1^2 - d_2^2) a \Omega}{48\ell^2} \frac{\eta''[\Omega]}{\eta_0}, \quad (2.14)$$

where $\eta'[\Omega]$ and $\eta''[\Omega]$ are the real and imaginary parts of the complex shear viscosity, respectively, and $\eta_0 = \eta[\Omega \rightarrow 0]$ is the constant zero-frequency viscosity.

The first term in Eq. (2.14) can be regarded as the viscous contribution and is present only if the time-reversal symmetry of the swimmer motion is broken, i.e., $\phi \neq 0, \pi$. The second term, on the other hand, corresponds to the elastic contribution, and exists only when the structural symmetry of the swimmer is broken, i.e., $d_1 \neq d_2$. If we are able to control d_1 , d_2 , and Ω of the swimmer, we can first obtain $\eta'[\Omega]$ by measuring \bar{V} as a function of Ω by setting $d_1 = d_2$. Then we make a difference between d_1 and d_2 to examine the change in \bar{V} , which then yields $\eta''[\Omega]$. The corresponding complex shear modulus is simply obtained by $G[\Omega] = i\Omega\eta[\Omega]$. This is a new type of active microrheology that I propose in this chapter.

Table 2.1: Locomotion of a three-sphere swimmer in a viscoelastic medium and the relevant rheological information.

medium	viscous				viscoelastic			
time-reversal symmetry	Y		N		Y		N	
structural symmetry	Y	N	Y	N	Y	N	Y	N
swimmer motion	N	N	Y	Y	N	Y	Y	Y
rheological information	–	–	N	N	–	η''	η'	η', η''

For a purely Newtonian fluid, namely, for a medium characterized by a constant viscosity, the second term in Eq. (2.14) vanishes, and the first term coincides with the expression obtained by Golestanian and Ajdari [2.3]. It should be noted here, however, that the velocity \bar{V} in this case no longer depends on the constant viscosity (because $\eta'[\Omega]/\eta_0 = 1$) and we cannot measure it from \bar{V} . Equation (2.14) also implies that the swimmer cannot move in a purely elastic medium, for which we have $\eta_0 \rightarrow \infty$. Importantly, owing to the presence of the second term, Purcell's scallop theorem should be generalized for a swimmer in a viscoelastic medium. Namely, even if the time-reversal symmetry of the swimmer motion is not broken, i.e., $\phi = 0, \pi$, the present swimmer can still move in a viscoelastic medium due to the second term as long as its structural symmetry is broken, i.e., $d_1 \neq d_2$. This behavior cannot be described by the original scallop theorem. On the basis of Eq. (2.14), I have summarized in Table I the motion of a three-sphere swimmer in a viscoelastic medium and the relevant rheological information.

To further illustrate my result, I first assume that the surrounding viscoelastic medium is described by a simple Maxwell model. In this case, the frequency-dependent viscosity can be written as

$$\eta[\omega] = \eta_0 \frac{1 - i\omega\tau_M}{1 + \omega^2\tau_M^2}, \quad (2.15)$$

where τ_M is the characteristic time scale. Within this model, the medium behaves as a viscous fluid for $\omega\tau_M \ll 1$, while it becomes elastic for $\omega\tau_M \gg 1$. Using

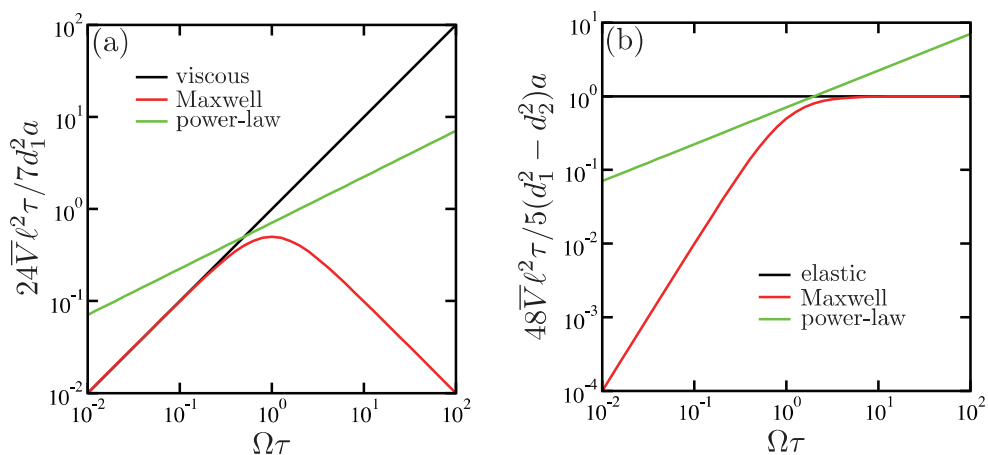


Figure 2.2: Average swimming velocity \bar{V} as a function of $\Omega\tau$, where Ω is the arm frequency and τ represents either τ_M for a Maxwell fluid (red lines) or τ_p for a power-law fluid (green lines). In the power-law model, we choose $\alpha = 1/2$. (a) Viscous contribution by setting $\phi = \pi/2$ and $d_1 = d_2$. Here \bar{V} is scaled by $7d_1^2a/(24\ell^2\tau)$. The case for a viscous fluid is plotted by the black line. (b) Elastic contribution by setting $\phi = 0$ and $d_1 \neq d_2$. Here \bar{V} is scaled by $5(d_1^2 - d_2^2)a/(48\ell^2\tau)$. The case for an elastic medium is plotted by the black line.

Eq. (2.15), we can easily obtain the average swimming velocity in Eq. (2.14) as

$$\bar{V} = \frac{7d_1d_2a\Omega}{24\ell^2} \frac{1}{1 + \Omega^2\tau_M^2} \sin\phi + \frac{5(d_1^2 - d_2^2)a\Omega}{48\ell^2} \frac{\Omega\tau_M}{1 + \Omega^2\tau_M^2}. \quad (2.16)$$

The first viscous term increases as $\bar{V} \sim \Omega$ for $\Omega\tau_M \ll 1$, while it decreases as $\bar{V} \sim \Omega^{-1}$ for $\Omega\tau_M \gg 1$. This is a unique feature of the viscoelasticity [2.1, 2.12, 2.13], but such a reduction occurs simply because the medium responds elastically in the high-frequency regime. On the other hand, the second elastic term increases as $\bar{V} \sim \Omega^2$ for $\Omega\tau_M \ll 1$, and it approaches a constant for $\Omega\tau_M \gg 1$. In Fig. 2.2(a), we plot the average swimming velocity \bar{V} as a function of the dimensionless arm frequency $\Omega\tau_M$ when $\phi = \pi/2$ and $d_1 = d_2$. This plot corresponds to the first term in Eq. (2.16). As a reference, the behavior of $\bar{V} \sim \Omega$ for a purely viscous fluid is also plotted. Figure 2.2(b) is a similar plot when $\phi = 0$ and $d_1 \neq d_2$, and corresponds to the second term in Eq. (2.16).

As a different example, I next consider the case in which the viscoelastic

medium is described by a power-law model such that [2.7, 2.14, 2.15]

$$\eta[\omega] = G_0(i\omega)^{\alpha-1}, \quad (2.17)$$

where the exponent can take values of $0 \leq \alpha \leq 1$. With this expression, the complex shear modulus also exhibits a power-law behavior, $G[\omega] = G_0(i\omega)^\alpha$. The limits of $\alpha = 0$ and 1 correspond to the purely elastic and the purely viscous cases, respectively. In the case of a power-law fluid, the average swimming velocity can be obtained from Eqs. (2.14) and (2.17) as

$$\bar{V} = \frac{7d_1d_2a}{24\ell^2\tau_p}(\Omega\tau_p)^\alpha \sin(\pi\alpha/2) \sin\phi + \frac{5(d_1^2 - d_2^2)a}{48\ell^2\tau_p}(\Omega\tau_p)^\alpha \cos(\pi\alpha/2), \quad (2.18)$$

where $\tau_p = (\eta_0/G_0)^{1/(1-\alpha)}$. Here we have assumed that the medium behaves as a purely viscous fluid in the low-frequency limit characterized by a finite viscosity η_0 . According to the above expression, the swimming velocity scales as $\bar{V} \sim \Omega^\alpha$ in both the first and second terms. For the purely viscous case of $\alpha = 1$, the first term reduces to the result by Golestanian and Ajdari [2.3], while the second term vanishes. For the purely elastic case of $\alpha = 0$, on the other hand, the first term vanishes and the second term remains, although the latter no longer depends on the arm frequency Ω . In Figs. 2.2(a) and 2.2(b), we have also plotted the average velocity \bar{V} as a function of $\Omega\tau_p$ when $\alpha = 1/2$. In both of these plots, the scaling behavior $\bar{V} \sim \Omega^{1/2}$ is seen.

2.4 Summary and discussion

Lauga considered the axisymmetric squirming motion of a sphere (squirmer) embedded in an Oldroyd-B fluid, which represents a typical polymeric fluid [2.16]. He reported that the scallop theorem in a viscoelastic fluid breaks down if the squirmer has fore-aft asymmetry in its surface velocity distribution. For a time-reversal deformation given by a simple sinusoidal gait, he showed that the average swimming velocity is given by $\bar{V} \sim \Omega\text{De}/(1 + \text{De}^2)$, where the Deborah number is given by $\text{De} = \Omega\tau_0$ with a characteristic relaxation time τ_0 in the Oldroyd-B model. Such a frequency dependence of the swimming velocity is

identical to the second term of Eq. (2.16) obtained for a Maxwell fluid, although Eq. (2.14) is more general. On the other hand, my result is different from that by Curtis and Gaffney [2.17], because they showed that the swimming velocity in a viscoelastic medium is the same as that in a Newtonian fluid.

To summarize, I have proposed a new active microrheology using the Najafi–Golestanian three-sphere swimmer. The frequency dependence of the average swimming speed provides us with the complex shear viscosity of the surrounding viscoelastic medium. Here the viscous contribution can exist only when the time-reversal symmetry of the swimmer is broken, whereas the elastic contribution is present only if its structural symmetry is broken.

Even though the argument in this chapter is restricted to the artificial three-sphere swimmer, I expect that my basic concept can still be applied to more complex biological processes such as the motion of bacteria, flagellated cellular swimming, and the beating of cilia. Since most of these phenomena take place in a viscoelastic environment, I hope that the concept of my new active microrheology will be used in the future to reveal their mechanical and dynamical properties.

2.A Derivation of Eq. (2.14)

In this appendix, I show the detailed derivation of Eq. (2.14). Substituting Eqs. (2.10) and (2.12) into Eq. (2.3), we obtain

$$V_{2,0} - V_{1,0} = 0, \quad (2.19)$$

$$V_{2,1} - V_{1,1} = -i\pi d_1 \Omega, \quad (2.20)$$

$$V_{2,-1} - V_{1,-1} = i\pi d_1 \Omega, \quad (2.21)$$

$$V_{2,n} - V_{1,n} = 0 \quad \text{for } |n| \geq 2. \quad (2.22)$$

Similarly, substituting Eqs. (2.11) and (2.12) into Eq. (2.4), we obtain

$$V_{3,0} - V_{2,0} = 0, \quad (2.23)$$

$$V_{3,1} - V_{2,1} = \pi d_2 \Phi_2 \Omega, \quad (2.24)$$

$$V_{3,-1} - V_{2,-1} = \pi d_2 \Phi_1 \Omega, \quad (2.25)$$

$$V_{3,n} - V_{2,n} = 0 \quad \text{for } |n| \geq 2, \quad (2.26)$$

where we have used the following notations

$$\Phi_1 = i \cos \phi + \sin \phi, \quad (2.27)$$

$$\Phi_2 = -i \cos \phi + \sin \phi. \quad (2.28)$$

Next we expand Eqs. (2.5), (2.6) and (2.7) in terms of the small quantities d_1/ℓ and d_2/ℓ while keeping only the lowest order terms. Substituting Eqs. (2.12) and (2.13) into these three equations, we obtain

$$\begin{aligned} V_{1,n} \approx & \frac{F_{1,n}}{6\pi\eta[-n\Omega]a} + \frac{1}{4\pi\eta[-n\Omega]\ell} \left(F_{2,n} - \frac{d_1 F_{2,n+1}}{2\ell} - \frac{d_1 F_{2,n-1}}{2\ell} \right) \\ & + \frac{1}{4\pi\eta[-n\Omega]\ell} \left(\frac{F_{3,n}}{2} - \frac{d_1 F_{3,n+1}}{8\ell} - \frac{d_1 F_{3,n-1}}{8\ell} \right. \\ & \left. + \frac{id_2 \Phi_1 F_{3,n+1}}{8\ell} - \frac{id_2 \Phi_2 F_{3,n-1}}{8\ell} \right), \end{aligned} \quad (2.29)$$

$$\begin{aligned} V_{2,n} \approx & \frac{1}{4\pi\eta[-n\Omega]\ell} \left(F_{1,n} - \frac{d_1 F_{1,n+1}}{2\ell} - \frac{d_1 F_{1,n-1}}{2\ell} \right) + \frac{F_{2,n}}{6\pi\eta[-n\Omega]a} \\ & + \frac{1}{4\pi\eta[-n\Omega]\ell} \left(F_{3,n} + \frac{id_2 \Phi_1 F_{3,n+1}}{2\ell} - \frac{id_2 \Phi_2 F_{3,n-1}}{2\ell} \right), \end{aligned} \quad (2.30)$$

$$\begin{aligned} V_{3,n} \approx & \frac{1}{4\pi\eta[-n\Omega]\ell} \left(\frac{F_{1,n}}{2} - \frac{d_1 F_{1,n+1}}{8\ell} - \frac{d_1 F_{1,n-1}}{8\ell} \right. \\ & \left. + \frac{id_2 \Phi_1 F_{1,n+1}}{8\ell} - \frac{id_2 \Phi_2 F_{1,n-1}}{8\ell} \right) \\ & + \frac{1}{4\pi\eta[-n\Omega]\ell} \left(F_{2,n} + \frac{id_2 \Phi_1 F_{2,n+1}}{2\ell} - \frac{id_2 \Phi_2 F_{2,n-1}}{2\ell} \right) + \frac{F_{3,n}}{6\pi\eta[-n\Omega]a}. \end{aligned} \quad (2.31)$$

Note that the couplings between different n -modes are involved in these equations. Finally, substituting Eq. (2.13) into Eq. (2.9), we obtain

$$F_{1,n} + F_{2,n} + F_{3,n} = 0. \quad (2.32)$$

The above set of equations constitute a matrix equation with infinite dimensions and cannot be solved in general. Under the assumption of $a \ll \ell$, however, we are allowed to consider only $n = -1, 0, 1$ and further approximate as $F_{i,\pm 2} \approx 0$. The justification of the latter approximation is also seen by solving

Eqs. (2.22), (2.26), (2.29), (2.30), (2.31) and (2.32) for $n = \pm 2$ and taking the limit of $a \ll \ell$. Hence the above set of equations can be solved for 18 unknowns, i.e., $V_{i,n}$ and $F_{i,n}$ for $i = 1, 2, 3$ and $n = -1, 0, 1$.

The velocity of each sphere is simply obtained by the inverse Fourier transform, $V_i(t) = (2\pi)^{-1} \int_{-\infty}^{\infty} d\omega V_i(\omega) e^{i\omega t}$. The average swimming velocity over one cycle of motion is then calculated by

$$\bar{V} = \frac{\Omega}{2\pi} \int_0^{2\pi/\Omega} dt [V_1(t) + V_2(t) + V_3(t)]/3. \quad (2.33)$$

Up to the lowest order terms in a , we finally obtain Eq. (2.14). In order to obtain more accurate higher order terms in a , one needs to take into account the higher order n -modes ($|n| \geq 2$).

References

- [2.1] E. Lauga and T. R. Powers, Rep. Prog. Phys. **72** 096601 (2009).
- [2.2] A. Najafi and R. Golestanian, Phys. Rev. E **69**, 062901 (2004).
- [2.3] R. Golestanian and A. Ajdari, Phys. Rev. E **77**, 036308 (2008).
- [2.4] G. Grosjean, M. Hubert, G. Lagubeau, and N. Vandewalle, Phys. Rev. E **94**, 021101(R) (2016).
- [2.5] E. M. Purcell, Am. J. Phys. **45**, 3 (1977).
- [2.6] E. Lauga, Soft Matter **7**, 3060 (2011).
- [2.7] R. Granek, Soft Matter **7**, 5281 (2011).
- [2.8] F. Gittes, B. Schnurr, P. D. Olmsted, F. C. MacKintosh, and C. F. Schmidt, Phys. Rev. Lett. **79**, 3286 (1997).
- [2.9] B. Schnurr, F. Gittes, F. C. MacKintosh, and C. F. Schmidt, Macromolecules **30**, 7781 (1997).
- [2.10] T. G. Mason and D. A. Weitz, Phys. Rev. Lett. **74**, 1250 (1995).

- [2.11] T. G. Mason, *Rheol. Acta* **39**, 371 (2000).
- [2.12] H. C. Fu, T. R. Powers, and C. W. Wolgemuth, *Phys. Rev. Lett.* **99**, 258101 (2007).
- [2.13] H. C. Fu, C. W. Wolgemuth, and T. R. Powers, *Phys. Fluids* **21**, 033102 (2009).
- [2.14] S. Komura, S. Ramachandran, and K. Seki, *EPL* **97**, 68007 (2012).
- [2.15] S. Komura, K. Yasuda, and R. Okamoto, *J. Phys.: Condens. Matter* **27**, 432001 (2015).
- [2.16] E. Lauga, *EPL* **86**, 64001 (2009).
- [2.17] M. P. Curtis and E. A. Gaffney, *Phys. Rev. E* **87**, 043006 (2013).

Chapter 3

Three-Disk Microswimmer in a Two-Dimensional Fluid

A model of three-disk micromachine swimming in a quasi two-dimensional supported membrane is proposed. I calculate the average swimming velocity as a function of the disk size and the arm length. Due to the presence of the hydrodynamic screening length in the quasi two-dimensional fluid, the geometric factor appearing in the average velocity exhibits three different asymptotic behaviors depending on the microswimmer size and the hydrodynamic screening length. This is in sharp contrast with a microswimmer in a three-dimensional bulk fluid that shows only a single scaling behavior. I also find that the maximum velocity is obtained when the disks are equal-sized, whereas it is minimized when the average arm lengths are identical. The intrinsic drag of the disks on the substrate does not alter the scaling behaviors of the geometric factor.

3.1 Introduction

Biological membranes are composed of lipid molecules and various types of proteins which can move laterally due to the membrane fluidity [3.1]. Hence biomembranes play important roles in various life processes, such as the transportation of materials or the reaction between chemical species [3.2]. While some

proteins are subjected to thermal agitations of lipid molecules and undergo passive Brownian motions [3.3, 3.4], there is also a large number of active proteins which cyclically change their conformations [3.5]. For instance, with a supply of adenosine triphosphate (ATP), some proteins act as ion pumps by changing their structural conformations in order to allow materials to pass through the membranes [3.6–3.8]. In general, such cyclic motions of proteins can lead to their active locomotion under certain conditions rather than just a passive motion.

By converting chemical energy into mechanical work, microswimmers change their shape and move in viscous environments [3.9]. Over the length scale of microswimmers, the fluid forces acting on them are governed by the effect of viscous dissipation. According to Purcell’s scallop theorem [3.10], time-reversal body motion cannot be used for locomotion in a Newtonian fluid [3.11]. As one of the simplest models exhibiting broken time-reversal symmetry in a three-dimensional (3D) fluid, Najafi and Golestanian proposed a three-sphere swimmer [3.12, 3.13], in which three in-line spheres are linked by two arms of varying length. This model is suitable for analytical treatment because it is sufficient to consider only the translational motion, and the tensorial structure of the fluid motion can be neglected. Recently, such a three-sphere swimmer has been experimentally realized [3.14, 3.15]. Moreover, some authors proposed a generalized three-sphere microswimmer in which the spheres are connected by two elastic springs with varying natural lengths [3.16, 3.17].

Compared to microswimmers in 3D bulk fluids, those in two-dimensional (2D) or quasi-2D fluids such as biomembranes have been less investigated in spite of their importances. Huang *et al.* considered a model of an active inclusion in a membrane with three particles (domains) connected by variable elastic springs [3.18]. In their model, the natural lengths of the springs depend on the discrete states that are cyclically switched. They also performed a microscopic dynamical simulation, where the lipid bilayer structure of the membrane is resolved and the solvent effects are included by multiparticle collision dynamics.

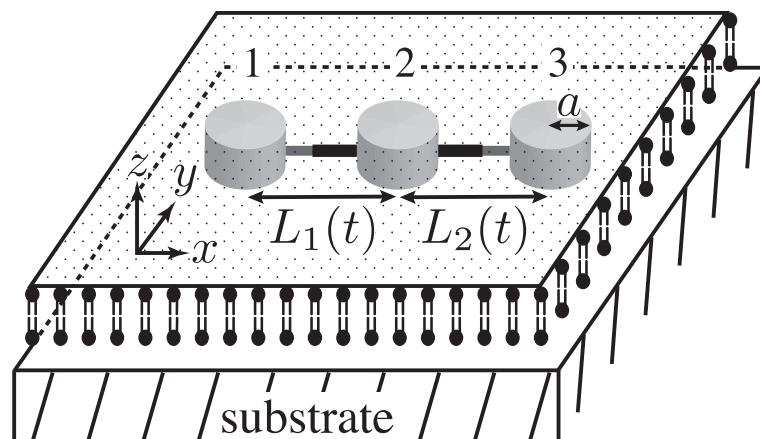


Figure 3.1: A 2D three-disk micromachine swimming in a fluid membrane supported by a solid substrate. The flat fluid membrane located at $z = 0$ is infinitely large and its 2D viscosity is η . The 2D momentum within the membrane can leak away due to the friction between the membrane and the substrate [see Eq. (3.1)], and hence the membrane corresponds to a quasi-2D fluid. The 2D microswimmer consists of three rigid disks of radii a_i ($i = 1, 2, 3$) that are connected by two arms of variable lengths L_j ($j = 1, 2$). Without loss of generality, the microswimmer is assumed to move along the x -axis. In the present model, the two arms can open and close in a prescribed form.

For quasi-2D fluids, there exists a hydrodynamic screening length which distinguishes 2D and 3D hydrodynamic interactions [3.19, 3.20]. In the model by Huang *et al.*, the longitudinal coupling mobility has a logarithmic dependence on the distance between two particles, which is valid only when the distance is much smaller than the hydrodynamic screening length. As for the mobility of a particle, they employed the 3D Stokes law even in a 2D fluid membrane, which is justified only when the particle size is much larger than the hydrodynamic screening length.

In this chapter, I present a systematic and also analytical investigation on the locomotion of a 2D microswimmer immersed in a supported fluid membrane, i.e., a lipid bilayer membrane located on a solid substrate [3.21, 3.22]. For supported membranes, the membrane-substrate distance is usually not large, and such a direct contact leads to a frictional coupling between the membrane and the solid support. My swimmer consists of three thin rigid disks (rather than spheres)

connected by two arms or springs which can undergo prescribed cyclic motions. I employ the 2D mobility and the coupling mobility that take into account the hydrodynamic interactions mediated by the quasi-2D fluid in the presence of the substrate [3.19]. I analytically obtain the average velocity of such a three-disk micromachine as a function of the disk and arm sizes. Due to the presence of the hydrodynamic screening length associated with the quasi-2D fluid model, the geometric factor in the average velocity exhibits various asymptotic size dependencies, which is in sharp contrast to a microswimmer in a 3D bulk fluid because they do not have any characteristic length scale.

In the next section, I briefly review the mobilities in a quasi-2D fluid describing a supported membrane. In Sec. 3.3, I discuss the motion of a 2D three-disk microswimmer in a supported membrane. In Sec. 3.4, I argue various asymptotic behaviors of the geometric factor appearing in the average velocity. I also examine the effects of structural asymmetry of 2D and 3D microswimmers in Sec. 3.5. Finally, the summary of my work and some discussions are given in Sec. 3.6.

3.2 Mobilities in a two-dimensional fluid

I first describe the quasi-2D hydrodynamic model for a supported fluid membrane as shown in Fig. 3.1. Although a lipid bilayer membrane itself can be treated as a 2D fluid, it is not an isolated system because the membrane is supported by the outer solid substrate (hence a quasi-2D fluid). Due to the friction between the 2D membrane and the substrate, the momentum within the membrane can leak away from the membrane. Such an effect can be taken into account through a momentum decay term in the hydrodynamic equation. Within the Stokes approximation and by assuming the steady state, I consider the following 2D equation for a supported membrane [3.23–3.25]:

$$\eta \nabla^2 \mathbf{v} - \nabla p - \lambda \mathbf{v} = 0. \quad (3.1)$$

In the above, $\nabla = (\partial_x, \partial_y)$ is a 2D differential operator, \mathbf{v} (m/s) and p (N/m) are the 2D velocity and pressure, respectively, η (N·s/m) is the membrane 2D viscosity, and λ (N·s/m³) is the momentum decay parameter (or the friction coefficient). In addition, I employ the 2D incompressibility condition as expressed by

$$\nabla \cdot \mathbf{v} = 0. \quad (3.2)$$

It is worthwhile to briefly mention here the physical meaning of the friction parameter λ . For a supported membrane, a thin lubricating layer of bulk solvent [thickness h and 3D viscosity η_s (N·s/m²)] exists between the membrane and the substrate [3.23]. In such a situation, the friction parameter in Eq. (3.1) can be identified as $\lambda = \eta_s/h$, provided that h is small enough [3.25].

Solving the above quasi-2D hydrodynamic equations, one can obtain the translational mobility coefficient μ of a rigid disk that is defined by $V = \mu F$, where V is the disk velocity and F is a driving force. By using the no-slip boundary condition, the resulting expression becomes [3.23–3.25]

$$\mu(a) = \frac{1}{4\pi\eta} \left[\frac{(\kappa a)^2}{4} + \frac{\kappa a K_1(\kappa a)}{K_0(\kappa a)} \right]^{-1}, \quad (3.3)$$

where a is the disk radius, $\kappa = \sqrt{\lambda/\eta}$, and K_0 and K_1 are modified Bessel functions of the second kind, order zero and one, respectively. Physically, κ^{-1} represents the hydrodynamic screening length beyond which the 2D hydrodynamic interaction becomes irrelevant. Notice that κ^{-1} diverges as $\lambda \rightarrow 0$, which alludes the Stokes paradox in a pure 2D fluid [3.3, 3.4]. The effect of intrinsic drag of the disk on the substrate will be discussed later in the final section.

For $\kappa a \ll 1$, the above disk mobility asymptotically behaves as

$$\mu(a) \approx \frac{1}{4\pi\eta} \left[\ln \left(\frac{2}{\kappa a} \right) - \gamma \right], \quad (3.4)$$

where $\gamma = 0.5772 \dots$ is Euler's constant. Here the mobility is only weakly (logarithmically) dependent on the disk size a , which is characteristic for 2D

fluids. For $\kappa a \gg 1$, on the other hand, we have

$$\mu(a) \approx \frac{1}{\pi\eta(\kappa a)^2}, \quad (3.5)$$

which shows a stronger algebraic size dependence when compared with the Stokes law for 3D fluids. Such a size dependence can be understood in terms of mass conservation principle because 2D momentum is not conserved any more in the quasi-2D hydrodynamics [3.26].

Next I explain the hydrodynamic interaction between the two disks immersed in the membrane by using the velocity Green's function $G_{\alpha\beta}(\mathbf{r})$. This tensor gives the flow velocity $\mathbf{v}(\mathbf{r})$ of the membrane at \mathbf{r} due to a point force \mathbf{F} exerted on the membrane at the origin in the xy -plane, according to $v_\alpha(\mathbf{r}) = G_{\alpha\beta}(\mathbf{r})F_\beta$ with $\alpha, \beta = x, y$. The velocity Green's function can generally be expressed as $G_{\alpha\beta}(\mathbf{r}) = C_1(r)\delta_{\alpha\beta} + C_2(r)(r_\alpha r_\beta / r^2)$ where $\delta_{\alpha\beta}$ is the Kronecker delta and $r = |\mathbf{r}|$. The longitudinal coupling mobility between the two disks in the membrane can be obtained from $M(r) = C_1(r) + C_2(r)$, where r here denotes the distance between the two disks and should satisfy the condition $r \gg a$. Hence M does not depend on a up to the lowest order contribution.

Using the quasi-2D hydrodynamic equations, the longitudinal coupling mobility M is given by [3.27–3.31]

$$M(r) = \frac{1}{2\pi\eta} \left[\frac{1}{(\kappa r)^2} - \frac{K_1(\kappa r)}{\kappa r} \right]. \quad (3.6)$$

For $\kappa r \ll 1$, the above coupling mobility asymptotically behaves as

$$M(r) \approx \frac{1}{4\pi\eta} \left[\ln \left(\frac{2}{\kappa r} \right) - \gamma + \frac{1}{2} \right]. \quad (3.7)$$

For $\kappa r \gg 1$, on the other hand, we have

$$M(r) \approx \frac{1}{2\pi\eta(\kappa r)^2}. \quad (3.8)$$

Equations (3.7) and (3.8) are analogous to Eqs. (3.4) and (3.5), respectively, and the physical origins are exactly the same as those for the disk mobility μ .

3.3 Three-disk microswimmer

Having explained the quasi-2D hydrodynamic model for a supported membrane and the resulting mobilities for inclusions, I now investigate the locomotion of a microswimmer in a membrane. To calculate the swimming velocity, I follow the procedure in Ref. [3.13] for a three-sphere swimmer in a 3D bulk fluid. As shown in Fig. 3.1, I consider a 2D micromachine consisting of three rigid disks of radii a_i ($i = 1, 2, 3$) that are connected by two arms of variable lengths L_j ($j = 1, 2$). Such a three-disk microswimmer is immersed in an infinitely large and flat supported membrane having 2D viscosity η and the friction coefficient λ , as described before. Each disk exerts a force F_i on the quasi-2D fluid that we assume to be along the swimmer axis. Without loss of generality, the microswimmer is assumed to move along the x -axis. In the limit $a_i/L_j \ll 1$, we can use Eqs. (3.3) and (3.6) to relate the forces F_i and the velocities V_i as

$$V_1 = \mu(a_1)F_1 + M(L_1)F_2 + M(L_1 + L_2)F_3, \quad (3.9)$$

$$V_2 = M(L_1)F_1 + \mu(a_2)F_2 + M(L_2)F_3, \quad (3.10)$$

$$V_3 = M(L_1 + L_2)F_1 + M(L_2)F_2 + \mu(a_3)F_3. \quad (3.11)$$

The swimming velocity of the whole object is obtained by averaging the velocities of the three disks, i.e., $V = (V_1 + V_2 + V_3)/3$. Since we are interested in the autonomous net locomotion of the swimmer, there are no external forces acting on the disks. This leads to the following force-free condition:

$$F_1 + F_2 + F_3 = 0. \quad (3.12)$$

As assumed in Ref. [3.13], the motion of the arms connecting the three disks is prescribed by the two given functions $L_j(t)$. In this situation, the arm motions are related to the velocities as

$$\dot{L}_1 = V_2 - V_1, \quad \dot{L}_2 = V_3 - V_2, \quad (3.13)$$

where the dot indicates the time derivative. The set of six equations in Eqs. (3.9), (3.10), (3.11), (3.12), and (3.13) is sufficient to solve for the six unknown quan-

tities V_i and F_i ($i = 1, 2, 3$).

We further assume that arm deformations are relatively small as given by

$$L_1(t) = \ell_1 + u_1(t), \quad L_2(t) = \ell_2 + u_2(t), \quad (3.14)$$

where ℓ_j are constants and $u_j/\ell_j \ll 1$. With these prescribed arm motions, we perform an expansion of the swimming velocity to the leading order in both a_i/ℓ_j and u_j/ℓ_j . After some calculations, we finally obtain the average swimming velocity as [3.13]

$$\bar{V} = \frac{G}{2} \langle u_1 \dot{u}_2 - \dot{u}_1 u_2 \rangle, \quad (3.15)$$

where G is the geometric factor to be presented later in Eq. (3.18), and the averaging $\langle \dots \rangle$ should be performed by time integration in a full cycle. In the above calculation, the terms proportional to $u_1 \dot{u}_1$, $u_2 \dot{u}_2$, and $u_1 \dot{u}_2 + \dot{u}_1 u_2$ are omitted because they average out to zero in a cycle.

As studied for a three-sphere swimmer [3.13], one can assume, for example, that the two arms undergo the following periodic motions:

$$u_1(t) = d_1 \cos(\Omega t), \quad u_2(t) = d_2 \cos(\Omega t - \phi). \quad (3.16)$$

Here, d_1 and d_2 are the amplitudes of the oscillatory motions, Ω is a common arm frequency, and ϕ is a mismatch in phases between the two arms. Then the average swimming velocity in Eq. (3.15) further reads

$$\bar{V} = \frac{G}{2} d_1 d_2 \Omega \sin \phi, \quad (3.17)$$

which is maximized when $\phi = \pi/2$. When the disks are connected by elastic springs with time-dependent natural lengths, a more general expression for \bar{V} can be obtained [3.17].

3.4 Geometric factor

The geometric factor G (having the dimension of inverse length) in Eq. (3.15) or Eq. (3.17) for a three-disk swimmer in a quasi-2D fluid turns out to be

$$\frac{G(\epsilon_i, \delta_j)}{\kappa}$$

$$= \frac{Y}{Z^2} \left[2 \left(\frac{1}{\delta_1^3} + \frac{1}{\delta_2^3} - \frac{1}{(\delta_1 + \delta_2)^3} \right) - \left(\frac{K_2(\delta_1)}{\delta_1} + \frac{K_2(\delta_2)}{\delta_2} - \frac{K_2(\delta_1 + \delta_2)}{\delta_1 + \delta_2} \right) \right], \quad (3.18)$$

where

$$\begin{aligned} Y &= \epsilon_1 \epsilon_2 \epsilon_3 K_0(\epsilon_1) K_0(\epsilon_2) K_0(\epsilon_3) [\epsilon_1 K_0(\epsilon_1) + 4K_1(\epsilon_1)] \\ &\quad \times [\epsilon_2 K_0(\epsilon_2) + 4K_1(\epsilon_2)] [\epsilon_3 K_0(\epsilon_3) + 4K_1(\epsilon_3)], \\ Z &= 4\epsilon_1 K_1(\epsilon_1) K_0(\epsilon_2) K_0(\epsilon_3) + 4\epsilon_2 K_0(\epsilon_1) K_1(\epsilon_2) K_0(\epsilon_3) \\ &\quad + 4\epsilon_3 K_0(\epsilon_1) K_0(\epsilon_2) K_1(\epsilon_3) + (\epsilon_1^2 + \epsilon_2^2 + \epsilon_3^2) K_0(\epsilon_1) K_0(\epsilon_2) K_0(\epsilon_3). \end{aligned}$$

Here, $\epsilon_i = \kappa a_i$ and $\delta_j = \kappa l_j$, and K_2 is modified Bessel function of the second kind, order two. I note that Eq. (3.18) is invariant under the exchange of not only the three disks a_i , but also under the exchange of the two arms l_j .

For the fully symmetric case with $a_1 = a_2 = a_3 = a$ and $l_1 = l_2 = l$, the geometric factor in Eq. (3.18) reduces to

$$\frac{G(\epsilon, \delta)}{\kappa} = \frac{1}{36} \left[\epsilon^2 + \frac{4\epsilon K_1(\epsilon)}{K_0(\epsilon)} \right] \left[\frac{15}{\delta^3} - \frac{8K_2(\delta)}{\delta} + \frac{2K_2(2\delta)}{\delta} \right], \quad (3.19)$$

where $\epsilon = \kappa a$ and $\delta = \kappa l$. Equations (3.18) and (3.19) are the main results of this chapter. In Fig. 3.2, I plot G/κ in Eq. (3.19) as a function of δ while keeping the ratio to $a/l = 10^{-2}$. In fact, Eq. (3.19) has three asymptotic expressions

$$\frac{G(\epsilon, \delta)}{\kappa} \approx \frac{1}{3\delta[\ln(2/\epsilon) - \gamma]} \quad (3.20)$$

for $\epsilon \ll 1$ and $\delta \ll 1$,

$$\frac{G(\epsilon, \delta)}{\kappa} \approx \frac{5}{3\delta^3[\ln(2/\epsilon) - \gamma]} \quad (3.21)$$

for $\epsilon \ll 1$ and $\delta \gg 1$, and

$$\frac{G(\epsilon, \delta)}{\kappa} \approx \frac{5\epsilon^2}{12\delta^3} \quad (3.22)$$

for $\epsilon \gg 1$ and $\delta \gg 1$.

I note here that Eq. (3.20) decays as δ^{-1} , whereas Eqs. (3.21) and (3.22) decay as δ^{-3} . The dependence on the disk size ϵ is only logarithmic in Eqs. (3.20) and (3.21), while it is proportional to ϵ^2 in Eq. (3.22). In Fig. 3.2, I also plot

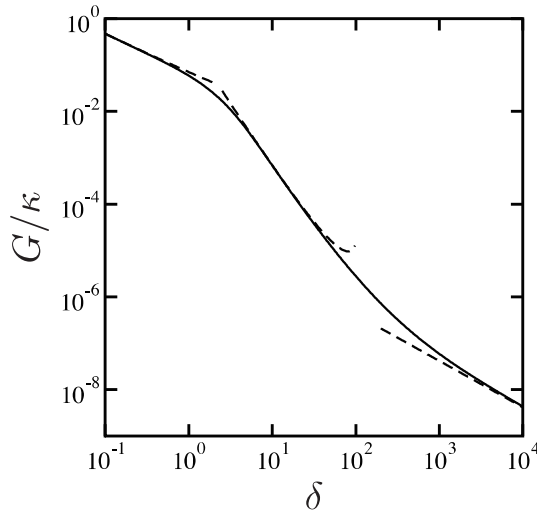


Figure 3.2: Plot of the scaled geometric factor G/κ [see Eq. (3.19)] for a fully symmetric 2D microswimmer as a function of the scaled arm length $\delta = \kappa\ell$ when the disk-to-arm ratio is $a/\ell = 10^{-2}$. The three asymptotic expressions in Eqs. (3.20), (3.21), and (3.22) are plotted by the dashed lines.

the above three asymptotic expressions by the dashed lines when $a/\ell = 10^{-2}$. They are all in good agreement with the solid line that corresponds to the full expression of Eq. (3.19). Notice that the apparent behavior of Eq. (3.22) is δ^{-1} because I have fixed the ratio to $a/\ell = 10^{-2}$ in this plot.

It is important to mention the physical meaning of the geometric factor G in the average velocity. Within the scaling argument, the geometric factor is generally related to the mobility coefficient μ and the longitudinal coupling mobility M by

$$G(a, \ell) \sim \frac{M(\ell)}{\mu(a)\ell}. \quad (3.23)$$

This relation holds irrespective of the dimensionality of the micromachine and the surrounding fluid [3.32]. Due to the presence of the hydrodynamic screening length κ^{-1} in a supported membrane, both μ and M exhibit different asymptotic behaviors as shown in Eqs. (3.4), (3.5) and Eqs. (3.7), (3.8), respectively. Various limiting expressions of G in Eqs. (3.20)-(3.22) can be understood as different combinations of the asymptotic forms of μ and M . For example, Eq. (3.22) showing the scaling $G \sim (a^2/\ell^2)/\ell$ is a direct consequence of Eqs. (3.5) and

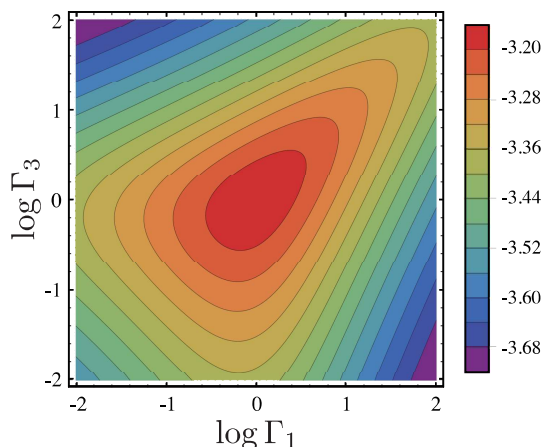


Figure 3.3: Color plot of the scaled geometric factor $\log(G/\kappa)$ [see Eq. (3.18)] of a 2D microswimmer as a function of the asymmetry parameters $\Gamma_1 = a_1/a_2$ and $\Gamma_3 = a_3/a_2$ [see Eq. (3.26)] when $\kappa a = 0.1$ and $\kappa \ell = 10$. Notice that $a = (a_1 + a_2 + a_3)/3$ and $\ell = \ell_1 = \ell_2$. All the quantities including the color scale are plotted in the logarithmic scale. The maximum of G occurs at $\Gamma_1 = \Gamma_3 = 1$.

(3.8). I also note that, because of the explicit $1/\ell$ -dependence in Eq. (3.23), the logarithmic dependence of $M(\ell)$ on ℓ , as in Eq. (3.7), does not show up in Eq. (3.20) within the lowest order expansion.

In order to compare my result with that of a three-sphere swimmer in a 3D fluid, I show here its corresponding geometric factor as obtained in Ref. [3.13]:

$$G_{3D} = \frac{3a_1a_2a_3}{(a_1 + a_2 + a_3)^2} \left[\frac{1}{\ell_1^2} + \frac{1}{\ell_2^2} - \frac{1}{(\ell_1 + \ell_2)^2} \right], \quad (3.24)$$

where a_i here denote the radii of the three spheres (rather than disks). For the symmetric case with $a_1 = a_2 = a_3 = a$ and $\ell_1 = \ell_2 = \ell$, the above expression reduces to

$$G_{3D} = \frac{7a}{12\ell^2}. \quad (3.25)$$

First, I note that Eq. (3.24) or Eq. (3.25) does not depend on the 3D fluid viscosity, while Eq. (3.18) or Eq. (3.19) is dependent on the membrane viscosity η through the inverse screening length κ . Second, the essential size dependence in Eq. (3.25) is $G_{3D} \sim (a/\ell)/\ell$ which does not appear in the previous quasi-2D case. On the other hand, such a dependence is in accordance with the scaling relation Eq. (3.23) and the Stokes law in a 3D fluid without any characteristic

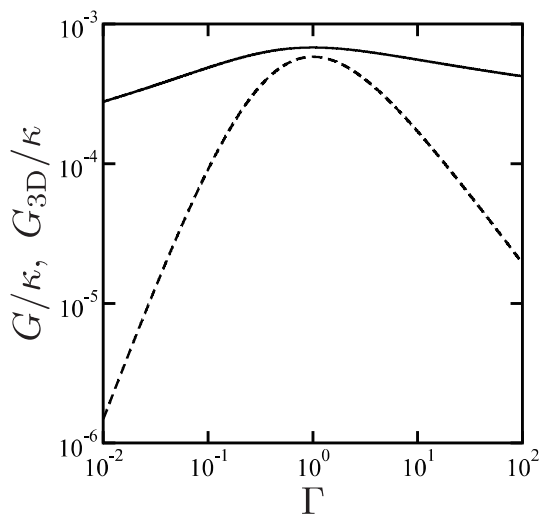


Figure 3.4: Plot of the scaled geometric factor G/κ (solid line) [see Eq. (3.18)] and G_{3D}/κ (dashed line) [see Eq. (3.24)] as a function of the asymmetry parameter $\Gamma = \Gamma_1 = \Gamma_3$ when $\kappa a = 0.1$ and $\kappa \ell = 10$. Notice that $a = (a_1 + a_2 + a_3)/3$ and $\ell = \ell_1 = \ell_2$. The maxima of G and G_{3D} occur at $\Gamma = 1$.

length scale. Hence the existence of the characteristic length scale, κ^{-1} , for a quasi-2D fluid completely changes the asymptotic size dependencies of the average velocity. This is an important finding of this chapter and highlights the essential difference between 2D and 3D microswimmers.

3.5 Asymmetric microswimmers

Since I have obtained the general expression of the geometric factor G for a three-disk microswimmer, as shown in Eq. (3.18), I discuss now the effects of structural asymmetry of a microswimmer on its geometric factor. We first set as $\ell_1 = \ell_2 = \ell$ and vary the two ratios between the disk sizes as defined by

$$\Gamma_1 = \frac{a_1}{a_2}, \quad \Gamma_3 = \frac{a_3}{a_2}, \quad (3.26)$$

whereas we keep, for instance, the sum of the three radii being fixed to $a_1 + a_2 + a_3 = 3a$. In Fig. 3.3, I plot the scaled geometric factor G/κ in Eq. (3.18) as a function of the two ratios Γ_1 and Γ_3 when $\kappa a = 0.1$ and $\kappa \ell = 10$. Notice that a/ℓ should be small within our expansion scheme and the color scale indicates the quantity $\log(G/\kappa)$. From this plot, I find that the maximum of the geometric

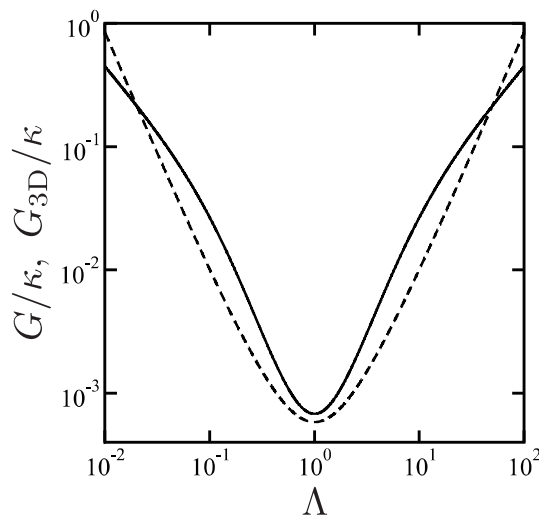


Figure 3.5: Plot of the scaled geometric factor G/κ (solid line) [see Eq. (3.18)] and G_{3D}/κ (dashed line) [see Eq. (3.24)] as a function of the asymmetry parameter $\Lambda = \ell_1/\ell_2$ [see Eq. (3.27)] when $\kappa a = 0.1$ and $\kappa \ell = 10$. Notice that $a = a_1 = a_2 = a_3$ and $\ell = (\ell_1 + \ell_2)/2$. The minima of G and G_{3D} occur at $\Lambda = 1$.

factor is realized when the disk size is identical, i.e., $\Gamma_1 = \Gamma_3 = 1$. In other words, any asymmetry in the disk size leads to a reduction of the average swimming velocity.

In Fig. 3.4, I further consider the case when $\Gamma_1 = \Gamma_3 = \Gamma$ (or, equivalently, $a_1 = a_3$), and plot G/κ as a function of Γ . Such a plot corresponds to a cross-section of Fig. 3.3 along the diagonal line. To compare the quasi-2D case with the 3D case, I also plot G_{3D}/κ [see Eq. (3.24)] as a function of Γ under the same condition. For G_{3D} , the ratios Γ_1 and Γ_3 correspond to those between the sphere radii. It should be also noted that Eq. (3.24) does not contain κ and it is used only to compare with the quasi-2D case. Although both G and G_{3D} are maximized at $\Gamma = 1$, the dependence on Γ is much weaker for G . This weak dependence originates from the logarithmic dependence of the disk mobility μ on the disk size a , as shown in Eq. (3.4).

Alternatively, one can set as $a_1 = a_2 = a_3 = a$ and vary the ratio between

the arm lengths defined by

$$\Lambda = \frac{\ell_1}{\ell_2}, \quad (3.27)$$

whereas we keep the sum of the two arm lengths being fixed to $\ell_1 + \ell_2 = 2\ell$. In Fig. 3.5, I plot the scaled geometric factors G/κ and G_{3D}/κ as a function of Λ when $\kappa a = 0.1$ and $\kappa\ell = 10$ as before. Here it is remarkable that both G and G_{3D} are minimized when $\Lambda = 1$. On the other hand, the overall behaviors of G and G_{3D} are rather similar because the chosen parameter value satisfies the condition $\kappa\ell \gg 1$ for which the coupling mobility M exhibits an algebraic dependence on the distance ℓ , as shown in Eq. (3.8).

3.6 Summary and discussion

In summary, I have proposed a model of 2D three-disk micromachine swimming in a quasi-2D supported membrane. In particular, I have obtained the average swimming velocity as a function of the disk size and the arm length. Due to the presence of the hydrodynamic screening length in the quasi-2D fluid, κ^{-1} , the geometric factor in the average velocity exhibits various asymptotic behaviors depending on the microswimmer size and the screening length. My result has been confirmed by the scaling argument for the geometric factor. I have also looked at the effects of structural asymmetry of a microswimmer, and found that the geometric factor is maximized when the disks are equal-sized, whereas it is minimized when the average arm lengths are identical.

At this point, a rough estimate of the characteristic length scales would be useful [3.25, 3.29, 3.31]. The membrane viscosity of lipid bilayers at physiological temperatures is approximately $\eta \approx 10^{-9}$ N·s/m and the viscosity of surrounding water is $\eta_s \approx 10^{-3}$ N·s/m². For supported membranes, we can approximate the height of the intervening solvent region as $h \approx 10^{-9}$ m. Hence we obtain $\kappa^{-1} = \sqrt{\eta h / \eta_s} \approx 3 \times 10^{-8}$ m. I note that this length scale is relatively small and the large scale behavior is expected for micron-sized swimmers.

In my model of a three-disk microswimmer, I have assumed that the three

disks are connected by two arms and their time-dependent motions are given by Eq. (3.14) [3.12, 3.13]. Alternatively, one can also consider a three-disk microswimmer in which the disks are connected by two elastic springs, while the natural length of each spring is assumed to undergo a prescribed cyclic change. Using the results in Ref. [3.17], one can immediately estimate the average quantity $\langle u_1 \dot{u}_2 - \dot{u}_1 u_2 \rangle$ in Eq. (3.15) and obtain the average velocity \bar{V} of an elastic 2D microswimmer. It can be generally shown that the swimming velocity increases with frequency in the low-frequency region, whereas in the high-frequency region, the average velocity decreases when the frequency is increased [3.17]. Such a behavior originates from the intrinsic spring relaxation dynamics of an elastic swimmer.

Although I have taken into account the hydrodynamic friction between the fluid membrane and the substrate through the friction coefficient λ in Eq. (3.1), the effect of intrinsic drag of the disks on the substrate was not considered in Eq. (3.3). One can naturally assume that the drag coefficient of a disk on the substrate is proportional to its area and is given by $\lambda_d \pi a^2$, where λ_d is the disk friction coefficient. In this case, the translational mobility coefficient in Eq. (3.3) will be modified [3.23]:

$$\mu(a) = \frac{1}{4\pi\eta} \left[\frac{(\kappa a)^2}{4} \left(1 + \frac{\lambda_d}{\lambda} \right) + \frac{\kappa a K_1(\kappa a)}{K_0(\kappa a)} \right]^{-1}. \quad (3.28)$$

Notice that the correction term due to λ_d/λ gives rise to a contribution that is independent of λ . Since only the coefficient of $(\kappa a)^2$ is altered when compared with Eq. (3.3), the drag acting on the disks modifies my result only up to a numerical factor when $\kappa a \gg 1$. This means that the asymptotic scaling behaviors in Sec. 3.4 are not affected by the drag forces on the disks. In principle, the disk friction coefficient can be different for different disks. Such an effect can be effectively taken into account by considering different disk radii as long as they are much larger than the screening length κ^{-1} .

In this chapter, I have discussed the behavior of a 2D microswimmer in a

quasi-2D fluid that is characterized by a hydrodynamic screening length, κ^{-1} . It should be noted, however, that we encounter a similar situation in which a 3D micromachine swims in a structured viscoelastic fluid having a characteristic length scale. According to my preliminary result, I find that the frequency dependence of the average velocity exhibits fairly complex behaviors depending on the machine size relative to the characteristic length scale of the surrounding structured fluid. Details of such an investigation will be reported elsewhere [3.32].

In the future, we shall also investigate the case when the surrounding bulk fluid is viscoelastic [3.30]. Such a study will enable us to obtain the frequency dependent complex viscosity of the surrounding 3D fluid by measuring the velocity of a 2D microswimmer in a membrane [3.33]. Such a method will provide us with a new type of non-contact surface microrheology.

References

- [3.1] S. J. Singer and G. L. Nicolson, *Science* **175**, 720 (1972).
- [3.2] B. Alberts, A. Johnson, P. Walter, J. Lewis, and M. Raff, *Molecular Biology of the Cell* (Garland Science, New York, 2015).
- [3.3] P. G. Saffman and M. Delbrück, *Proc. Natl. Acad. Sci. USA.* **72**, 3111 (1975).
- [3.4] P. G. Saffman, *J. Fluid Mech.* **73**, 593 (1976).
- [3.5] Y. Togashi and A. S. Mikhailov, *Proc. Natl. Acad. Sci. USA.* **104**, 8697 (2007).
- [3.6] J.-B. Manneville, P. Bassereau, D. Lévy, and P. Prost, *Phys. Rev. Lett.* **82**, 4356 (1999).
- [3.7] J.-B. Manneville, P. Bassereau, S. Ramaswamy, and J. Prost, *Phys. Rev. E* **64**, 021908 (2001).

-
- [3.8] M. D. El Alaoui Faris, D. Lacoste, J. Pécrcéaux, J.-F. Joanny, J. Prost, and P. Bassereau, *Phys. Rev. Lett.* **102**, 038102 (2009).
- [3.9] E. Lauga and T. R. Powers, *Rep. Prog. Phys.* **72**, 096601 (2009).
- [3.10] E. M. Purcell, *Am. J. Phys.* **45**, 3 (1977).
- [3.11] E. Lauga, *Soft Matter* **7**, 3060 (2011).
- [3.12] A. Najafi and R. Golestanian, *Phys. Rev. E* **69**, 062901 (2004).
- [3.13] R. Golestanian and A. Ajdari, *Phys. Rev. E* **77**, 036308 (2008).
- [3.14] G. Grosjean, M. Hubert, G. Lagubeau, and N. Vandewalle, *Phys. Rev. E* **94**, 021101 (2016).
- [3.15] G. Grosjean, M. Hubert, and N. Vandewalle, *Adv. Colloid Interface Sci.* **255**, 84 (2018).
- [3.16] J. Pande, L. Merchant, T. Krüger, J. Harting, and A.-S. Smith, *New J. Phys.* **19**, 053024 (2017).
- [3.17] K. Yasuda, Y. Hosaka, M. Kuroda, R. Okamoto, and S. Komura, *J. Phys. Soc. Jpn.* **86**, 093801 (2017).
- [3.18] M.-J. Huang, A. S. Mikhailov, and H.-Y. Chen, *Eur. Phys. J. E* **35**, 119 (2012).
- [3.19] S. Komura, S. Ramachandran, and M. Imai, in *Non-Equilibrium Soft Matter Physics*, edited by S. Komura and T. Ohta (World Scientific, Singapore, 2012), p. 197.
- [3.20] S. Komura and D. Andelman, *Adv. Colloid Interface Sci.* **208**, 34 (2014).
- [3.21] E. Sackmann, *Science* **271**, 43 (1996).
- [3.22] M. Tanaka and E. Sackmann, *Nature* **437**, 656 (2005).

- [3.23] E. Evans and E. Sackmann, *J. Fluid Mech.* **194**, 553 (1988).
- [3.24] K. Seki and S. Komura, *Phys. Rev. E* **47**, 2377 (1993).
- [3.25] S. Ramachandran, S. Komura, M. Imai, and K. Seki, *Eur. Phys. J. E* **31**, 303 (2010).
- [3.26] H. Diamant, *J. Phys. Soc. Jpn.* **78**, 041002 (2009).
- [3.27] S. Ramachandran, S. Komura, and G. Gompper, *EPL* **89**, 56001 (2010).
- [3.28] N. Oppenheimer and H. Diamant, *Phys. Rev. E* **82**, 041912 (2010).
- [3.29] S. Ramachandran, S. Komura, K. Seki, and G. Gompper, *Eur. Phys. J. E* **34**, 46 (2011).
- [3.30] S. Komura, S. Ramachandran, and K. Seki, *EPL* **97**, 68007 (2012).
- [3.31] Y. Hosaka, K. Yasuda, R. Okamoto, and S. Komura, *Phys. Rev. E* **95**, 052407 (2017).
- [3.32] K. Yasuda, R. Okamoto, and S. Komura, *EPL* **123**, 34002 (2018).
- [3.33] K. Yasuda, R. Okamoto, and S. Komura, *J. Phys. Soc. Jpn.* **86**, 043801 (2017).

Chapter 4

Three-Sphere Microswimmer in a Structured Fluid

I discuss the locomotion of a three-sphere microswimmer in a viscoelastic structured fluid characterized by typical length and time scales. I derive a general expression to link the average swimming velocity to the sphere mobilities. In this relationship, a viscous contribution exists when the time-reversal symmetry is broken, whereas an elastic contribution is present when the structural symmetry of the microswimmer is broken. As an example of a structured fluid, we consider a polymer gel, which is described by a “two-fluid model”. I demonstrate in detail that the competition between the swimmer size and the polymer mesh size gives rise to the rich dynamics of a three-sphere microswimmer.

4.1 Introduction

Microswimmers are tiny machines, such as sperm cells or motile bacteria, that swim in a fluid and are expected to be relevant to microfluidics and microsystems [4.1]. By transforming chemical energy into mechanical work, microswimmers can change their shapes and move in viscous environments. The fluid forces acting on the length scale of microswimmers are governed by the effect of viscous dissipation. According to Purcell’s scallop theorem [4.2], time-

reversal body motion cannot be used for locomotion in a Newtonian fluid. As one of the simplest models exhibiting broken time-reversal symmetry, Najafi and Golestanian proposed a three-sphere microswimmer [4.3, 4.4] in which three in-line spheres are linked by two arms of varying lengths. This model is suitable for analytical studies because the tensorial structure of the fluid motion can be neglected in its translational motion. Recently, such a microswimmer has been experimentally realized [4.5, 4.6].

For microswimmers in general situations, however, the surrounding fluid is not necessarily purely viscous but viscoelastic. Several studies have discussed the swimming behaviors of micromachines in different types of viscoelastic fluids [4.7–4.11]. In particular, Lauga showed that the Scallop theorem in a viscoelastic fluid breaks down if the squirmer has a fore-aft asymmetry in its surface velocity distribution [4.7]. In a previous chapter, I discussed the locomotion of a three-sphere microswimmer in a viscoelastic medium and derived a relationship linking the average swimming velocity to the frequency-dependent viscosity of the surrounding medium [4.12]. I demonstrated that the absence of the time-reversal symmetry of the swimmer motion is reflected in the real part of the viscosity, whereas the absence of the structural symmetry of the swimmer is reflected in its imaginary part.

So far, investigations into the swimming behaviors of micromachines have been limited to homogeneous viscoelastic fluids without any internal structures. However, one of the fundamental and characteristic features of viscoelastic soft matter is that it contains various intermediate mesoscopic structures and behaves as a structured fluid [4.13]. The existence of such internal length scales significantly affects the rheological properties of soft matter [4.14]. In this chapter, I address the effects of the intermediate structures of the surrounding viscoelastic fluid on the locomotion of a three-sphere microswimmer. Because a three-sphere microswimmer is also characterized by its own size, my main interest is to find out how the average swimming velocity depends on the relative magnitudes of

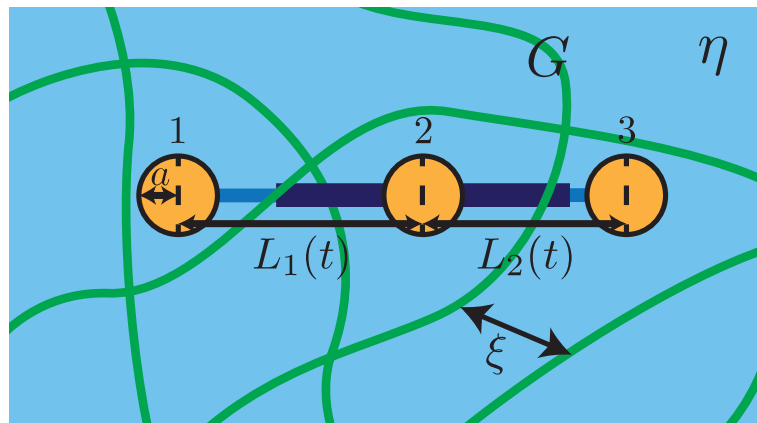


Figure 4.1: A three-sphere micromachine swimming in a structured fluid such as a polymer gel. Three identical spheres of radius a are connected by arms with lengths $L_1(t)$ and $L_2(t)$ and undergo time-dependent cyclic motions. According to the two-fluid model, the polymer gel consists of an elastic network characterized by a constant shear modulus G and a viscous fluid characterized by a constant shear viscosity η . The elastic and fluid components are coupled via mutual friction. The length scale ξ characterizes the typical internal structure of the elastic network, e.g., its mesh size.

the swimmer's size and the characteristic length of the surrounding fluid.

Generalizing my previous work [4.12], I first obtain the average velocity of a three-sphere microswimmer moving in a structured fluid, which is characterized by typical length and time scales. As an example of a structured fluid, we employ a “two-fluid model” that has been broadly used to describe the dynamics of polymer gels [4.15–4.17]. Recently, the response of a polymer network to the motion of a rigid sphere has been investigated within this two-fluid model [4.18–4.20]. I calculate the frequency dependency of the average velocity of a three-sphere microswimmer in a two-fluid gel and obtain its various asymptotic expressions by changing the swimmer size. The competition between the swimmer size and the polymer mesh size gives rise to the rich dynamics of microswimmers. Even though I primarily discuss the two-fluid model here, my result can be applied to various types of structured fluids.

4.2 Microswimmer in a structured fluid

As shown in Fig. 4.1, I consider a microswimmer consisting of three rigid spheres of the same radius a that are connected by two arms of variable lengths L_1 and L_2 [4.3, 4.4]. I assume that the motion of the arms is prescribed by two time-dependent functions $L_1(t), L_2(t) \gg a$. Then the velocity of each sphere V_i ($i = 1, 2, 3$) should satisfy the conditions $\dot{L}_1(t) = V_2(t) - V_1(t)$ and $\dot{L}_2(t) = V_3(t) - V_2(t)$, where the dot indicates the time derivative. The surrounding fluid exerts a force F_i ($i = 1, 2, 3$) on each sphere, which we assume to be along the swimmer axis. Because we are interested in the autonomous net locomotion of the swimmer, there are no external forces acting on the spheres. This leads to the force-free condition: $F_1(t) + F_2(t) + F_3(t) = 0$.

Within the linear response theory, the velocity and force acting on a sphere of radius a are related in the Fourier domain by $V_i(\omega) = \mu[a, \omega]F_i(\omega)$, where $V(\omega) = \int_{-\infty}^{\infty} dt V(t)e^{-i\omega t}$ (with the same form for $F(\omega)$) denotes the Fourier transform and $\mu[a, \omega] = \int_0^{\infty} dt \mu(a, t)e^{-i\omega t}$ gives the frequency-dependent self-mobility. Similarly, the force F_j acting on the j -th sphere at x_j and the induced velocity V_i of the i -th sphere at x_i are related by $V_i(\omega) = M[r, \omega]F_j(\omega)$, where $r = x_i - x_j \gg a$ and $M[r, \omega]$ is the frequency-dependent longitudinal coupling mobility.

I further assume that the arm deformations are relatively small, and given by $L_1(t) = \ell + u_1(t)$ and $L_2(t) = \ell + u_2(t)$, where ℓ is a constant length that satisfies $\ell \gg u_1(t), u_2(t)$. I consider the case when the two arms undergo the simplest periodic motions [4.3, 4.4]: $u_1(t) = d_1 \cos(\Omega t)$ and $u_2(t) = d_2 \cos(\Omega t - \phi)$, where d_1 and d_2 are the amplitudes of the oscillatory motions, Ω is the common arm frequency, and ϕ is the mismatch in the phases between the two arms. When the arm motions are given, the above set of equations is sufficient to solve for the six unknown quantities V_i and F_i . The swimming velocity is obtained by averaging the velocities of the three spheres, i.e., $V = (V_1 + V_2 + V_3)/3$.

Consider a viscoelastic structured fluid that is characterized by a character-

istic length scale ξ and a characteristic time scale τ . I assume that the above mentioned mobilities are expressed by the following scaling forms:

$$\mu[a, \omega] = \frac{\hat{\mu}[a/\xi, \omega\tau]}{6\pi\eta_0 a}, \quad M[r, \omega] = \frac{\hat{M}[r/\xi, \omega\tau]}{4\pi\eta_0 \ell}, \quad (4.1)$$

where $\hat{\mu}$ and \hat{M} are the dimensionless scaling functions and η_0 is the zero-frequency shear viscosity. Even if there are more than two length or time scales, the above assumption is still valid because only the dimensionless ratios between the different scales enter into the scaling functions. In other words, if there are several length scales $\xi_1, \xi_2, \xi_3, \dots$ and several time scales $\tau_1, \tau_2, \tau_3, \dots$, the dimensionless mobility can be expressed as

$$\hat{\mu}[a/\xi_1, \omega\tau_1; \xi_2/\xi_1, \xi_3/\xi_1, \dots; \tau_2/\tau_1, \tau_3/\tau_1, \dots], \quad (4.2)$$

and similarly for \hat{M} . Under this assumption, we perform an expansion of the swimming velocity to the leading order in a/ℓ , d_1/ℓ , and d_2/ℓ . After performing the time integration over a full cycle, we obtain the average swimming velocity:

$$\begin{aligned} \bar{V} &\approx \frac{d_1 d_2 a \Omega}{48 \ell^2} (\hat{\mu}[a/\xi, \Omega\tau]^{-1} + \hat{\mu}[a/\xi, -\Omega\tau]^{-1}) \\ &\times \left(8\hat{M}[\ell/\xi, 0] - \hat{M}[2\ell/\xi, 0] + 2\ell(-4\partial\hat{M}[\ell/\xi, 0] + \partial\hat{M}[2\ell/\xi, 0]) \right) \sin \phi \\ &+ \frac{i(d_1^2 - d_2^2)a\Omega}{96\ell^2} (\hat{\mu}[a/\xi, \Omega\tau]^{-1} - \hat{\mu}[a/\xi, -\Omega\tau]^{-1}) \\ &\times \left(4\hat{M}[\ell/\xi, 0] + \hat{M}[2\ell/\xi, 0] - 2\ell(2\partial\hat{M}[\ell/\xi, 0] + \partial\hat{M}[2\ell/\xi, 0]) \right), \quad (4.3) \end{aligned}$$

where

$$\partial\hat{M}[\ell/\xi, 0] = \lim_{\omega\tau \rightarrow 0} \left. \frac{\partial\hat{M}[r/\xi, \omega\tau]}{\partial r} \right|_{r=\ell}, \quad (4.4)$$

[see the Appendix 4.A for the full derivation]. This is a generalization of my previous result [4.12] and is the main result of this chapter.

The first term in Eq. (4.3) can be regarded as a viscous contribution, \bar{V}_v , and is present only if the time-reversal symmetry of the arm motion is broken, i.e., $\phi \neq 0, \pi$. The second term, conversely, corresponds to an elastic contribution, \bar{V}_e , and exists only when the structural symmetry of the swimmer is broken, i.e., $d_1 \neq d_2$. In other words, even if the time-reversal symmetry of the

swimmer motion is not broken, i.e., $\phi = 0, \pi$, the swimmer can still move in a viscoelastic medium because of the second elastic term as long as its structural symmetry is broken, i.e., $d_1 \neq d_2$. I used the condition $a \ll \ell$ when deriving Eq. (4.3), but nothing has been assumed concerning the relative magnitudes between the swimmer size, a and ℓ , and the characteristic length of the fluid, ξ . Therefore, Eq. (4.3) offers a very general velocity expression for a three-sphere microswimmer moving in a structured fluid.

Although Eq. (4.3) is applicable to any structured fluid, some special cases are worth discussing. For a purely viscous fluid, the scaling functions in Eq. (4.1) are given by $\hat{\mu} = 1$ and $\hat{M} = 1$; therefore, Eq. (4.3) reduces to the average velocity obtained by Golestanian and Ajdari [4.4]. Further, for a viscoelastic fluid without any internal structure, the scaling functions are simply given by $\hat{\mu} = \eta_0/\eta[\omega]$ and $\hat{M} = \eta_0/\eta[\omega]$, where $\eta[\omega]$ is the frequency-dependent complex viscosity. In such a homogeneous but viscoelastic fluid, Eq. (4.3) reduces to Eq. (13) in Ref. [4.12].

I note that the above derivation has been limited within the linear response theory because linear relationships between forces and velocities have been assumed. Such an assumption of the linear viscoelasticity is generally justified when the strain amplitude is small enough [4.21]. For a three-sphere microswimmer, this condition is given by $d_1/\ell \ll 1$ and $d_2/\ell \ll 1$ which have been indeed used in the derivation of Eq. (4.3). Otherwise, one needs to take into account nonlinear viscoelastic effects such as a shear thinning behavior [4.14].

4.3 Two-fluid model for a gel

As a simple example of various structured fluids, I consider here a polymer gel described by the two-fluid model. As schematically described in Fig. 4.1, there are two dynamical fields in this model: the displacement field $\mathbf{u}(\mathbf{r}, t)$ of the elastic network and the velocity field $\mathbf{v}(\mathbf{r}, t)$ of the permeating fluid. When inertial effects are neglected, the linearized coupled equations for these two field

variables are given by

$$0 = G\nabla^2 \mathbf{u} + (K + G/3)\nabla(\nabla \cdot \mathbf{u}) - \Gamma \left(\frac{\partial \mathbf{u}}{\partial t} - \mathbf{v} \right), \quad (4.5)$$

$$0 = \eta\nabla^2 \mathbf{v} - \nabla p - \Gamma \left(\mathbf{v} - \frac{\partial \mathbf{u}}{\partial t} \right) + \mathbf{f}. \quad (4.6)$$

Here, G and K are the shear and compression moduli of the elastic network, respectively, η is the shear viscosity of the fluid, $p(\mathbf{r}, t)$ is the pressure field, and $\mathbf{f}(\mathbf{r}, t)$ is the external force density acting on the fluid component. The elastic and fluid components are coupled via the mutual friction, which is characterized by the friction coefficient Γ . When the volume fraction of the elastic component is small, we further require the incompressibility condition: $\nabla \cdot \mathbf{v} = 0$. The above two-fluid model contains the characteristic length $\xi = (\eta/\Gamma)^{1/2}$ and the characteristic time $\tau = \eta/G$. The former length scale roughly corresponds to the mesh size of a polymer network, and the latter time scale sets the viscoelastic time. Hereafter, I introduce a dimensionless ratio defined as $\epsilon = [(K + 4G/3)/G]^{1/2}$.

Diamant calculated the self-mobility of a sphere in a two-fluid gel, which depends on the choice of the boundary condition at the surface of the sphere [4.18]. Here I consider the case of “a sticking fluid and a free network”, i.e., a stick boundary condition is used for the fluid while the network does not exchange stress with the sphere. In other words, the network moves only because of its coupling to the fluid. The full expression of the self-mobility μ is given in the Appendix 4.B [4.18], and here, I show only its limiting behaviors. In the low-frequency limit, $\omega\tau \rightarrow 0$, μ becomes

$$\mu[a, \omega] \approx \frac{9}{6\pi\eta a(9 + 9\hat{a} + \hat{a}^2)} + \frac{i\omega\tau}{6\pi\eta\xi} \frac{(4 + 3\epsilon^2)\hat{a}^3 + 36\epsilon^2\hat{a}^2 + 162\epsilon^2\hat{a} + 81\epsilon^2}{2(9 + 9\hat{a} + \hat{a}^2)^2\epsilon^2}, \quad (4.7)$$

where $\hat{a} = a/\xi$ and one can take further limits depending on the magnitude of \hat{a} . In the high-frequency limit, $\omega\tau \rightarrow \infty$, μ becomes

$$\mu[a, \omega] \approx \frac{1}{6\pi\eta a} - \frac{1}{6\pi\eta a(i\omega\tau)}. \quad (4.8)$$

This expression is equivalent to writing the mobility as $\mu[a, \omega] \approx 1/(6\pi\eta_b a)$, with an effective viscosity of $\eta_b = \eta[1 + 1/(i\omega\tau)]$. Therefore, the above two-fluid model reduces to the Kelvin-Voigt model at high-frequencies [4.14].

I previously obtained a general expression for the coupling mobility M connecting the velocity \mathbf{v} and the force \mathbf{f} in the two-fluid model [4.22, 4.23], which is also given in the Appendix 4.B. For small distances, $r/\xi \rightarrow 0$, the coupling mobility is

$$M[r, \omega] \approx \frac{1}{4\pi\eta r} - \frac{1}{6\pi\eta\xi(1 + i\omega\tau)^{1/2}}, \quad (4.9)$$

and consequently, the gel is nearly purely viscous. Conversely, for sufficiently large distances, $r/\xi \rightarrow \infty$, the coupling mobility is

$$M[r, \omega] \approx \frac{1}{4\pi\eta_b r} + \frac{\xi^2}{2\pi\eta r^3} \frac{1}{(1 + i\omega\tau)^2}. \quad (4.10)$$

4.4 Average velocities in a two-fluid gel

Next I discuss the average velocity of a three-sphere microswimmer in a two-fluid gel and investigate its frequency as well as size dependencies. Recall that there are two lengths that measure the size of a three-sphere microswimmer: the sphere radius a and the average arm length ℓ , with the condition $a \ll \ell$. Because the surrounding gel is characterized by the network mesh size, ξ , the following three different situations can be distinguished: (i) a large swimmer when $a \gg \xi$ and $\ell \gg \xi$, (ii) a medium swimmer when $a \ll \xi$ and $\ell \gg \xi$, and (iii) a small swimmer when $a \ll \xi$ and $\ell \ll \xi$. In each case, following the procedure in the Appendix 4.A, I numerically solve for V_i and F_i to calculate the average velocity \bar{V} without making an expansion in terms of a/ℓ . These numerical results are plotted by the solid lines in Fig. 4.2, whereas the analytical results obtained from Eq. (4.3) are plotted by the dotted lines with the same colors. In Fig. 4.2, the parameters a/ξ and ℓ/ξ are chosen in such a way that the condition $a/\ell \ll 1$ is always satisfied for a three-sphere microswimmer. Moreover, d_1/ℓ and d_2/ℓ are also small enough to ensure that the assumption of linear viscoelasticity is

appropriate.

In Figs. 4.2(a) and (b), I separately plot the viscous \bar{V}_v and elastic \bar{V}_e contributions, respectively, for a large swimmer as a function of the scaled frequency $\Omega\tau$. The behavior of \bar{V}_v in Fig. 4.2(a) is remarkable because it exhibits a non-monotonic dependence on Ω . A careful analysis reveals that it behaves as $\bar{V}_v \sim \Omega \rightarrow \Omega^{-1/2} \rightarrow \Omega \rightarrow \Omega^{-1} \rightarrow \Omega$ as Ω increases. This non-monotonic behavior is more pronounced for larger sphere sizes such as $a/\xi = 100$ (green). On the other hand, the frequency dependence of the elastic contribution, \bar{V}_e , crosses over as $\bar{V}_e \sim \Omega^2 \rightarrow \Omega^0$.

The above results can be reproduced by Eq. (4.3) when we use the full expressions of the two-fluid mobilities μ and M (most of the dotted lines in Fig. 4.2 are invisible because they almost coincide with the solid lines). Further, Eq. (4.3) provides us with various asymptotic expressions. For example, I first discuss the limit of $\Omega\tau \rightarrow 0$ in \bar{V}_v . Using the first term of Eq. (4.7) and the second term of Eq. (4.10), we obtain

$$\bar{V}_v \approx \frac{31d_1d_2a^3\Omega}{144\ell^4} \sin\phi, \quad (4.11)$$

which is proportional to Ω . The complex non-monotonic behaviors in the intermediate frequencies are separately discussed in the Appendix 4.C. In the limit of $\Omega\tau \rightarrow \infty$, we use the first term of Eq. (4.8) and the second term of Eq. (4.10) to obtain

$$\bar{V}_v \approx \frac{31d_1d_2\xi^2a\Omega}{16\ell^4} \sin\phi. \quad (4.12)$$

By evaluating the elastic term in Eq. (4.3), one can also obtain the asymptotic expressions for \bar{V}_e . In the limit of $\Omega\tau \rightarrow 0$, we use the second terms of Eqs. (4.7) and (4.10) to obtain

$$\bar{V}_e \approx \frac{17(d_1^2 - d_2^2)a^5}{5184\ell^4\xi^2\tau} \frac{4 + 3\epsilon^2}{\epsilon^2} (\Omega\tau)^2, \quad (4.13)$$

which is proportional to Ω^2 . In the limit of $\Omega\tau \rightarrow \infty$, the second terms of

Eqs. (4.8) and (4.10) yield

$$\bar{V}_e \approx \frac{17(d_1^2 - d_2^2)\xi^2 a}{32\ell^4 \tau}, \quad (4.14)$$

which is independent of Ω . Notice that the crossover frequency separating the different scaling regimes is strongly dependent on a/ξ . For example, the crossover frequency between Eqs. (4.13) and (4.14) roughly scales as $(\Omega\tau)^* \sim (a/\xi)^{-2}$. This means that one can extract information concerning the internal structure of the surrounding medium by observing the average swimming velocity. Moreover, the non-linear dependence on the sphere size, such as $\bar{V}_v \sim a^3$ in Eq. (4.11) or $\bar{V}_e \sim a^5$ in Eq. (4.13), is also a unique feature of a two-fluid gel.

For a medium swimmer ($a \ll \xi$ and $\ell \gg \xi$), I plot the numerical results of \bar{V}_v and \bar{V}_e in Figs. 4.2(c) and (d), respectively. In Fig. 4.2(c), we find $\bar{V}_v \sim \Omega$ over the entire frequency range. This behavior is essentially explained by Eq. (4.12), which was obtained for the large swimmer case. The elastic contribution in Fig. 4.2(d), conversely, crosses over as $\bar{V}_e \sim \Omega^2 \rightarrow \Omega^{1/2} \rightarrow \Omega^0$, where the Ω -independent behavior can be explained by Eq. (4.14) as before. In the Appendix 4.C, I show the asymptotic expressions for smaller frequencies [see Eqs. (4.54) and (4.55)].

Finally, I numerically plot \bar{V}_v and \bar{V}_e for a small swimmer ($a \ll \xi$ and $\ell \ll \xi$) in Figs. 4.2(e) and (f), respectively. The viscous contribution shows a linear dependence, $\bar{V}_v \sim \Omega$. This is reasonable because the combination of the first terms in Eqs. (4.8) and (4.9) simply represents a purely viscous fluid. The elastic contribution plotted in Fig. 4.2(f) crosses over as $\bar{V}_e \sim \Omega^2 \rightarrow \Omega^{3/2} \rightarrow \Omega^{1/2} \rightarrow \Omega^0$. Even though the first two scaling behaviors cannot be obtained analytically, the last two behaviors are given in the Appendix 4.C [see Eqs. (4.56) and (4.57)]. It should be mentioned here that Eq. (4.3) does not reproduce the numerical result in Fig. 4.2(f) because the lowest expansion in terms of a/ℓ is inappropriate for this limit. Hence the dotted lines deviate from the solid lines Fig. 4.2(f) especially for relatively smaller $\Omega\tau$ values.

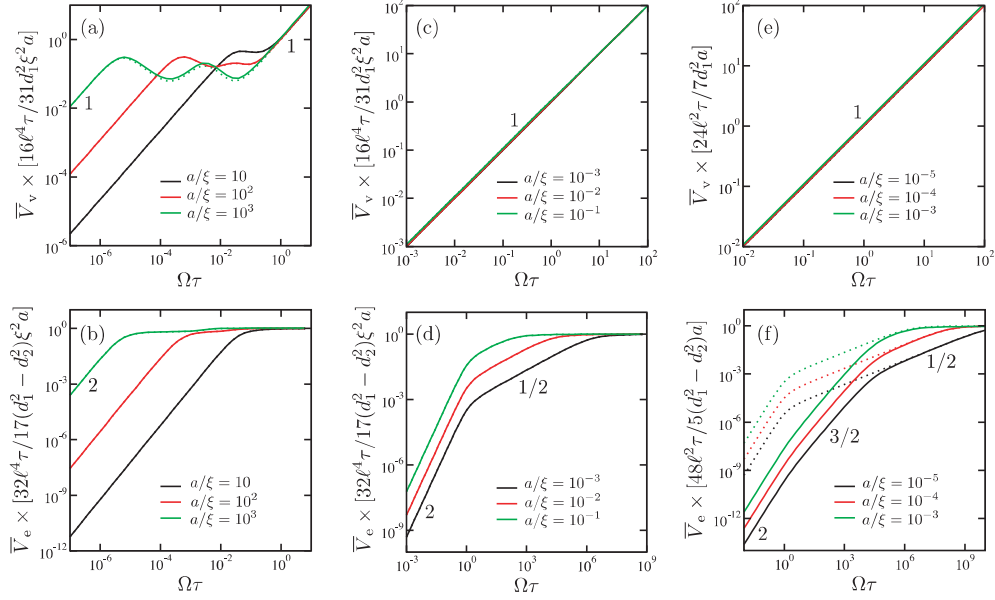


Figure 4.2: Plots of the average swimming velocity \bar{V} as a function of the scaled frequency $\Omega\tau$ for a three-sphere micromachine swimming in a polymer gel with $\epsilon = [(K + 4G/3)/G]^{1/2} = \sqrt{14/3} \approx 2.16$. The solid lines are the numerical results explained in the text, whereas the dotted lines (with the same colors) are the analytical results obtained from Eq. (4.3). The analytical dotted curves are invisible when they coincide with the numerical solid curves. The numbers indicate the slopes representing the exponents of the power-law behaviors. (a) The scaled viscous contribution \bar{V}_v and (b) the scaled elastic contribution \bar{V}_e for a large swimmer ($a \gg \xi$, $\ell \gg \xi$). The different colors correspond to the different a/ξ values shown in the graphs; here, we have chosen $\ell/\xi = 10^4$. The other parameters are $\phi = \pi/2$ and $d_1/\ell = d_2/\ell = 10^{-2}$ in (a) and $d_1 = 2d_2$ and $d_2/\ell = 10^{-2}$ in (b). (c) The scaled \bar{V}_v and (d) scaled \bar{V}_e for a medium swimmer ($a \ll \xi$, $\ell \gg \xi$). The different colors correspond to the different a/ξ values shown in the graphs; here, we have chosen $\ell/\xi = 10^4$. The other parameters are the same as those in (a) and (b). (e) The scaled \bar{V}_v and (d) scaled \bar{V}_e for a small swimmer ($a \ll \xi$, $\ell \ll \xi$). The different colors correspond to the different a/ξ values shown in the graphs; here, we have chosen $\ell/\xi = 10^{-2}$. The other parameters are the same as those in (a) and (b). Notice that in all these plots, a/ξ and ℓ/ξ are chosen in such a way that $a/\ell \ll 1$ is always satisfied.

4.5 Summary and discussion

So far, I have primarily discussed the motion of a three-sphere microswimmer in a polymer gel described by the two-fluid model. However, the importance of my work is not restricted to these specific models. The prediction of the average velocity in Eq. (4.3) is applicable to any structured viscoelastic fluid that has an intermediate length scale and a characteristic time scale. For example, one can also discuss the motion of a microswimmer in a polymer solution that is described by a different “two-fluid model” [4.24, 4.25]. In addition, it is interesting to discuss the dynamics of three-sphere microswimmers in liquid crystals [4.26], which typically exhibit complex rheological behavior depending on their different phases [4.27].

Furthermore, we encounter a similar situation when we consider the motion of a three-disk microswimmer immersed in a quasi-2D fluid membrane [4.28]. Owing to the presence of the hydrodynamic screening length in the quasi-2D fluid, the geometric factor appearing in the average velocity exhibits various asymptotic behaviors when changing the ratio between the swimmer size and the screening length. The result in Ref. [4.28] can be obtained from Eq. (4.3) using the mobility of the disk and the coupling mobility in a quasi-2D fluid.

At this point, it is useful to give some numbers related to realistic microswimmers and systems described by a two-fluid model. Let us first consider a homogeneous sample of entangled F-actin network whose mesh size ξ can be controlled by the actin monomer concentration c as $\xi = 0.3/\sqrt{c}$ (ξ in μm and c in mg/ml) [4.19, 4.20]. Hence $\xi \approx 1 \mu\text{m}$ for $c \approx 0.1 \text{ mg/ml}$. On the other hand, a typical size of colloidal particles used in microrheology experiments is $a \approx 0.5 \mu\text{m}$ [4.29]. If we assume that one can construct a three-sphere microswimmer by connecting these colloidal particles, its whole size (corresponding to ℓ) would amount to several microns, which is comparable to a typical size of living microorganisms such as bacteria. Since a magnitude relation $a < \xi < \ell$ holds in this case, a living microorganism swimming in an actin network may

correspond to a medium swimmer [see Fig. 4.3(c) and (d)].

On the other hand, a three-sphere swimmer has been experimentally realized by using ferromagnetic particles at an air-water interface and by applying an oscillating magnetic field [4.5, 4.6]. In this experiment, the size of spheres is about $a \approx 200 \mu\text{m}$ and the rest length of the bonds is roughly $\ell \approx 1 \text{ mm}$. Hence such a model swimmer behaves as a large swimmer in an actin network [see Fig. 4.3(a) and (b)], since the mesh size is much smaller, i.e., $\xi \ll a < \ell$. Such a comparison shows that the swimming behaviors of a microorganism and a ferromagnetic swimmer are essentially different in a structured fluid such as F-actin networks due to the presence of the characteristic length scale ξ . This is the main message of the present work.

Concerning the characteristic time scale τ of a two-fluid model, we shall refer to a number that was measured for F-actin networks [4.19, 4.20] by using microrheology techniques [4.29]. With the water viscosity $\eta \approx 10^{-3} \text{ Pa}\cdot\text{s}$ and the measured shear modulus $G \approx 10^{-1} \text{ Pa}$ for a F-actin network, we obtain the viscoelastic time scale as $\tau = \eta/G \approx 10^{-2} \text{ s}$. For a typical microorganism and a model swimmer mentioned above, characteristic frequencies are about $\Omega \approx 10^2 \text{ Hz}$ [4.1] and 1 Hz [4.5, 4.6], respectively. Hence the corresponding Deborah numbers for these two cases are $\text{De} \approx 1$ (microorganism) and 10^{-2} (model swimmer) which are both considered in Fig. 4.3.

Finally, I note that Fu *et al.* analyzed the swimming behavior of an infinite sheet undergoing transverse traveling-wave deformations in a two-fluid gel [4.30]. They demonstrated that the boundary conditions between the sheet and the network significantly affect the swimming speed. In my study, I considered only the case of “a sticking fluid and a free network” for the boundary condition between the sphere and the gel. Different situations such as “a sticking fluid and a sticking network” case or “a sticking fluid and a slipping network” case, as discussed in detail in Ref. [4.18], will lead to different swimming behaviors because the self-mobility of the spheres is modified. Although several deficiencies

of the two-fluid model have been explicitly pointed out [4.18], such investigations are left to future studies.

To summarize, I discussed the locomotion of a three-sphere microswimmer in a viscoelastic structured fluid with typical length and time scales. I derived a general expression for the average swimming velocity, Eq. (4.3), which includes both viscous and elastic contributions. To illustrate my result, I used the two-fluid model for a polymer gel and demonstrated that the average velocity exhibits various asymptotic behaviors depending on the swimmer size. Because one can extract information concerning the internal structure of the surrounding fluid from observations of the motion of a microswimmer, the present theory offers a new approach to active microrheology [4.29].

4.A Derivation of Eq. (4.3)

When the conditions $u_1(t), u_2(t) \ll \ell$ are satisfied, the equations of motion of the three spheres are given by [4.12]

$$\begin{aligned} V_1(\omega) \approx & \mu[a, \omega]F_1(\omega) + M[\ell, \omega]F_2(\omega) + \partial M[\ell, \omega] \frac{u_1(\omega) * F_2(\omega)}{2\pi} \\ & + M[2\ell, \omega]F_3(\omega) + \partial M[2\ell, \omega] \frac{[u_1(\omega) + u_2(\omega)] * F_3(\omega)}{2\pi}, \end{aligned} \quad (4.15)$$

$$\begin{aligned} V_2(\omega) \approx & M[\ell, \omega]F_1(\omega) + \partial M[\ell, \omega] \frac{u_1(\omega) * F_1(\omega)}{2\pi} + \mu[a, \omega]F_2(\omega) \\ & + M[\ell, \omega]F_3(\omega) + \partial M[\ell, \omega] \frac{u_2(\omega) * F_3(\omega)}{2\pi}, \end{aligned} \quad (4.16)$$

$$\begin{aligned} V_3(\omega) \approx & M[2\ell, \omega]F_1(\omega) + \partial M[2\ell, \omega] \frac{[u_1(\omega) + u_2(\omega)] * F_1(\omega)}{2\pi} \\ & + M[\ell, \omega]F_2(\omega) + \partial M[\ell, \omega] \frac{u_2(\omega) * F_2(\omega)}{2\pi} + \mu[a, \omega]F_3(\omega), \end{aligned} \quad (4.17)$$

where $\partial \hat{M}[\ell, \omega] = (\partial \hat{M}[r, \omega] / \partial r)_{r=\ell}$ and we have used the convolution defined by $f(\omega) * g(\omega) = \int_{-\infty}^{\infty} d\omega' f(\omega - \omega')g(\omega')$.

Since the arm frequency is Ω , we assume that the velocities and the forces of the three spheres can generally be written as [4.12]

$$V_i(\omega) = V_{i,0} \delta(\omega) + \sum_{n=1}^{\infty} [V_{i,n} \delta(\omega + n\Omega) + V_{i,-n} \delta(\omega - n\Omega)], \quad (4.18)$$

$$F_i(\omega) = F_{i,0} \delta(\omega) + \sum_{n=1}^{\infty} [F_{i,n} \delta(\omega + n\Omega) + F_{i,-n} \delta(\omega - n\Omega)]. \quad (4.19)$$

Substituting the assumed arm motions $u_1(t) = d_1 \cos(\Omega t)$, $u_2(t) = d_2 \cos(\Omega t - \phi)$ and (4.18) into $\dot{L}_1(t) = V_2(t) - V_1(t)$, we obtain

$$V_{2,0} - V_{1,0} = 0, \quad (4.20)$$

$$V_{2,1} - V_{1,1} = -i\pi d_1 \Omega, \quad (4.21)$$

$$V_{2,-1} - V_{1,-1} = i\pi d_1 \Omega, \quad (4.22)$$

$$V_{2,n} - V_{1,n} = 0 \quad \text{for } |n| \geq 2. \quad (4.23)$$

Similarly, we obtain from $\dot{L}_2(t) = V_3(t) - V_2(t)$

$$V_{3,0} - V_{2,0} = 0, \quad (4.24)$$

$$V_{3,1} - V_{2,1} = \pi d_2 \Phi_2 \Omega, \quad (4.25)$$

$$V_{3,-1} - V_{2,-1} = \pi d_2 \Phi_1 \Omega, \quad (4.26)$$

$$V_{3,n} - V_{2,n} = 0 \quad \text{for } |n| \geq 2, \quad (4.27)$$

where we have introduced the following notations:

$$\Phi_1 = i \cos \phi + \sin \phi, \quad (4.28)$$

$$\Phi_2 = -i \cos \phi + \sin \phi. \quad (4.29)$$

Substituting Eqs. (4.18) and (4.19) into Eqs. (4.15), (4.16) and (4.17), we obtain

$$\begin{aligned} V_{1,n} &\approx \mu[a, -n\Omega] F_{1,n} + M[\ell, -n\Omega] F_{2,n} + \partial M[\ell, -n\Omega] \frac{d_1}{2} (F_{2,n+1} + F_{2,n-1}) \\ &\quad + M[2\ell, -n\Omega] F_{3,n} + \partial M[2\ell, -n\Omega] \frac{d_1}{2} (F_{3,n+1} + F_{3,n-1}) \\ &\quad + \partial M[2\ell, -n\Omega] \frac{id_2}{2} (-\Phi_1 F_{3,n+1} + \Phi_2 F_{3,n-1}), \end{aligned} \quad (4.30)$$

$$\begin{aligned} V_{2,n} &\approx M[\ell, -n\Omega] F_{1,n} + \partial M[\ell, -n\Omega] \frac{d_1}{2} (F_{1,n+1} + F_{1,n-1}) + \mu[a, -n\Omega] F_{2,n} \\ &\quad + M[\ell, -n\Omega] F_{3,n} + \partial M[\ell, -n\Omega] \frac{id_2}{2} (-\Phi_1 F_{3,n+1} + \Phi_2 F_{3,n-1}), \end{aligned} \quad (4.31)$$

$$V_{3,n} \approx M[2\ell, -n\Omega] F_{1,n} + \partial M[2\ell, -n\Omega] \frac{d_1}{2} (F_{1,n+1} + F_{1,n-1})$$

$$\begin{aligned}
& + \partial M[2\ell, -n\Omega] \frac{id_2}{2} (-\Phi_1 F_{1,n+1} + \Phi_2 F_{1,n-1}) \\
& + M[\ell, -n\Omega] F_{2,n} + \partial M[\ell, -n\Omega] \frac{id_2}{2} (-\Phi_1 F_{2,n+1} + \Phi_2 F_{2,n-1}) + \mu[a, -n\Omega] F_{3,n}.
\end{aligned} \tag{4.32}$$

Note that the couplings between different n -modes are involved in these equations. Finally, substituting Eq. (4.19) into $F_1(t) + F_2(t) + F_3(t) = 0$, we obtain

$$F_{1,n} + F_{2,n} + F_{3,n} = 0. \tag{4.33}$$

The above set of equations constitute a matrix equation with infinite dimensions and cannot be solved in general. Under the assumption of $a \ll \ell$, however, we are allowed to consider only $n = -1, 0, 1$ and further approximate as $F_{i,\pm 2} \approx 0$. The justification of the latter approximation is also seen by solving Eqs. (4.23), (4.27), (4.30), (4.31), (4.32) and (4.33) for $n = \pm 2$ and taking the limit of $a \ll \ell$. Hence the above set of equations can be solved for 18 unknowns, i.e., $V_{i,n}$ and $F_{i,n}$ for $i = 1, 2, 3$ and $n = -1, 0, 1$.

The velocity of each sphere is simply obtained by the inverse Fourier transform, $V_i(t) = (2\pi)^{-1} \int_{-\infty}^{\infty} d\omega V_i(\omega) e^{i\omega t}$. The average swimming velocity over one cycle of motion is then calculated by

$$\bar{V} = \frac{\Omega}{2\pi} \int_0^{2\pi/\Omega} dt [V_1(t) + V_2(t) + V_3(t)]/3. \tag{4.34}$$

Within the lowest order expansion in a , we finally obtain Eq. (4.3) by using Eq. (4.1). In order to obtain more accurate higher order terms in a , one needs to take into account the higher order n -modes ($|n| \geq 2$).

4.B Mobilities in a two-fluid polymer gel

Self mobility

The self-mobility μ for a sphere in a two-fluid gel was calculated by Diamant [4.18]. Among various boundary conditions, we consider here “a sticking fluid and a free network” case. In this situation, the full expression of the self-

mobility μ is given by [4.18]

$$\mu[a, \omega] = \frac{1}{6\pi\eta_b a} \frac{N_1 + N_2}{D_1 + D_2}, \quad (4.35)$$

with

$$N_1 = \hat{a}^2 \epsilon \hat{s}^{-1/2} (\hat{a} + \epsilon \hat{s}^{-1/2}) [\hat{a}(1 + \hat{s})^{-1/2} + 3\hat{s}^{-1}], \quad (4.36)$$

$$N_2 = 2\hat{s}^{-1} (\hat{a} + 3\epsilon \hat{s}^{-1/2}) (2\hat{a} + 3\epsilon \hat{s}^{-1/2}) [\hat{a}(1 + \hat{s})^{-1/2} + \hat{s}^{-1}], \quad (4.37)$$

$$D_1 = \hat{a}^2 \epsilon \hat{s}^{-1/2} (\hat{a} + \epsilon \hat{s}^{-1/2}) [\hat{a}(1 + \hat{s})^{-1/2} + (1 + \hat{s})^{-1} + 2\hat{s}^{-1}], \quad (4.38)$$

$$D_2 = 2\hat{s}^{-1} (1 + \hat{s})^{-1/2} (\hat{a} + 3\epsilon \hat{s}^{-1/2}) (2\hat{a} + 3\epsilon \hat{s}^{-1/2}) [\hat{a} + (1 + \hat{s})^{-1/2}], \quad (4.39)$$

where we have used the dimensionless notations $\hat{a} = a/\xi$, $\hat{s} = i\omega\tau$ and $\epsilon = [(K + 4G/3)/G]^{1/2}$.

In addition to Eqs. (4.7) and (4.8), the above self-mobility has other limiting expressions. In the limit of $a/\xi \rightarrow 0$, the self-mobility becomes

$$\mu[a, \omega] \approx \frac{1}{6\pi\eta a} - \frac{1}{6\pi\eta\xi} \frac{1}{(1 + i\omega\tau)^{1/2}}, \quad (4.40)$$

which corrects the Stokes mobility. In the limit of $a/\xi \rightarrow \infty$, on the other hand, we have

$$\mu[a, \omega] \approx \frac{1}{6\pi\eta_b a} + \frac{\xi}{6\pi\eta a^2} \frac{1}{(1 + i\omega\tau)^{1/2} (1 + i\omega\tau)}. \quad (4.41)$$

In this regime, the response of a sphere is governed by η_b .

Approximate expressions of the self-mobility

When $a \gg \xi$ and $\omega\tau \ll 1$, Eq. (4.35) can be approximated as

$$\mu[a, s] \approx \frac{1}{6\pi\eta a} \frac{18\epsilon^2 + 18\hat{a}\epsilon\hat{s}^{1/2} + \hat{a}^2(3\epsilon^2 + 4)\hat{s} + 3\hat{a}^3\epsilon\hat{s}^{3/2} + \hat{a}^4\epsilon\hat{s}^{5/2}}{2\hat{a}^2\epsilon^2 + 2\hat{a}^3\epsilon\hat{s}^{1/2} + \hat{a}^4\epsilon\hat{s}^{3/2}}. \quad (4.42)$$

Using the notations $X = \hat{a}\hat{s}^{1/2}$ and $Y = \hat{a}\hat{s}$, the above expression can be rewritten as

$$\mu[a, s] \approx \frac{1}{6\pi\eta a} \frac{18\epsilon^2 + 18\epsilon X + (3\epsilon^2 + 4)X^2 + 3\epsilon X^3 + \epsilon X^3 Y}{2\hat{a}^2\epsilon^2 + 2\epsilon\hat{a}^2 X + \epsilon\hat{a}^2 XY}, \quad (4.43)$$

where $X \gg Y$ holds because $\hat{s} \ll 1$.

For $X \ll 1$ and $Y \ll 1$, we have

$$\mu[a, s] \approx \frac{1}{6\pi\eta a} \frac{9}{\hat{a}^2}. \quad (4.44)$$

For $X \gg 1$ and $Y \ll 1$, we have

$$\mu[a, s] \approx \frac{1}{6\pi\eta a} \left(\frac{2\hat{a}^2}{3X^2} + \frac{\hat{a}^2 Y}{9X^2} - \frac{8\hat{a}^2}{9\epsilon X^3} \right)^{-1}. \quad (4.45)$$

For $Y \gg 1$ and $X \gg 1$, we have

$$\mu[a, s] \approx \frac{1}{6\pi\eta a} \left(\frac{\hat{a}^2}{X^2} - \frac{\hat{a}^2}{X^2 Y} \right)^{-1}. \quad (4.46)$$

Coupling mobility

The full expression of the longitudinal coupling mobility is given by [4.22, 4.23]

$$M[r, \omega] = \frac{1}{4\pi\eta r} \left[1 + \frac{1 - \eta_b/\eta}{\eta_b/\eta} \mathcal{G}(\hat{r}) \right], \quad (4.47)$$

where $\hat{r} = r(1 + i\omega\tau)^{1/2}/\xi$ and the scaling function $\mathcal{G}(z)$ is given by

$$\mathcal{G}(z) = 1 - \frac{2}{z^2} + \frac{2e^{-z}}{z} \left(1 + \frac{1}{z} \right). \quad (4.48)$$

4.C Asymptotic expressions of the average velocity

Large swimmer

For $\Omega\tau \ll (a/\xi)^{-2}$, we use the first term of Eq. (4.7) and the second term of Eq. (4.10) to obtain

$$\bar{V}_v \approx \frac{31d_1d_2a^3\Omega}{144\ell^4} \sin\phi, \quad (4.49)$$

as in Eq. (4.11).

For $(a/\xi)^{-2} \ll \Omega\tau \ll (a/\xi)^{-4/3}$, we use the third term of Eq. (4.45) and the second term of Eq. (4.10) to obtain

$$\bar{V}_v \approx \frac{31d_1d_2\xi^3}{18\sqrt{2}\epsilon\ell^4\Omega^{1/2}\tau^{3/2}} \sin\phi. \quad (4.50)$$

For $(a/\xi)^{-4/3} \ll \Omega\tau \ll (a/\xi)^{-1}$, we use the second term of Eq. (4.45) and

the second term of Eq. (4.10) to obtain

$$\bar{V}_v \approx \frac{31d_1d_2\xi a^2\Omega}{144\ell^4} \sin\phi. \quad (4.51)$$

For $(a/\xi)^{-1} \ll \Omega\tau \ll (a/\xi)^{-1/2}$, we use Eq. (4.46) and the second term of Eq. (4.10) to obtain

$$\bar{V}_v \approx \frac{31d_1d_2\xi^3}{16\ell^4\Omega\tau^2} \sin\phi. \quad (4.52)$$

For $\Omega\tau \gg (a/\xi)^{-1/2}$, we use the first term of Eq. (4.8) and the second term of Eq. (4.10) to obtain

$$\bar{V}_v \approx \frac{31d_1d_2\xi^2 a\Omega}{16\ell^4} \sin\phi, \quad (4.53)$$

as in Eq. (4.12).

Medium swimmer

For $\Omega\tau \ll 1$, we use the second term of Eq. (4.7) and the second term of Eq. (4.10) to obtain

$$\bar{V}_e \approx \frac{17(d_1^2 - d_2^2)\xi a^2}{64\ell^4\tau} (\Omega\tau)^2. \quad (4.54)$$

For $1 \ll \Omega\tau \ll (a/\xi)^{-2}$, we use the second term of Eq. (4.40) and the second term of Eq. (4.10) to obtain

$$\bar{V}_e \approx \frac{17\sqrt{2}(d_1^2 - d_2^2)\xi a^2}{64\ell^4\tau} (\Omega\tau)^{1/2}. \quad (4.55)$$

Small swimmer

For $(\ell/\xi)^{-2} \ll \Omega\tau \ll (a/\xi)^{-2}$, we use the second term of Eq. (4.40) and the first term of Eq. (4.9) to obtain

$$\bar{V}_e \approx \frac{5\sqrt{2}(d_1^2 - d_2^2)a^2}{96\ell^2\xi\tau} (\Omega\tau)^{1/2}. \quad (4.56)$$

For $\Omega\tau \gg (a/\xi)^{-2}$, we use the second term of Eq. (4.8) and the first term of Eq. (4.9) to obtain

$$\bar{V}_e \approx \frac{5(d_1^2 - d_2^2)a}{48\ell^2\tau}. \quad (4.57)$$

References

- [4.1] E. Lauga and T. R. Powers, *Rep. Prog. Phys.* **72**, 096601 (2009).
- [4.2] E. M. Purcell, *Am. J. Phys.* **45**, 3 (1977).
- [4.3] A. Najafi and R. Golestanian, *Phys. Rev. E* **69**, 062901 (2004).
- [4.4] R. Golestanian and A. Ajdari, *Phys. Rev. E* **77**, 036308 (2008).
- [4.5] G. Grosjean, M. Hubert, G. Lagubeau, and N. Vandewalle, *Phys. Rev. E* **94**, 021101(R) (2016).
- [4.6] G. Grosjean, M. Hubert, and N. Vandewalle, *Adv. Colloid Interface Sci.* **255**, 84 (2018).
- [4.7] E. Lauga, *EPL* **86**, 64001 (2009).
- [4.8] J. Teran, L. Fauci, and M. Shelley, *Phys. Rev. Lett.* **104**, 038101 (2010).
- [4.9] M. P. Curtis and E. A. Gaffney, *Phys. Rev. E* **87**, 043006 (2013).
- [4.10] T. Qiu, T.-C. Lee, A. G. Mark, K. I. Morozov, R. Munster, O. Mierka, S. Turek, A. M. Leshansky, and P. Fischer, *Nat. Commun.* **5**, 5119 (2014).
- [4.11] K. Ishimoto and E. A. Gaffney, *J. Fluid Mech.* **831**, 228 (2017).
- [4.12] K. Yasuda, R. Okamoto, and S. Komura, *J. Phys. Soc. Jpn.* **86**, 043801 (2017).
- [4.13] T. A. Witten and P. Pincus, *Structured Fluids* (Oxford University Press, Oxford, 2004).
- [4.14] R. G. Larson, *The Structure and Rheology of Complex Fluids* (Oxford University Press, Oxford, 1999).
- [4.15] P. G. de Gennes, *Macromolecules* **9**, 587 (1976).
- [4.16] P. G. de Gennes, *Macromolecules* **9**, 594 (1976).

-
- [4.17] F. Brochard and P. G. de Gennes, *Macromolecules* **10**, 1157 (1977).
- [4.18] H. Diamant, *Eur. Phys. J. E* **38**, 32 (2015).
- [4.19] A. Sonn-Segev, A. Bernheim-Groswasser, H. Diamant, and Y. Roichman, *Phys. Rev. Lett.* **122**, 088301 (2014).
- [4.20] A. Sonn-Segev, A. Bernheim-Groswasser, and Y. Roichman, *Soft Matter* **10**, 8324 (2014).
- [4.21] A. C. Pipkin, *Lectures on Viscoelasticity Theory* (Springer-Verlag, New York, 1972).
- [4.22] K. Yasuda, R. Okamoto, S. Komura, and A. S. Mikhailov, *EPL* **117**, 38001 (2017).
- [4.23] K. Yasuda, R. Okamoto, and S. Komura, *Phys. Rev. E* **95**, 032417 (2017).
- [4.24] M. Doi and A. Onuki, *J. Phys. II (France)* **2**, 1631 (1992).
- [4.25] R. Bruinsma, A. Y. Grosberg, Y. Rabin, and A. Zidovska, *Biophys. J.* **106**, 1871 (2014).
- [4.26] M. S. Krieger, S. E. Spagnolieb, and T. Powers *Soft Matter* **11**, 9115 (2015).
- [4.27] S. Fujii, S. Komura, and C.-Y. D. Lu, *Materials* **7**, 5146 (2014).
- [4.28] Y. Ota, Y. Hosaka, K. Yasuda, and S. Komura, *Phys. Rev. E* **97**, 052612 (2018).
- [4.29] E. M. Furst and T. M. Squires, *Microrheology* (Oxford University Press, Oxford, 2017).
- [4.30] H. C. Fu, V. B. Shenoy, and T. R. Powers, *EPL* **91**, 24002 (2010).

Chapter 5

Elastic Three-Sphere

Microswimmer in a Viscous Fluid

We discuss the dynamics of a generalized three-sphere microswimmer in which the spheres are connected by two elastic springs. The natural length of each spring is assumed to undergo a prescribed cyclic change. We analytically obtain the average swimming velocity as a function of the frequency of cyclic change in the natural length. In the low-frequency region, the swimming velocity increases with frequency, and its expression reduces to that of the original three-sphere model by Najafi and Golestanian. Conversely, in the high-frequency region, the average velocity decreases with increasing frequency. Such behavior originates from the intrinsic spring relaxation dynamics of an elastic swimmer moving in a viscous fluid.

5.1 Introduction

Microswimmers are tiny machines that swim in a fluid, such as sperm cells or motile bacteria, and they are expected to be applied to microfluidics and microsystems [5.1]. By transforming chemical energy into mechanical work,

microswimmers change their shape and move in viscous environments. Over the length scale of microswimmers, the fluid forces acting on them are governed by the effect of viscous dissipation. According to Purcell's scallop theorem [5.2], time-reversal body motion cannot be used for locomotion in a Newtonian fluid [5.3]. As one of the simplest models exhibiting broken time-reversal symmetry, Najafi and Golestanian proposed a three-sphere swimmer [5.4, 5.5], in which three in-line spheres are linked by two arms of varying length. Recently, such a swimmer has been experimentally realized by using ferromagnetic particles at an air-water interface and by applying an oscillating magnetic field [5.6].

The original Najafi–Golestanian model has been further extended to various situations, such as the case when one of the spheres has a larger radius [5.7] or when three spheres are arranged in a triangular configuration [5.8]. Montino and DeSimone considered the case in which one arm is periodically actuated while the other is replaced by a passive elastic spring [5.9]. It was shown that such a swimmer exhibits a delayed mechanical response of the passive spring with respect to the active arm. More recently, they analyzed the motion of a three-sphere swimmer with arms having active viscoelastic properties mimicking muscular contraction [5.10]. Recently, Nasouri *et al.* discussed the motion of an elastic two-sphere swimmer, in which one of the sphere is a neo-Hookean solid [5.11].

Another approach for extending the Najafi–Golestanian model is to consider the arm motions as occurring stochastically [5.12, 5.13], rather than assuming a prescribed sequence of deformations [5.4, 5.5]. In these models, the configuration space of a swimmer generally consists of a finite number of distinct states. A similar idea was employed by Sakaue *et al.*, who discussed the propulsion of molecular machines or active proteins in the presence of hydrodynamic interactions [5.14]. Later, Huang *et al.* considered a modified three-sphere swimmer in a two-dimensional viscous fluid [5.15]. In their model, the spheres are connected by two springs, the lengths of which are assumed to depend on the discrete states

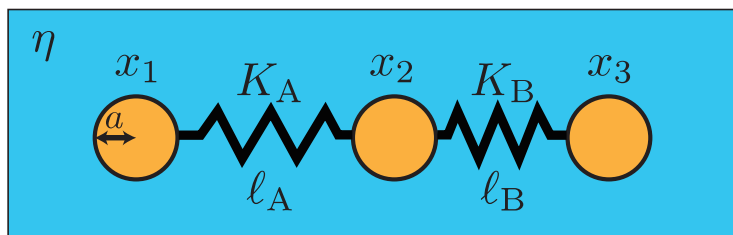


Figure 5.1: Elastic three-sphere microswimmer in a viscous fluid characterized by the shear viscosity η . Three identical spheres of radius a are connected by two harmonic springs with elastic constants K_A and K_B . The natural lengths of the springs, $\ell_A(t)$ and $\ell_B(t)$, depend on time and are assumed to undergo cyclic change [see Eqs. (5.6) and (5.7)]. The time-dependent positions of the spheres are denoted by $x_1(t)$, $x_2(t)$, and $x_3(t)$ in a one-dimensional coordinate system.

that are cyclically switched. As a result, the dynamics of a swimmer consists of the spring relaxation processes, which follow after each switching event.

In this chapter, we discuss a generalized three-sphere swimmer in which the spheres are simply connected by two harmonic springs. The main difference between this model and the previous models is that the natural length of each spring depends on time and is assumed to undergo a prescribed cyclic change. Whereas the arms in the Najafi–Golestanian model undergo a prescribed motion regardless of the force exerted by the fluid, the sphere motion in our model is determined by the natural spring lengths representing internal states of a swimmer and also by the force exerted by the fluid. In this sense, our model is more realistic to study the locomotion of active microswimmers. We analytically obtain the average swimming velocity as a function of the frequency of cyclic change in the natural length. In order to better illustrate our result, we first explain the case in which the two spring constants are identical and the two oscillation amplitudes of the natural lengths are the same. Then, we shall discuss a general case in which these quantities are different and the phase mismatch between the natural lengths is arbitrary.

The introduction of harmonic springs between the spheres leads to an intrinsic time scale of an elastic swimmer that characterizes its internal relaxation

dynamics. When the frequency of cyclic change in the natural lengths is smaller than this characteristic time, the swimming velocity increases with frequency, as in the previous works [5.5]. In the high-frequency region, on the other hand, the motion of spheres cannot follow the change in the natural length, and the average swimming velocity decreases with increasing frequency. Such a situation resembles the dynamics of the Najafi–Golestanian three-sphere swimmer in a viscoelastic medium [5.16]. We also show that, owing to the elasticity that has been introduced, the proposed micromachine can swim even if the change in the natural lengths is reciprocal as long as its structural symmetry is violated. Although the considered swimmer appears to be somewhat trivial, it can be regarded as a generic model for microswimmers or protein machines since the behaviors of the previous models can be deduced from our model by taking different limits.

5.2 Model

We generalize the Najafi–Golestanian three-sphere swimmer model to take into account the elasticity in the sphere motion. As schematically shown in Fig. 5.1, the present model consists of three hard spheres of the same radius a connected by two harmonic springs A and B with spring constants K_A and K_B , respectively. We assume that the natural lengths of these springs, denoted by $\ell_A(t)$ and $\ell_B(t)$, undergo cyclic time-dependent change. Their explicit time dependences will be specified later. The total energy of an elastic swimmer is then given by

$$E = \frac{K_A}{2}(x_2 - x_1 - \ell_A)^2 + \frac{K_B}{2}(x_3 - x_2 - \ell_B)^2, \quad (5.1)$$

where $x_i(t)$ ($i = 1, 2, 3$) are the positions of the three spheres in a one-dimensional coordinate system. We also assume $x_1 < x_2 < x_3$ without loss of generality. Owing to the hydrodynamic interaction, each sphere exerts a force on the viscous fluid of shear viscosity η and experiences an opposite force from it. In general, the surrounding medium can be viscoelastic [5.16], but such an effect is not

considered in this chapter.

Denoting the velocity of each sphere by \dot{x}_i , we can write the equations of motion of the three spheres as

$$\begin{aligned} \dot{x}_1 = & \frac{K_A}{6\pi\eta a}(x_2 - x_1 - \ell_A) - \frac{K_A}{4\pi\eta} \frac{(x_2 - x_1 - \ell_A)}{x_2 - x_1} \\ & + \frac{K_B}{4\pi\eta} \frac{(x_3 - x_2 - \ell_B)}{x_2 - x_1} - \frac{K_B}{4\pi\eta} \frac{(x_3 - x_2 - \ell_B)}{x_3 - x_1}, \end{aligned} \quad (5.2)$$

$$\begin{aligned} \dot{x}_2 = & \frac{K_A}{4\pi\eta} \frac{(x_2 - x_1 - \ell_A)}{x_2 - x_1} - \frac{K_A}{6\pi\eta a}(x_2 - x_1 - \ell_A) \\ & + \frac{K_B}{6\pi\eta a}(x_3 - x_2 - \ell_B) - \frac{K_B}{4\pi\eta} \frac{(x_3 - x_2 - \ell_B)}{x_3 - x_2}, \end{aligned} \quad (5.3)$$

$$\begin{aligned} \dot{x}_3 = & \frac{K_A}{4\pi\eta} \frac{(x_2 - x_1 - \ell_A)}{x_3 - x_1} - \frac{K_A}{4\pi\eta} \frac{(x_2 - x_1 - \ell_A)}{x_3 - x_2} \\ & + \frac{K_B}{4\pi\eta} \frac{(x_3 - x_2 - \ell_B)}{x_3 - x_2} - \frac{K_B}{6\pi\eta a}(x_3 - x_2 - \ell_B), \end{aligned} \quad (5.4)$$

where we have used the Stokes' law for a sphere and the Oseen tensor in a three-dimensional viscous fluid. The swimming velocity of the whole object can be obtained by averaging the velocities of the three spheres:

$$V = \frac{1}{3}(\dot{x}_1 + \dot{x}_2 + \dot{x}_3). \quad (5.5)$$

One of the advantages of the present formulation is that the motion of the spheres is simply described by coupled ordinary differential equations. Moreover, the force-free condition for the whole system [5.4, 5.5] is automatically satisfied in the above equations.

Next, we assume that the two natural lengths of the springs undergo the following periodic changes:

$$\ell_A(t) = \ell + d_A \cos(\Omega t), \quad (5.6)$$

$$\ell_B(t) = \ell + d_B \cos(\Omega t - \phi). \quad (5.7)$$

In the above, ℓ is the common constant length, d_A and d_B are the amplitudes of the oscillatory change, Ω is the common frequency, and ϕ is the mismatch in phase between the two cyclic changes. The time-reversal symmetry of the spring dynamics exists only when $\phi = 0$ or π ; otherwise, the time-reversal symmetry

is broken. In the following analysis, we generally assume that $d_A, d_B, a \ll \ell$ and focus on the leading-order contribution. It is convenient to introduce a characteristic time scale $\tau = 6\pi\eta a/K_A$. Then we use ℓ to scale all the relevant lengths (x_i , a , d_A , and d_B) and employ τ to scale the frequency, i.e., $\hat{\Omega} = \Omega\tau$. By further defining the ratio between the two spring constants as $\lambda = K_B/K_A$, the coupled Eqs. (5.2)–(5.4) can be made dimensionless.

5.3 Results

In order to discuss the essential outcome of the present model, we shall first consider the simplest symmetric case, i.e., $\lambda = 1$, $d_A = d_B = d$, and $\phi = \pi/2$. Hence, Eq. (5.7) now reads $\ell_B(t) = \ell + d \sin(\Omega t)$. For our later calculation, it is useful to introduce the following spring lengths with respect to ℓ :

$$u_A = x_2 - x_1 - \ell, \quad u_B = x_3 - x_2 - \ell. \quad (5.8)$$

Notice that these quantities are related to the sphere velocities in Eqs. (5.2)–(5.4) as

$$\dot{u}_A = \dot{x}_2 - \dot{x}_1, \quad \dot{u}_B = \dot{x}_3 - \dot{x}_2. \quad (5.9)$$

Using Eqs. (5.2)–(5.4) and solving Eq. (5.9) in the frequency domain, we obtain the following expressions after inverse Fourier transform

$$u_A(t) \approx \frac{9 - 3\hat{\Omega} + 5\hat{\Omega}^2 + \hat{\Omega}^3}{9 + 10\hat{\Omega}^2 + \hat{\Omega}^4} d \cos(\Omega t) + \frac{6\hat{\Omega} - 4\hat{\Omega}^2 + 2\hat{\Omega}^3}{9 + 10\hat{\Omega}^2 + \hat{\Omega}^4} d \sin(\Omega t), \quad (5.10)$$

$$u_B(t) \approx -\frac{6\hat{\Omega} + 4\hat{\Omega}^2 + 2\hat{\Omega}^3}{9 + 10\hat{\Omega}^2 + \hat{\Omega}^4} d \cos(\Omega t) + \frac{9 + 3\hat{\Omega} + 5\hat{\Omega}^2 - \hat{\Omega}^3}{9 + 10\hat{\Omega}^2 + \hat{\Omega}^4} d \sin(\Omega t), \quad (5.11)$$

where we have used $a/\ell \ll 1$.

According to the calculation by Golestanian and Ajdari [5.5], the average swimming velocity of a three-sphere swimmer can generally be expressed up to the leading order in u_A/ℓ and u_B/ℓ as

$$\bar{V} = \frac{7a}{24\ell^2} \langle u_A \dot{u}_B - \dot{u}_A u_B \rangle, \quad (5.12)$$

where the averaging $\langle \dots \rangle$ is performed by time integration in a full cycle. The

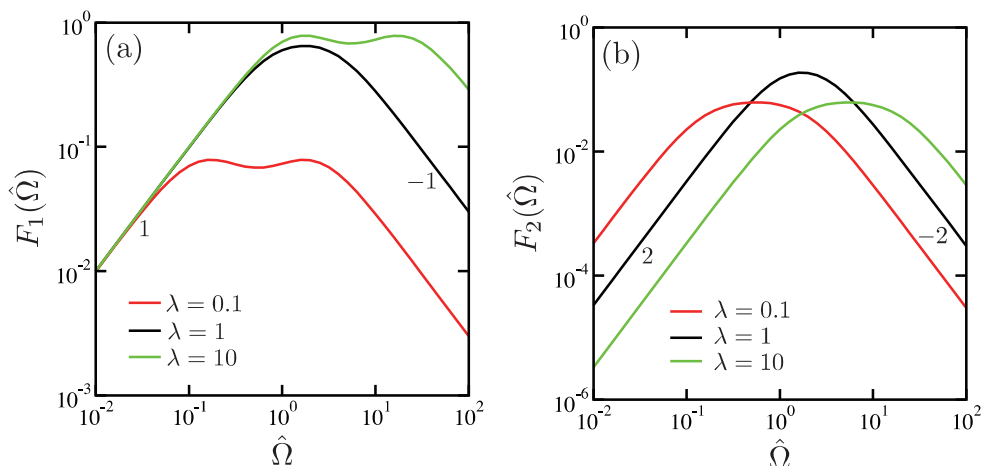


Figure 5.2: Plots of the scaling functions (a) $F_1(\hat{\Omega}; \lambda)$ and (b) $F_2(\hat{\Omega}; \lambda)$ defined in Eqs. (5.22) and (5.23), respectively, as functions of $\hat{\Omega} = \Omega\tau$ for $\lambda = K_B/K_A = 0.1, 1$, and 10 . The numbers indicate the slope representing the exponent of the power-law behaviors.

above expression indicates that the average velocity is determined by the area enclosed by the orbit of periodic motion in the configuration space [5.5]. Using Eqs. (5.10) and (5.11) for an elastic microswimmer with $d/\ell, a/\ell \ll 1$, we obtain the lowest-order contribution as

$$\bar{V} = \frac{7d^2a}{24\ell^2\tau} \frac{3\hat{\Omega}(3 + \hat{\Omega}^2)}{9 + 10\hat{\Omega}^2 + \hat{\Omega}^4}, \quad (5.13)$$

which is an important result of this chapter.

We first consider the small-frequency limit of $\hat{\Omega} \ll 1$. Physically, this limit corresponds to the case when the spring constant K_A is very large. We easily obtain

$$u_A(t) \approx d \cos(\Omega t), \quad u_B(t) \approx d \sin(\Omega t), \quad (5.14)$$

and

$$\bar{V} \approx \frac{7d^2a\Omega}{24\ell^2}, \quad (5.15)$$

which exactly coincides with the average velocity of the Najafi-Golestani swimmer with identical spheres [5.4, 5.5]. This is reasonable because the two spring lengths u_A and u_B are in phase with their respective natural lengths ℓ_A

and ℓ_B , as we can see from Eqs. (5.6), (5.7), and (5.14). Notice that the average velocity increases as $\bar{V} \sim \Omega$ in this limit, while it does not depend on the fluid viscosity η [5.4, 5.5].

In the opposite large-frequency limit of $\hat{\Omega} \gg 1$, on the other hand, we have

$$u_A(t) \approx \frac{\sqrt{5}d}{\Omega\tau} \cos[\Omega t - \arctan 2], \quad (5.16)$$

$$u_B(t) \approx \frac{\sqrt{5}d}{\Omega\tau} \sin[\Omega t - (\pi - \arctan 2)], \quad (5.17)$$

where $\arctan 2 \approx 1.107$ and

$$\bar{V} \approx \frac{21d^2a}{24\ell^2\Omega\tau^2}. \quad (5.18)$$

We see here that u_A and u_B are out of phase with respect to the natural lengths ℓ_A and ℓ_B , while the average velocity decreases as $\bar{V} \sim \Omega^{-1}$ when Ω is increased. When the spring constant K_A is small, it takes time for a spring to relax to its natural length, which leads to a delay in the mechanical response. The crossover frequency between the above two regimes is determined by $\hat{\Omega}^* \sim 1$. The general frequency dependence of Eq. (5.13) is shown in Fig. 5.2(a) for $\lambda = 1$ (black line). It shows a maximum around $\hat{\Omega} \sim 1$, as expected.

Recently, we investigated the motion of the Najafi-Golestanian three-sphere swimmer in a viscoelastic medium [5.16]. We derived a relation that connects the average swimming velocity and the frequency-dependent viscosity of the surrounding medium. In this relation, the viscous contribution can exist only when the time-reversal symmetry is broken, whereas the elastic contribution is present only when the structural symmetry of the swimmer is broken. In particular, we calculated the average swimming velocity when the surrounding viscoelastic medium is described by a simple Maxwell fluid with a characteristic time scale τ_M . It was shown that the viscous term increases as $\bar{V} \sim \Omega$ for $\Omega\tau_M \ll 1$, while it decreases as $\bar{V} \sim \Omega^{-1}$ for $\Omega\tau_M \gg 1$. This is a unique feature of a swimmer in a viscoelastic medium [5.16–5.18], and such a reduction occurs simply because the medium responds elastically in the high-frequency regime. We note that the

frequency dependence of \bar{V} for an elastic three-sphere swimmer, as obtained in Eqs. (5.13), is analogous to that for the Najafi-Golestanian swimmer in a viscoelastic Maxwell fluid. In other words, an elastic microswimmer in a viscous fluid exhibits “viscoelastic” effects as a whole.

Having discussed the simplest situation of the proposed elastic swimmer, we now show the result for a general case when $K_A \neq K_B$ (or $\lambda \neq 1$), $d_A \neq d_B$, and the phase mismatch ϕ in Eq. (5.7) is arbitrary. By repeating the same calculation as before, the spring lengths in Eq. (5.8) now become

$$u_A(t) \approx \frac{1}{9\lambda^2 + 2(2 + \lambda + 2\lambda^2)\hat{\Omega}^2 + \hat{\Omega}^4} \times \left\{ [9\lambda^2 + (4 + \lambda)\hat{\Omega}^2]d_A \cos(\Omega t) + 2(3\lambda^2 + \hat{\Omega}^2)\hat{\Omega}d_A \sin(\Omega t) - 2\lambda(1 + \lambda)\hat{\Omega}^2d_B \cos(\Omega t - \phi) - \lambda(-3\lambda + \hat{\Omega}^2)\hat{\Omega}d_B \sin(\Omega t - \phi) \right\}, \quad (5.19)$$

$$u_B(t) \approx \frac{1}{9\lambda^2 + 2(2 + \lambda + 2\lambda^2)\hat{\Omega}^2 + \hat{\Omega}^4} \times \left\{ -2(1 + \lambda)\hat{\Omega}^2d_A \cos(\Omega t) + (3\lambda - \hat{\Omega}^2)\hat{\Omega}d_A \sin(\Omega t) + \lambda[9\lambda + (1 + 4\lambda)\hat{\Omega}^2]d_B \cos(\Omega t - \phi) + 2\lambda(3 + \hat{\Omega}^2)\hat{\Omega}d_B \sin(\Omega t - \phi) \right\}, \quad (5.20)$$

respectively, where we have used $a/\ell \ll 1$. Using Eq. (5.12) again, we finally obtain the lowest-order general expression of the average velocity as

$$\bar{V} = \frac{7d_A d_B a}{24\ell^2 \tau} F_1(\hat{\Omega}; \lambda) \sin \phi - \frac{7(\lambda - 1)d_A d_B a}{12\ell^2 \tau} F_2(\hat{\Omega}; \lambda) \cos \phi + \frac{7(d_A^2 - d_B^2 \lambda)a}{24\ell^2 \tau} F_2(\hat{\Omega}; \lambda), \quad (5.21)$$

where the two scaling functions are defined by

$$F_1(\hat{\Omega}; \lambda) = \frac{3\lambda\hat{\Omega}(3\lambda + \hat{\Omega}^2)}{9\lambda^2 + 2(2 + \lambda + 2\lambda^2)\hat{\Omega}^2 + \hat{\Omega}^4}, \quad (5.22)$$

$$F_2(\hat{\Omega}; \lambda) = \frac{3\lambda\hat{\Omega}^2}{9\lambda^2 + 2(2 + \lambda + 2\lambda^2)\hat{\Omega}^2 + \hat{\Omega}^4}. \quad (5.23)$$

In Fig. 5.2, we plot the above scaling functions as functions of $\hat{\Omega}$ for $\lambda = 0.1$ and 10. Notice, however, that these two cases are essentially equivalent because we

can always exchange the springs A and B, whereas we have defined the relaxation time τ by using K_A .

When $\lambda = 1$, $d_A = d_B$, and $\phi = \pi/2$, only the first term remains, and Eq. (5.21) reduces to Eq. (5.13), as expected. When $\lambda \neq 1$, on the other hand, the second term is present even if $\phi = 0$. The third term is also present when $d_A^2 \neq d_B^2 \lambda$, regardless of the phase mismatch ϕ . Notice that the first term represents the broken time-reversal symmetry for $\phi \neq 0$, whereas both the second and third terms reflect the structural asymmetry of an elastic three-sphere swimmer [5.16]. To be more precise, the second term is due to the difference between the relaxation times of the two springs, and the third term reflects the asymmetric changes of their natural lengths.

It is interesting to note that the frequency dependence of the second and third terms in Eq. (5.21), represented by $F_2(\hat{\Omega}, \lambda)$, is different from that of the first term, represented by $F_1(\hat{\Omega}, \lambda)$. According to Eq. (5.23), \bar{V} due to the second and third terms increases as $\bar{V} \sim \Omega^2$ for $\hat{\Omega} \ll 1$, whereas it decreases as $\bar{V} \sim \Omega^{-2}$ for $\hat{\Omega} \gg 1$. In general, the overall swimming velocity depends on various structural parameters and exhibits a complex frequency dependence. For example, $F_1(\hat{\Omega}, \lambda)$ in Fig. 5.2(a) exhibits a non-monotonic frequency dependence (two maxima) for $\lambda = 0.1$ or 10 (namely, when $\lambda \neq 1$). On the other hand, an important common feature in all the terms in Eq. (5.21) is that \bar{V} decreases for $\hat{\Omega} \geq 1$, which is characteristic of elastic swimmers.

We confirm again that Eq. (5.21) reduces to the result by Golestanian and Ajdari [5.5], i.e., $\bar{V} = 7d_A d_B a \Omega \sin \phi / (24\ell^2)$, when the two spring constants are infinitely large, i.e., $K_A, K_B \rightarrow \infty$ and $\lambda = 1$. The third term in Eq. (5.21) vanishes even if $d_A \neq d_B$ because $\hat{\Omega} \rightarrow 0$ holds in this limit. In the modified three-sphere swimmer model considered by Montino and DeSimone, one of the two arms was replaced by a passive elastic spring [5.9]. Their model can be obtained from the present model simply by setting one of the spring constants to be infinitely large, say $K_A \rightarrow \infty$, and by regarding the natural length of the

other spring as a constant, say $\ell_B = \ell$ (or $d_B = 0$). The continuous changes of the natural lengths introduced in Eqs. (5.6) and (5.7) are a straightforward generalization of cyclically switched discrete states considered in the previous studies [5.12–5.15]. We finally note that a model similar to the present one was considered in Ref. [5.19], although that study focused only on the low-frequency region and did not discuss the entire frequency dependence. Using coupled Langevin equations, the authors of Ref. [5.19] mainly investigated the interplay between self-driven motion and diffusive behavior [5.19], which is also an important aspect of microswimmers.

5.4 Summary and discussion

To summarize, we have discussed the locomotion of a generalized three-sphere microswimmer in which the spheres are connected by two elastic springs and the natural length of each spring is assumed to undergo a prescribed cyclic change. As shown in Eqs. (5.13) and (5.21), we have analytically obtained the average swimming velocity \bar{V} as a function of the frequency Ω of cyclic change in the natural length. In the low-frequency region, the swimming velocity increases with frequency and reduces to the original three-sphere model by Najafi and Golestanian [5.4, 5.5]. Conversely, in the high-frequency region, the velocity decreases with increasing frequency. This property reflects the intrinsic spring relaxation dynamics of an elastic swimmer in a viscous fluid.

References

- [5.1] E. Lauga and T. R. Powers, *Rep. Prog. Phys.* **72** 096601 (2009).
- [5.2] E. M. Purcell, *Am. J. Phys.* **45**, 3 (1977).
- [5.3] E. Lauga, *Soft Matter* **7**, 3060 (2011).
- [5.4] A. Najafi and R. Golestanian, *Phys. Rev. E* **69**, 062901 (2004).
- [5.5] R. Golestanian and A. Ajdari, *Phys. Rev. E* **77**, 036308 (2008).

- [5.6] G. Grosjean, M. Hubert, G. Lagubeau, and N. Vandewalle, *Phys. Rev. E* **94**, 021101(R) (2016).
- [5.7] R. Golestanian, *Eur. Phys. J. E* **25**, 1 (2008).
- [5.8] R. Ledesma-Aguilar, H. Löwen, and J. M. Yeomans, *Eur. Phys. J. E* **35**, 70 (2012).
- [5.9] A. Montino and A. DeSimone, *Eur. Phys. J. E* **42**, 38 (2015).
- [5.10] A. Montino and A. DeSimone, *Acta Appl. Math.* **149**, 53 (2017).
- [5.11] B. Nasouri, A. Khot, and G. J. Elfring, *Phys. Rev. Fluids* **2**, 043101 (2017).
- [5.12] R. Golestanian and A. Ajdari, *Phys. Rev. Lett.* **100**, 038101 (2008).
- [5.13] R. Golestanian, *Phys. Rev. Lett.* **105**, 018103 (2010).
- [5.14] T. Sakaue, R. Kapral, and A. S. Mikhailov, *Eur. Phys. J. B* **75**, 381 (2010).
- [5.15] M.-J. Huang, H.-Y. Chen, and A. S. Mikhailov, *Eur. Phys. J. E* **119**, 35 (2012).
- [5.16] K. Yasuda, R. Okamoto, and S. Komura, *J. Phys. Soc. Jpn.* **86**, 043801 (2017).
- [5.17] E. Lauga, *EPL* **86**, 64001 (2009).
- [5.18] M. P. Curtis and E. A. Gaffney, *Phys. Rev. E* **87**, 043006 (2013).
- [5.19] J. Dunkel and I. M. Zaid, *Phys. Rev. E* **80**, 021903 (2009).
- [5.20] J. Pande and A.-S. Smith, *Soft Matter* **11**, 2364 (2015).
- [5.21] J. Pande, L. Merchant, T. Krüger, J. Harting, and A.-S. Smith, *New J. Phys.* **19**, 053024 (2017).

Chapter 6

State Transition of a Micromachine Driven by Catalytic Reaction

I propose a model that describes cyclic state transitions of a micromachine driven by catalytic chemical reaction. This model is introduced to understand the universal principle of nonequilibrium micromachines. I consider the coupled dynamics of variables representing the degree of chemical reaction and the state of a micromachine. The total free energy of the system consists of the tilted periodic potential and the periodic coupling energy. I assume that the reaction variable obeys a deterministic stepwise dynamics characterized by two typical time scales: the mean first passage time and the mean first transition path time. To estimate the functionality of a micromachine, I introduce a physical quantity called “state cyclone” and further discuss its dependency on the properties of the chemical reaction. For example, I show that the state cyclone is proportional to the square of the mean first transition path time. The explicit calculation of these time scales within the proposed model reveals that the state cyclone is inversely proportional to the square of the activation energy of the chemical reaction.

6.1 Introduction

In recent years, physics of micromachines such as bacteria, motor proteins, artificial molecular machines has been intensively studied [6.1, 6.2]. Generally, a micromachine can be defined as a small object that extracts energy from chemical substances in the system and further exhibits mechanical function by using them. The interplay between the structural dynamics of such a small object and the associated chemical reaction is crucial for a micromachine.

Owing to the development of nonequilibrium statistical mechanics and the improvement of experimental techniques, many researches have been conducted to reveal the energetics of micromachines. For example, the energy efficiency of F1-ATPase motor and Kinesin has been experimentally obtained by using the Harada-Sasa relation [6.3–6.5]. On the other hand, attention has been also paid to the dynamics of micromachines. For instance, several works reported that the diffusion coefficients of metabolic enzymes increase due to enzymatic reactions [6.6–6.8]. Although several possible scenarios have been proposed such as self-heat diffusion, swimming, and macroscopic heating, the main physical mechanism for the enhanced diffusion is not yet specified [6.7].

Biological functions of a micromachine is intimately related to the transition between its different internal states. As depicted in Fig. 6.1(a), we can use time-dependent state variables $s_i(t)$ to characterize such as the conformational structure or the adhesion state when a micromachine is interacting with a substrate. The state variables $s_i(t)$ change dynamically when a micromachine catalyzes a chemical reaction of substrate molecules. As long as a micromachine acts as a catalyst, however, the internal state should return to the initial state after one cycle of reaction. Hence, the state variables $s_i(t)$ should change periodically in time as the chemical reaction occurs repeatedly.

In overdamped systems, such a state cycle is intimately related to biological functions of a micromachine. For example, microswimmers in a viscous fluid have been investigated by using a three-sphere model [6.9] or within the frame-

work of a gauge theory [6.10]. It is known that the average swimming velocity is proportional to the closed loop area in the deformation space, as shown in Fig. 6.1(b). In order to extend this concept and to generally characterize the functionality of a micromachine, I introduce the following quantity

$$C_{ij} = \int_0^{\tau_c} dt \dot{s}_i s_j, \quad (6.1)$$

where $\dot{s}_i = ds_i/dt$ and τ_c is the period of a state cycle. In this chapter, I shall call the quantity C_{ij} as the “state cyclone”.

For a three-sphere microswimmer, s_1 and s_2 correspond to the lengths of the two arms, and the average swimming velocity V over one cycle is directly proportional to the state cyclone, i.e., $V \sim C_{12}$ [6.9]. Such a relation holds not only for a deterministic microswimmer, but also for a stochastic microswimmer [6.11, 6.12]. Within a gauge theory, shape deformation of an object can be expanded in terms of the proper eigenfunctions. Then, the average velocity is generally given by $V = \sum_{i,j} W_{ij} C_{ij}$, where W_{ij} is a tensor that connects the velocity and the state cyclone [6.10]. The state cyclone is also relevant to a crawling motion of a cell on a substrate [6.13, 6.14].

Although the functionality of a micromachine is characterized by C_{ij} , it is not known how the state cyclone is regulated within a micromachine. In this chapter, I consider an active micromachine that utilizes a catalytic chemical reaction, and investigate the relationship between the properties of the chemical reaction and the state cyclone. For this purpose, I consider an additional variable $\theta(t)$ that represents the degree of the chemical reaction. My purpose is to propose a minimum model of a micromachine undergoing a state transition that is driven by a catalytic chemical reaction.

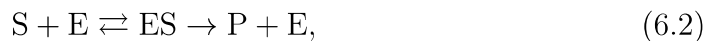
I consider a tilted periodic potential to describe the catalytic reaction and a periodic coupling free energy between s_i and θ . Onsager’s phenomenological equations are employed for the time evolution of these variables. I assume that the dynamics of θ is described by a step function characterized by two typical

time scales, i.e., the mean first passage time τ_p and the mean first transition path time τ_t . Solving the equations for the state variables s_i , I analytically obtain the state cyclone C_{12} as a function of these time scales. Moreover, I give analytical expressions for τ_p and τ_t in the weak coupling limit. I shall discuss in detail how these quantities are related to the properties of the chemical reaction.

In Sec. 6.2, I introduce my minimum model. Then I discuss the dynamics of the state variables in Sec. 6.3. In Sec. 6.4, I calculate the state cyclone analytically. In Sec. 6.5, I obtain the mean first passage time and the mean first transition path time. Finally, a summary of my work and a discussion is provided in Sec. 6.6.

6.2 Model

In this section, I describe my model of a micromachine driven by a catalytic chemical reaction. Consider a system which contains one enzyme molecule (E) that plays a role of a micromachine, n_S substrate molecules (S), and n_P product molecules (P). The enzyme molecule acts as a catalyst and the corresponding chemical reaction is written as



where ES indicates a complex molecule. The reaction rate \dot{n}_P is often analyzed by the Michaelis-Menten equation [6.15]. Although the above chemical reaction is relevant to the present study, my purpose is to adopt the simplest model for such a chemical reaction and not to reproduce it.

The extent of a catalytic reaction is commonly described by the number of product molecules n_P . However, since my purpose is to investigate a single molecular reaction process, I introduce a reaction variable $\theta(t)$ to quantify the extent of the catalytic reaction. Unlike n_P , the reaction variable θ is continuous and increases 2π for each reaction. By using θ , the catalytic reaction can be described by the Kramers theory [6.16].

According to the Kramers theory, the free energy G_r describing the chemical

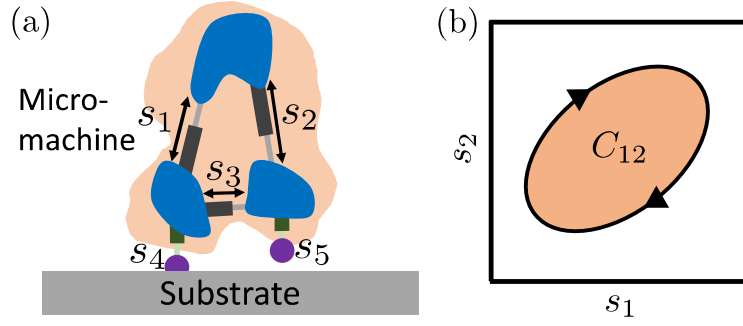


Figure 6.1: (a) Schematic picture of a micromachine characterized by the conformational state variables s_1 , s_2 , and s_3 . Moreover, the adhesion between the domains and the substrate is described by the variables s_4 and s_5 . (b) The state transition of a micromachine is represented by a trajectory in the state space spanned by the variables s_1 and s_2 . The state cyclone C_{12} [see Eq. (6.1)] corresponds to the area enclosed by the trajectory.

reaction is given by

$$G_r(\theta) = G_p(\theta) - F\theta, \quad (6.3)$$

where G_p is a periodic free energy with the period of 2π , i.e., $G_p(\theta+2\pi) = G_p(\theta)$. As shown in Fig. 6.2(a), the amplitude of G_p , denoted by A , represents the energy barrier in the chemical reaction and is regarded as the activation energy. The explicit form of G_p will be presented later. On the other hand, F in Eq. (6.3) represents the chemical potential difference that drives the chemical reaction. The system is in chemical equilibrium when $F = 0$, whereas it is in out-of-equilibrium situation when $F \neq 0$. In this chapter, we shall consider the case of $F > 0$ and call F as the nonequilibrium force (even though it has the dimension of energy).

Next, I introduce the state variables s_i with $i = 1, 2, 3, \dots$ characterizing the conformation of a micromachine. As shown in Fig. 6.1(a), the examples of the state variable are the distances between the domains in a micromachine or the distances between the domains and the substrate (if it exists). In principle, there is a large number of degrees of freedom of a micromachine, and the number of the state variable can be also large.

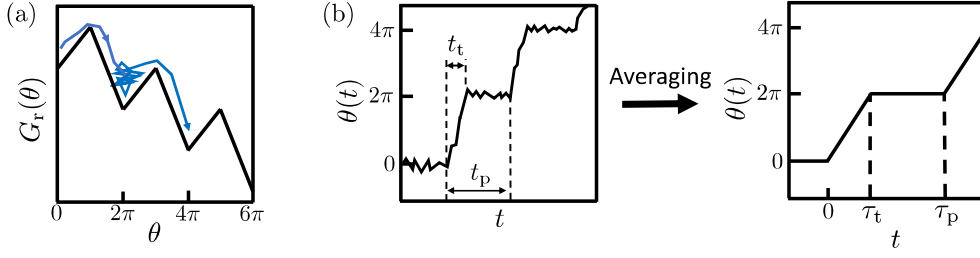


Figure 6.2: (a) The tilted periodic free energy G_r as a function of the reaction variable θ . As shown in Eqs. (6.3) and (6.23), G_r is characterized by the height of the energy barrier A and the nonequilibrium force F , whereas the periodic part G_p has the periodicity of 2π . (b) An example of stochastic time evolution of the reaction variable θ (left). Such a time evolution is characterized by the first transition path time t_t and the first passage time t_p which are both stochastic. After averaging over these quantities, we obtain the average time evolution of θ (right) as assumed in Eq. (6.15). Here τ_t and τ_p are the mean first transition path time the mean first passage time, respectively. The reaction variable increases linearly for $0 \leq t < \tau_t$ and stays constant for $\tau_t \leq t < \tau_p$. The function θ satisfies $\theta(t + \tau_p) = \theta(t) + 2\pi$.

Because we are considering a catalytic reaction, the internal state of a micromachine should return to the initial state after one cycle of reaction. Hence the state variable s_i is expected to change also periodically as the reaction variable θ evolves in time. With these requirements, I consider the following coupling energy between θ and s_i :

$$G_c(\theta, \{s_i\}) = \sum_i \frac{K_i}{2} [s_i - d_i \sin(\theta + \phi_i)]^2. \quad (6.4)$$

Here K_i is the coupling parameter, d_i is the amplitude, and ϕ_i is the phase difference. The total free energy G_t in my model is simply given by

$$G_t(\theta, \{s_i\}) = G_r(\theta) + G_c(\theta, \{s_i\}). \quad (6.5)$$

For the time evolutions of θ and s_i , I employ the Onsager's phenomenological equations [6.17]

$$\dot{\theta} = -M \frac{\partial G_t}{\partial \theta} + \xi(t), \quad (6.6)$$

$$\dot{s}_i = - \sum_j \mu_{ij} \frac{\partial G_t}{\partial s_j} + \xi_i(t). \quad (6.7)$$

Here, M and μ_{ij} are the dynamical coefficients for θ and s_i , respectively, while

ξ and ξ_i represent thermal fluctuations which satisfy the fluctuation-dissipation theorem

$$\langle \xi(t) \rangle = 0, \quad (6.8)$$

$$\langle \xi(t)\xi(t') \rangle = 2Mk_B T \delta(t - t'), \quad (6.9)$$

$$\langle \xi_i(t) \rangle = 0, \quad (6.10)$$

$$\langle \xi_i(t)\xi_j(t') \rangle = 2\mu_{ij}k_B T \delta(t - t'), \quad (6.11)$$

where k_B is the Boltzmann constant and T is the temperature.

Although the above model is general, I make several simplifying assumptions in order to solve the coupled equations analytically. First, we only take into account two degrees of freedom, i.e., s_1 and s_2 . Second, the mobility coefficients μ_{ij} is assumed to have the form $\mu_{11} = \mu_{22} = \mu$ and $\mu_{12} = \mu_{21} = 0$. Third, the coupling free energy is symmetric between the two degrees of freedom, i.e., $K_1 = K_2 = K$ and $d_1 = d_2 = d$. Then Eqs. (6.6) and (6.7) reduce to

$$\dot{\theta} = -M[\partial_\theta G_r(\theta) - Kd \cos(\theta + \phi_1)\delta_1 - Kd \cos(\theta + \phi_2)\delta_2] + \xi, \quad (6.12)$$

$$\dot{\delta}_1 = -\gamma\delta_1 - d \cos(\theta + \phi_1)\dot{\theta} + \xi_1, \quad (6.13)$$

$$\dot{\delta}_2 = -\gamma\delta_2 - d \cos(\theta + \phi_2)\dot{\theta} + \xi_2, \quad (6.14)$$

where we have introduced the notations $\gamma = \mu K$ and $\delta_i = s_i - d \sin(\theta + \phi_i)$.

In the following sections, I analyze the above coupled equations to estimate the state cyclone C_{12} given in Eq. (6.1). To do so, we first solve Eqs. (6.13) and (6.14) for δ_i (s_i) by assuming a simple functional form of θ . After that, Eq. (6.12) will be used to determine the two characteristic time scales of θ .

6.3 Dynamics of the state variable

In this section, I discuss the dynamics of the state variables δ_1 (s_1) and δ_2 (s_2) obeying Eqs. (6.13) and (6.14), respectively. To solve these equations, we make an assumption for the time dependence of θ . With the tilted periodic potential given by Eq. (6.3) and shown in Fig. 6.2(a), the reaction variable θ changes stochastically across the energy barriers and the value of θ increases over a long

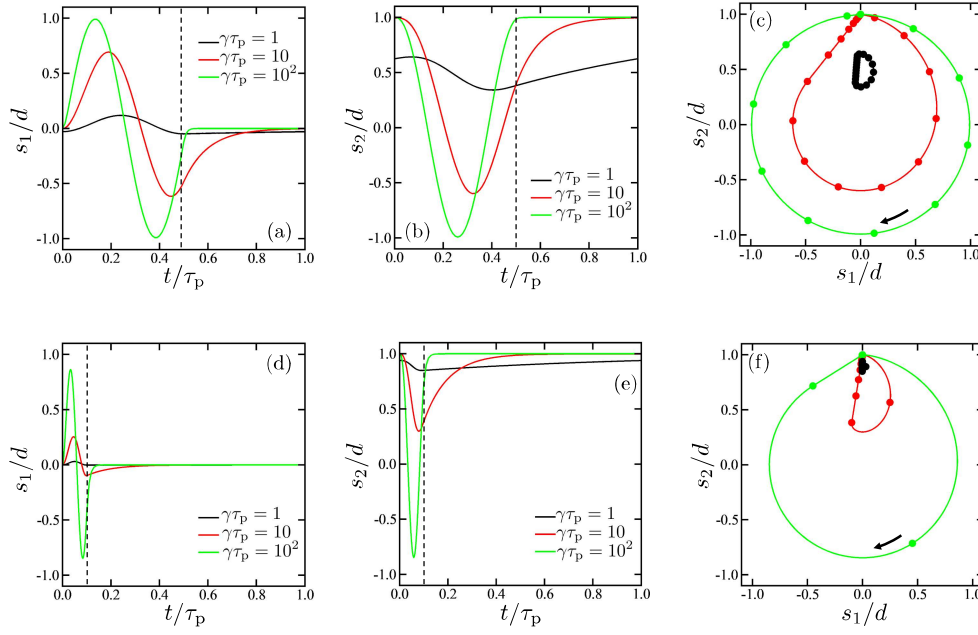


Figure 6.3: Time evolutions of (a) s_1 and (b) s_2 when $\phi_1 = 0$ and $\phi_2 = \pi/2$. I set $\tau_t/\tau_p = 0.5$ (shown by the dashed line) and change $\gamma\tau_p = 1$ (black), 10 (red), and 10^2 (green). (c) The trajectory of the state variables s_1 and s_2 shown in (a) and (b), respectively, over one period of cycle. For each cycle, 20 equal time intervals are marked by the filled circles. The black arrow indicates the direction of the state transition. The enclosed area of the trajectory corresponds to the state cyclone C_{12} . (d), (e), and (f) are the similar plots to (a), (b), and (c), respectively, when $\tau_t/\tau_p = 0.1$ (shown by the dashed line).

time. Such a time evolution can be characterized by two characteristic time scales. The first one is the “first passage time” t_p which is the time required to change from one local minimum to the neighboring lower local minimum [6.16]. The second one is the “first transition path time” t_t which is the time needed for the actual transition [6.18–6.20]. It should be noticed that both t_p and t_t are stochastic quantities.

In order to discuss the dynamics of s_1 and s_2 , let us assume that θ follows a deterministic stepwise function characterized by the “mean first passage time” τ_p and the “mean first transition path time” τ_t which are the averages of t_p and

t_t , respectively. As presented in Fig. 6.2(b), the assumed functional form of θ is

$$\theta(t) = \begin{cases} 2\pi t/\tau_t & \text{for } 0 \leq t < \tau_t \\ 2\pi & \text{for } \tau_t \leq t < \tau_p \end{cases}. \quad (6.15)$$

Furthermore, we require that θ increases by 2π after one cycle of reaction τ_p , i.e., $\theta(t + \tau_p) = \theta(t) + 2\pi$. The explicit expressions of τ_p and τ_t will be given in Sec. 6.5 where we focus on their dependencies on A and F .

Substituting Eq. (6.15) into Eqs. (6.13) and (6.14), we solve them in the absence of thermal noise, i.e., $\xi_1 = \xi_2 = 0$ [see Appendix 6.A for the details].

Then the stationary solution for δ_i ($i = 1, 2$) can be obtained as

$$\delta_i(t) = \frac{d}{(\gamma\tau_t/2\pi)^2 + 1} \left[-\frac{\gamma\tau_t}{2\pi} \cos\left(\frac{2\pi t}{\tau_t} + \phi_i\right) - \sin\left(\frac{2\pi t}{\tau_t} + \phi_i\right) + \frac{e^{\gamma\tau_p} - e^{\gamma\tau_t}}{e^{\gamma\tau_p} - 1} \left(\frac{\gamma\tau_t}{2\pi} \cos\phi_i + \sin\phi_i \right) e^{-\gamma t} \right], \quad (6.16)$$

for $0 \leq t < \tau_t$ and

$$\delta_i(t) = -\frac{d}{(\gamma\tau_t/2\pi)^2 + 1} \frac{e^{\gamma\tau_p}(e^{\gamma\tau_t} - 1)}{e^{\gamma\tau_p} - 1} \left(\frac{\gamma\tau_t}{2\pi} \cos\phi_i + \sin\phi_i \right) e^{-\gamma t}, \quad (6.17)$$

for $\tau_t \leq t < \tau_p$.

In Figs. 6.3(a) and (b), I plot the time evolutions of s_1 and s_2 , respectively, when $\phi_1 = 0$ and $\phi_2 = \pi/2$. I set $\tau_t/\tau_p = 0.5$ and change $\gamma\tau_p = 1, 10$, and 10^2 . When $\gamma\tau_p = 10^2$ (green), the behaviors for $0 \leq t < \tau_t$ are well described by sinusoidal functions $s_1/d = \sin(2\pi t/\tau_t)$ and $s_2/d = \cos(2\pi t/\tau_t)$. In this strong coupling case (notice that $\gamma = \mu K$), we see a sufficiently large state change within a micromachine. In the weaker coupling case, such as when $\gamma\tau_p = 1$ or 10 (black or red), s_i cannot follow the change in θ and the functionality of a micromachine is suppressed. In Fig. 6.3(c), I plot the trajectories of s_1 and s_2 over one period of cycle for different values of $\gamma\tau_p$. For each cycle, 20 equal time intervals are marked by the filled circles. As mentioned before, the enclosed area of each trajectory gives the state cyclone C_{12} .

In Figs. 6.3(d), (e), and (f), I show the corresponding plots when $\tau_t/\tau_p = 0.1$. When $\gamma\tau_p = 10^2$ (green) and $0 \leq t < \tau_t$, both s_1 and s_2 are well described

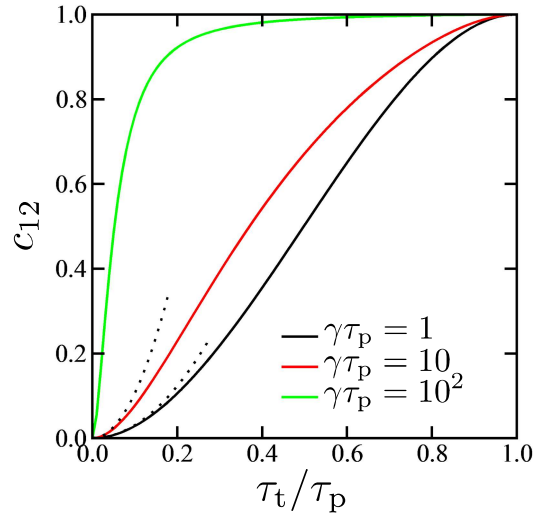


Figure 6.4: The dimensionless state cyclone $c_{12} = 4\pi C_{12}[(\gamma\tau_p/2\pi)^2 + 1]/[d^2\gamma^2\tau_p^2 \sin(\phi_2 - \phi_1)]$ as a function of τ_t/τ_p for $\gamma\tau_p = 1$ (black), 10 (red), and 10^2 (green). The dotted lines are the asymptotic expression in Eq. (6.20) for $\tau_t/\tau_p \ll 1$.

by the same sinusoidal functions as in Figs. 6.3(a) and (b), respectively. On the other hand, the black and red curves for $\gamma\tau_p = 1$ and 10, respectively, deviate significantly from the green curve for $\gamma\tau_p = 10^2$, and their amplitudes are significantly diminished. These reduced amplitudes can also be seen in Fig. 6.3(f) where the areas enclosed by the black and red lines are much smaller than the area enclosed by the green line. This means that, in the weaker coupling case, the state cyclone is further decreased as τ_t/τ_p is made smaller.

6.4 State cyclone of a micromachine

I have mentioned before that the state cyclone defined in Eq. (6.1) provides us with a quantity to evaluate the functionality of a micromachine [6.9–6.11, 6.13, 6.14]. In the previous works, the state cyclone was obtained along a deterministic state change when the period of deformation is constant. On the other hand, this is not always possible when fluctuations are present [6.21]. For a stochastic micromachine, it is necessary either to take a long time limit or to estimate the statistical average to obtain the state cyclone. In the present analysis, however,

one can calculate the state cyclone directly from Eq. (6.1) because we have assumed a deterministic dynamics for θ .

By using the results in Eqs. (6.16) and (6.17), the state cyclone C_{12} is obtained in terms of τ_p and τ_t as

$$\begin{aligned} C_{12} &= \int_0^{\tau_p} dt \dot{s}_1 s_2 \\ &= \frac{d^2 \gamma^2 \tau_t^2}{4\pi[(\gamma\tau_t/2\pi)^2 + 1]} \left[1 + \frac{2[1 + e^{\gamma\tau_p} - e^{\gamma\tau_t} - e^{\gamma(\tau_p - \tau_t)}]}{\gamma\tau_t[(\gamma\tau_t/2\pi)^2 + 1](e^{\gamma\tau_p} - 1)} \right] \sin(\phi_2 - \phi_1). \end{aligned} \quad (6.18)$$

This is the main result of this work. Since C_{12} is proportional to $\sin(\phi_2 - \phi_1)$, it vanishes when $\phi_1 = \phi_2$. In other words, the state variables s_1 and s_2 should be out-of-phase ($\phi_1 \neq \phi_2$) in order to exhibit its functionality. This result is related to the scallop theorem for a microswimmer [6.9, 6.10]. Moreover, the state cyclone satisfies the symmetry property such that $C_{12} = -C_{21}$.

From Eq. (6.18), the asymptotic expressions of C_{12} can be obtained as

$$C_{12} \approx \frac{d^2 \gamma^2 \tau_p^2}{4\pi[(\gamma\tau_p/2\pi)^2 + 1]} \sin(\phi_2 - \phi_1) \quad \text{for } \tau_t/\tau_p \approx 1, \quad (6.19)$$

$$C_{12} \approx \frac{3d^2 \gamma^2 \tau_t^2}{4\pi} \sin(\phi_2 - \phi_1) \quad \text{for } \tau_t/\tau_p \ll 1. \quad (6.20)$$

In Fig. 6.4, I plot the dimensionless state cyclone c_{12} as a function of the ratio τ_t/τ_p for different values of $\gamma\tau_p$. The dotted lines represent the asymptotic expression in Eq. (6.20). From this plot, one can confirm the scaling behavior $C_{12} \sim (\gamma\tau_t)^2$ when $\tau_t/\tau_p \ll 1$. When $\tau_t/\tau_p \approx 1$, on the other hand, c_{12} approaches unity as can be confirmed by Eq. (6.19).

6.5 Two characteristic time scales

The dynamics of a chemical reaction is generally characterized by the mean first passage time τ_p and the mean first transition path time τ_t . According to the Kramers theory, τ_p gives the time to overcome an energy barrier, and the inverse of it is a chemical reaction rate [6.16]. While most of the first passage time is spent by the waiting time, the actual time required for a state

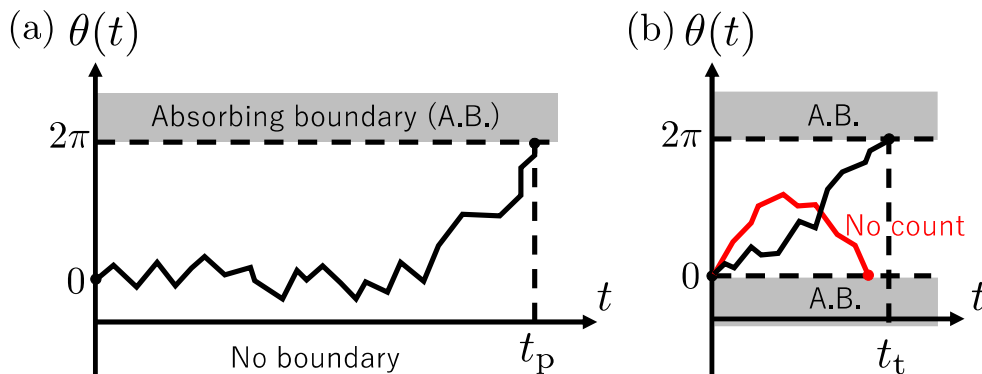


Figure 6.5: (a) Schematic description of the first passage time t_p . We consider a semi-infinite system with an absorbing boundary condition at $\theta = 2\pi$, and measure the time until the Brownian particle is absorbed at $\theta = 2\pi$. Here the state $\theta = 0$ can be visited multiple times, which gives rise to a long waiting time. (b) Schematic description of the first transition path time t_t . We consider a finite system with absorbing boundary conditions at $\theta = 0$ and 2π , and measure the time until the Brownian particle is absorbed at $\theta = 2\pi$. When the particle is absorbed at $\theta = 0$, such an event is not counted.

transition can be much smaller. Such a short time scale is characterized by τ_t [6.18–6.20, 6.22, 6.23], whose typical value was measured to be $\tau_t < 10^{-5}$ s for a nucleic acid folding [6.24–6.26].

In this section, we obtain the analytical expressions of τ_p and τ_t in terms of the potential parameters by considering only the dynamics of θ given by Eq. (6.12). Here we focus on the weak coupling limit, $Kd^2 \ll A$, and analyze the following simplified equation

$$\dot{\theta} = -M\partial_{\theta}G_r(\theta) + \xi. \quad (6.21)$$

With this dynamical equation for θ , one can obtain both τ_p and τ_t for a general potential [6.20].

6.5.1 Mean first passage time τ_p

The first passage time t_p is the time for a reaction that started from the initial value θ_0 reaches the final value θ_f for the first time. Notice that $\theta_0 = 0$ and $\theta_f = 2\pi$ in my model. Mathematically, this is equivalent to consider a Brownian motion of a particle in a semi-infinite system with an absorbing

boundary condition at $\theta = \theta_f$, and to measure the time until the particle is absorbed at $\theta = \theta_f$ [see Fig. 6.5 (a)]. However, because the state $\theta = \theta_0$ can be visited multiple times, most of the first passage time is spent by a long waiting time. Since t_p is a stochastic quantity and has a broad distribution, it is useful to consider its average τ_p .

A formal derivation of τ_p is explained in Appendix 6.B. For an arbitrary periodic function G_p , τ_p can be obtained as

$$\tau_p = \frac{1}{D(1 - e^{-2\pi f})} \int_0^{2\pi} dx \int_0^{2\pi} dy \exp[g_p(x) - g_p(x - y) - fy], \quad (6.22)$$

where $g_p = G_p/(k_B T)$ and $f = F/(k_B T)$ are the dimensionless potential and nonequilibrium force, respectively, and $D = Mk_B T$ is the diffusion constant. Note that D has the dimension of inverse time in the present model.

For the sake of simplicity, we assume that G_p is given by the combination of the following linear functions:

$$G_p(\theta) = \begin{cases} A \left(\frac{2}{\pi} \theta - 1 \right) & \text{for } 0 \leq \theta < \pi \\ A \left(-\frac{2}{\pi} \theta + 3 \right) & \text{for } \pi \leq \theta < 2\pi \end{cases}. \quad (6.23)$$

With this periodic potential, one can analytically obtain τ_p as

$$\tau_p = \frac{2\pi^2}{D} \left[\frac{\pi f}{\pi^2 f^2 - 4a^2} - \frac{8a^2}{(\pi^2 f^2 - 4a^2)^2} \frac{1 + e^{-2\pi f}}{1 - e^{-2\pi f}} + \frac{16a^2 \cosh(2a)}{(\pi^2 f^2 - 4a^2)^2} \frac{e^{-\pi f}}{1 - e^{-2\pi f}} \right], \quad (6.24)$$

where $a = A/(k_B T)$ is the dimensionless energy barrier. Then the asymptotic expressions of τ_p are given as follows:

$$\tau_p \approx \frac{2\pi}{Df} = \frac{2\pi}{MF} \quad \text{when } a \ll 1 \text{ or } a \ll f, \quad (6.25)$$

$$\tau_p \approx \frac{\pi e^{2a}}{2Da^2 f} = \frac{\pi(k_B T)^2 e^{2A/k_B T}}{2MA^2 F} \quad \text{when } a \gg 1 \text{ and } f \ll 1, \quad (6.26)$$

$$\tau_p \approx \frac{\pi^2 e^{2a} e^{-\pi f}}{Da^2} = \frac{\pi^2 k_B T e^{2A/k_B T} e^{-\pi F/k_B T}}{MA^2} \quad \text{when } a \gg f \gg 1. \quad (6.27)$$

Here we have recovered the dimension in the last expressions. Since Eq. (6.25) does not depend on the temperature, thermal fluctuations are irrelevant in this limit. This is not the case for Eqs. (6.26) and (6.27) which diverge due to the

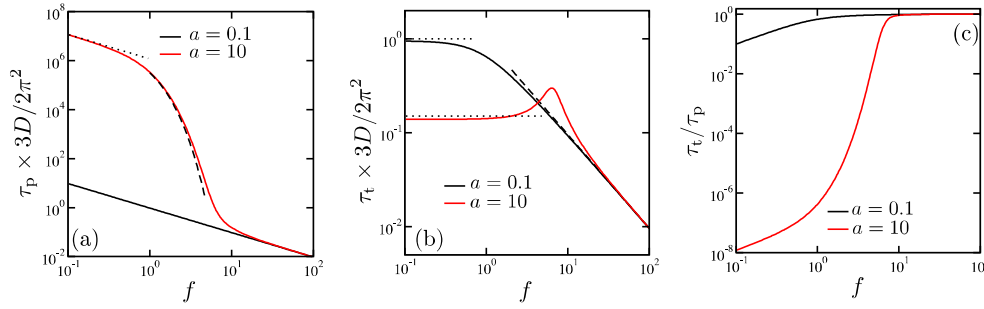


Figure 6.6: (a) The dimensionless mean first passage time τ_p as a function of the dimensionless nonequilibrium force f for $a = 0.1$ (black) and 10 (red). The plot for $a = 0.1$ almost coincides with the asymptotic form in Eq. (6.25). The dotted and dashed lines are the asymptotic expressions in Eqs. (6.26) and (6.27), respectively. (b) The dimensionless mean first transition path time τ_t as a function of the dimensionless nonequilibrium force f for $a = 0.1$ (black) and 10 (red). The dotted and dashed lines are the asymptotic expressions in Eqs. (6.35) and (6.36), respectively. The dashed-dotted line is the asymptotic expression in Eq. (6.37). (c) The ratio τ_t/τ_p as a function of the dimensionless nonequilibrium force f for $a = 0.1$ and 10. The asymptotic value of τ_t/τ_p approaches unity for large f , while it strongly depends on a for small f .

exponential factor when the temperature vanishes.

In Fig. 6.6(a), I plot the scaled τ_p in Eq. (6.24) as a function of f for $a = 0.1$ and 10. For $a = 0.1$ (black), the entire behavior is simply approximated by Eq. (6.25). For $a = 10$ (red), on the other hand, I have plotted Eqs. (6.26) (dotted line) and (6.27) (dashed line) which are in good agreement with the full expression of τ_p .

6.5.2 Mean first transition path time τ_t

The first transition path time t_t is the time for a reaction that started from the initial value θ_0 reaches the final value θ_f without returning to θ_0 . Mathematically, this is equivalent to consider a Brownian motion of a particle in a finite system with absorbing boundary conditions both at $\theta = \theta_0$ and $\theta = \theta_f$, and to measure the time until the particle is absorbed at $\theta = \theta_f$ [see the black trajectory in Fig. 6.5 (b)]. When the particle is absorbed at $\theta = \theta_0$, such an event is not counted [see the red trajectory in Fig. 6.5 (b)]. Since t_t is also a random quantity, we consider its average τ_t .

A formal derivation of τ_t is explained in Appendix 6.C, and the result is given by

$$\tau_t = \frac{1}{D} \left[\int_0^{2\pi} dw \exp[g_r(w)] \right]^{-1} \times \int_0^{2\pi} dx \exp[-g_r(x)] \int_x^{2\pi} dy \exp[g_r(y)] \int_0^x dz \exp[g_r(z)], \quad (6.28)$$

where $g_r = G_r/(k_B T)$. Using Eqs. (6.3) and (6.23), we can analytically obtain τ_t as

$$\tau_t = \frac{2\pi^2}{D} \frac{\Xi_0 + \Xi_1(\pi f) + \Xi_2(\pi f)^2 + \Xi_3(\pi f)^3 + \Xi_4(\pi f)^4}{[2a(1 - 2e^{2a}e^{\pi f} + e^{2\pi f}) + \pi f(e^{2\pi f} - 1)](\pi^2 f^2 - 4a^2)^2}, \quad (6.29)$$

where

$$\Xi_0 = -2(2a)^4 e^{2a} e^{\pi f} + (2a)^3 (e^{-2a} e^{\pi f} + 3e^{2a} e^{\pi f} - 2 - 2e^{2\pi f}), \quad (6.30)$$

$$\Xi_1 = (2a)^3 (1 - e^{2\pi f}) + 3(2a)^2 (1 - e^{2\pi f}), \quad (6.31)$$

$$\Xi_2 = (2a)^2 (-1 + 2e^{2a} e^{\pi f} - 3e^{2\pi f}) + (2a) (-e^{-2a} e^{\pi f} + 5e^{2a} e^{\pi f} - 2e^{2\pi f} - 2), \quad (6.32)$$

$$\Xi_3 = 2a(e^{2\pi f} - 1) - (e^{2\pi f} - 1), \quad (6.33)$$

$$\Xi_4 = e^{2\pi f} + 1. \quad (6.34)$$

Then the asymptotic expressions of τ_t are given as follows:

$$\tau_t \approx \frac{2\pi^2}{3D} = \frac{2\pi^2}{3Mk_B T} \quad \text{when } a \ll 1 \text{ and } f \ll 1, \quad (6.35)$$

$$\tau_t \approx \frac{2\pi}{Df} = \frac{2\pi}{MF} \quad \text{when } f \gg 1 \text{ and } a \ll f, \quad (6.36)$$

$$\tau_t \approx \frac{\pi^2}{Da} = \frac{\pi^2}{MA} \quad \text{when } a \gg 1 \text{ and } a \gg f. \quad (6.37)$$

In the limit of Eq. (6.35), the transition process is dominated by thermal fluctuations. On the other hand, Eqs. (6.36) and (6.37) are independent of the temperature, and the transitions occur deterministically. The scaling relation $\tau_t \sim 1/a$ in Eq. (6.37) was also obtained before for a quadratic potential [6.27].

In Fig. 6.6(b), I plot the scaled τ_t as a function of f for $a = 0.1$ and 10. For $a = 0.1$ (black), τ_t is constant for $f < 1$ and it decreases for $f > 1$. This behavior is in accordance with the asymptotic expressions in Eqs. (6.35) (dotted line) and

(6.36) (dashed line). For $a = 10$ (red), on the other hand, τ_t takes a maximum value around $f \approx a$. The dashed-dotted line is the asymptotic expression in Eq. (6.37).

In Fig. 6.6(c), I plot the ratio τ_t/τ_p as a function of f for $a = 0.1$ and 10. For $a = 0.1$ (black), a power law dependence is seen for $f < 1$, and τ_t/τ_p approaches unity for $f > 1$. For $a = 10$ (red), on the other hand, τ_t/τ_p is vanishingly small for $f < 1$, and it grows exponentially for $1 < f < a$.

It is worth mentioning the characteristic difference between τ_p and τ_t . In the limit of $f \rightarrow 0$, τ_p diverges while τ_t remains finite. This is because a nonequilibrium force is required for the net chemical reaction with a finite τ_p . On the other hand, τ_t can be evaluated even in the equilibrium case.

6.6 Summary and discussion

In this chapter, I have discussed cyclic state transitions of a micromachine driven by a catalytic chemical reaction. I have proposed a minimum model of a generic micromachine and calculated the state cyclone in Eq. (6.1) to quantify its functionality. My model uses the reaction variable θ and the state variables s_i which are coupled to each other through the free energy. The tilted periodic potential for θ is characterized by the energy barrier A and the nonequilibrium chemical force F . Importantly, the state variable s_i is required to change periodically in time for a catalytic reaction.

In the analysis, I have assumed that θ obeys a deterministic stepwise dynamics characterized by the mean first passage time τ_p and the mean first transition path time τ_t . Under this assumption, I have first obtained the time dependencies of the state variables s_1 and s_2 . I find that their amplitudes become smaller when either τ_t/τ_p or $\gamma\tau_p$ is decreased. Then I have calculated the state cyclone C_{12} analytically [see Eq. (6.18)]. One of the important results is the scaling relation $C_{12} \sim (\gamma\tau_t)^2$ for $\tau_t/\tau_p \ll 1$. In the small coupling limit, we have further obtained τ_p [see Eq. (6.24)] and τ_t [see Eq. (6.29)] in terms of the potential

parameters A and F .

In my result, the state cyclone has been obtained in terms of τ_p and τ_t , whereas they can further be expressed by A and F . For a realistic chemical reaction such as ATP hydrolysis, τ_t/τ_p is typically small, and I expect that the limit in Eq. (6.20) is appropriate for C_{12} . As for the estimate of τ_t , we use Eq. (6.37) by assuming a is large. Using the corresponding asymptotic expressions, we obtain approximately

$$C_{12} \sim \frac{d^2 \gamma^2}{D^2 a^2} \sin(\phi_2 - \phi_1) \sim \frac{d^2 \mu^2 K^2}{M^2 A^2} \sin(\phi_2 - \phi_1). \quad (6.38)$$

The scaling relation $C_{12} \sim 1/A^2$ implies that the higher the energy barrier is, the smaller the state cyclone becomes. This scaling relation is also an important outcome of the present model.

Here I give some typical values of the model parameters. From the experiment measuring the enhanced diffusion, the activation energy of ATP was estimated to be $A \sim 10 k_B T$ [6.28]. When a single ATP molecule is converted into ADP, the produced energy is roughly $20 k_B T$ [6.4]. Hence I estimate the nonequilibrium chemical force as $F \sim 20/(2\pi) k_B T \sim 3 k_B T$ so that both $A/k_B T > 1$ ($a > 1$) and $A > F$ ($a > f$) are satisfied. Moreover, one can estimate from Eqs. (6.26) and (6.37) that $\tau_t/\tau_p \sim 10^{-6} \ll 1$, which justifies the assumption used in Eq. (6.38).

Recent experiments reported the diffusion enhancement of enzymes due to chemical reactions [6.6, 6.8]. When a self-propelled particle undergoes a rotational diffusion, its translational diffusion coefficient increases by $\Delta D = V^2 \tau_{\text{rot}}$, where V is the propulsion velocity and τ_{rot} is the rotational diffusion time [6.29]. Since the propulsion velocity is proportional to the state cyclone, i.e., $V \sim C$, the diffusion enhancement can be written as $\Delta D \sim C^2 \tau_{\text{rot}} \sim \tau_{\text{rot}}/A^4$. So far, the relation between the activation energy and the functionality of a micromachine has not yet been investigated. We predict that the change in the activation energy can be reflected in the diffusion enhancement of enzymes.

In this study, I have mainly discussed the case when there are only two degrees of freedom of a micromachine. Although this is a minimum but sufficient number, one needs to take into account many state variables to describe the dynamics of realistic enzymes. As mentioned in Introduction, the total functionality of a micromachine can be generally expressed by the quantity $\sum_{i,j} W_{ij} C_{ij}$, where W_{ij} is the weight tensor that depends on the type of the micromachine and its environment. Hence it is necessary to evaluate the state cyclones for all the combinations of the state variables. Although the estimation of the weight tensor W_{ij} is beyond the scope of this work, such a study will be important in the future.

In the present work, the time scales τ_p and τ_t have been obtained only in the weak coupling limit, $Kd^2 \ll A$. The study of the opposite strong coupling limit is left as a future work. In this limit, both θ and s_i need to be solved simultaneously because they are strongly coupled to each other.

6.A Derivation of Eqs. (6.16) and (6.17)

In this Appendix, I show the derivation of Eqs. (6.16) and (6.17). In the absence of the noise terms, Eqs. (6.13) and (6.14) can be formally solved as

$$\delta_i(t) = -e^{-\gamma t} \int_{-\infty}^t dt' e^{\gamma t'} d \cos[\theta(t') + \phi_i] \dot{\theta}(t'), \quad (6.39)$$

where we have assumed $0 \leq t \leq \tau_p$ and ignored a term that depends on the initial condition. Using Eq. (6.15) for θ and the condition $\theta(t + \tau_p) = \theta(t) + 2\pi$, we obtain

$$\begin{aligned} \delta_i(t) = & -\frac{2\pi}{\tau_t} de^{-\gamma t} \left[\int_0^t dt' e^{\gamma t'} \cos\left(\frac{2\pi t'}{\tau_t} + \phi_i\right) \Theta(\tau_t - t') \right. \\ & \left. - \sum_{n=1}^{\infty} \int_{-n\tau_p}^{-n\tau_p + \tau_t} dt' e^{\gamma t'} \cos\left[\frac{2\pi}{\tau_t}(t' + n\tau_p) + \phi_i\right] \right], \quad (6.40) \end{aligned}$$

where $\Theta(t)$ is the Heaviside step function. Changing the variable to $t'' = t' + n\tau_p$ in the second integral, we obtain

$$\delta_i(t) = -\frac{2\pi}{\tau_t} de^{-\gamma t} \left[\int_0^t dt' e^{\gamma t'} \cos\left(\frac{2\pi t'}{\tau_t} + \phi_i\right) \Theta(\tau_t - t') \right.$$

$$- \sum_{n=1}^{\infty} e^{-\gamma n \tau_p} \int_0^{\tau_t} dt'' e^{\gamma t''} \cos\left(\frac{2\pi t''}{\tau_t} + \phi_i\right) \Bigg], \quad (6.41)$$

which results in Eqs. (6.16) and (6.17) after the integration.

6.B Derivation of Eq. (6.22)

In this Appendix, I show the derivation of the mean first passage time τ_p in Eq. (6.22) [6.16, 6.30, 6.31]. For this purpose, we consider a conditional probability distribution $P(\theta, t|\theta_0)$ for which $\theta(t=0) = \theta_0$ is imposed as the initial condition. Then $P(\theta, t|\theta_0)$ satisfies the following Fokker-Planck equation:

$$\partial_t P(\theta, t|\theta_0) = \mathcal{L}(\theta)P(\theta, t|\theta_0), \quad (6.42)$$

$$\mathcal{L}(\theta) = D\partial_\theta \exp[-g_r(\theta)]\partial_\theta \exp[g_r(\theta)]. \quad (6.43)$$

Similarly, $P(\theta, t|\theta_0)$ also satisfies the following backward Fokker-Planck equation:

$$\partial_t P(\theta, t|\theta_0) = \mathcal{L}^\dagger(\theta_0)P(\theta, t|\theta_0), \quad (6.44)$$

$$\mathcal{L}^\dagger(\theta_0) = D \exp[g_r(\theta_0)]\partial_{\theta_0} \exp[-g_r(\theta_0)]\partial_{\theta_0}. \quad (6.45)$$

We employ the reflective boundary condition at $\theta \rightarrow -\infty$ and the absorbing boundary condition at $\theta = 2\pi$. Then the total probability distribution decays due to the latter boundary condition. Here we introduce the survival probability defined as

$$S(t, \theta_0) = \int_{-\infty}^{2\pi} d\theta P(\theta, t|\theta_0). \quad (6.46)$$

Then the distribution function of the first passage time is given by

$$K_p(t, \theta_0) = -\frac{dS}{dt}. \quad (6.47)$$

From the condition $S(t=0) = 1$, the following normalization condition holds

$$\int_0^\infty dt K_p(t, \theta_0) = 1. \quad (6.48)$$

The mean first passage time τ_p is defined as the first moment of the distribution function

$$\tau_p(\theta_0) = \int_0^\infty dt t K_p(t, \theta_0). \quad (6.49)$$

Next, one can show from Eqs. (6.44), (6.46), (6.47), and (6.49) that

$$-1 = \mathcal{L}^\dagger(\theta_0)\tau_p(\theta_0), \quad (6.50)$$

where we have used the conditions $\lim_{t \rightarrow 0} tK_p(t) = 0$ and $\lim_{t \rightarrow \infty} tK_p(t) = 0$. Using the reflective boundary condition ($\partial_{\theta_0}\tau_p = 0$ at $\theta_0 \rightarrow -\infty$) and the absorbing boundary conditions ($\tau_p = 0$ at $\theta_0 = 2\pi$), one can solve the above equation to obtain [6.32],

$$\tau_p(\theta_0) = \frac{1}{D} \int_{\theta_0}^{2\pi} dx \exp[g_r(x)] \int_{-\infty}^x dY \exp[-g_r(Y)]. \quad (6.51)$$

Setting $\theta_0 = 0$ and using Eq. (6.3), we get

$$\tau_p = \frac{1}{D} \int_0^{2\pi} dx \int_0^\infty dy' \exp[g_p(x) - g_p(x - y') - fy'], \quad (6.52)$$

where $y' = x - Y$. Because G_p has the periodicity of 2π , we obtain

$$\tau_p = \frac{1}{D} \sum_{n=0}^{\infty} e^{-2n\pi F} \int_0^{2\pi} dx \int_0^{2\pi} dy \exp[g_p(x) - g_p(x - y) - fy], \quad (6.53)$$

where $y = y' - 2n\pi$. Since $F > 0$, one can easily evaluate the infinite series and obtain Eq. (6.22).

6.C Derivation of Eq. (6.28)

In this Appendix, I show the derivation of the mean first transition path time τ_t in Eq. (6.28) [6.18–6.20]. For this situation, the absorbing boundary condition is imposed both at $\theta = 0$ and $\theta = 2\pi$. Hence, unlike τ_p , the probability is absorbed from both of the boundaries, although the probability of being absorbed at $\theta = 2\pi$ determines τ_t .

The distribution function of the first transition path time is given by

$$K_t(t, \theta_0) = \frac{1}{N} J(\theta = 2\pi, t|\theta_0), \quad (6.54)$$

where $J(\theta, t|\theta_0)$ is a probability flux

$$J(\theta, t|\theta_0) = -D \exp[-g_r(\theta)] \frac{\partial}{\partial \theta} [\exp[g_r(\theta)] P(\theta, t|\theta_0)]. \quad (6.55)$$

In Eq. (6.54), N is the normalization constant that is fixed by the condition

$$\int_0^\infty dt K_t(t, \theta_0) = 1. \quad (6.56)$$

The mean first transition path time τ_t is defined as the first moment of the distribution function

$$\tau_t(\theta_0) = \int_0^\infty dt t K_t(t, \theta_0). \quad (6.57)$$

The backward Fokker-Planck equation for the probability flux J is given by

$$\partial_t J(\theta, t|\theta_0) = \mathcal{L}^\dagger(\theta_0)J(\theta, t|\theta_0). \quad (6.58)$$

From Eqs. (6.54), (6.56), and (6.58), one can show that

$$0 = \mathcal{L}^\dagger(\theta_0)N(\theta_0), \quad (6.59)$$

where we have used the conditions $J(2\pi, 0|\theta_0) = 0$ and $J(2\pi, \infty|\theta_0) = 0$. Solving this equation with the boundary conditions $N(0) = 0$ and $N(2\pi) = 1$, we obtain

$$N(\theta_0) = \int_0^{\theta_0} dy_0 \exp[g_r(y_0)] \left[\int_0^{2\pi} dy_0 \exp[g_r(y_0)] \right]^{-1}. \quad (6.60)$$

From Eqs. (6.54), (6.57), and (6.58), we obtain

$$-N(\theta_0) = \mathcal{L}^\dagger(\theta_0)\psi(\theta_0), \quad (6.61)$$

where $\psi(\theta_0) = \tau_t(\theta_0)N(\theta_0)$ and we have used the conditions $\lim_{t \rightarrow 0} t K_t(t, \theta_0) = 0$ and $\lim_{t \rightarrow \infty} t K_t(t, \theta_0) = 0$. With the use of the absorbing boundary conditions $\psi(0) = 0$ and $\psi(2\pi) = 0$, one can solve the above equation to obtain

$$\begin{aligned} \psi(\theta_0) &= \frac{1}{D} \left[\int_0^{2\pi} dw \exp[g_r(w)] \right]^{-1} \\ &\times \left[(1 - N(\theta_0)) \int_0^{\theta_0} dx \exp[-g_r(x)] N^2(x) \right. \\ &\quad \left. + N(\theta_0) \int_{\theta_0}^{2\pi} dx \exp[-g_r(x)] (1 - N(x)) N(x) \right]. \end{aligned} \quad (6.62)$$

Since $\tau_t = \lim_{\theta_0 \rightarrow 0} [\psi(\theta_0)/N(\theta_0)]$, only the second term remains and we obtain Eq. (6.28).

References

- [6.1] S. Toyabe and M. Sano, *J. Phys. Soc. Jpn.* **84**, 102001 (2015).
- [6.2] A. I. Brown and D. A. Sivak, *Chem. Rev.* **120**, 434 (2020).
- [6.3] T. Harada and S.-i. Sasa, *Phys. Rev. Lett.* **95**, 130602 (2005).
- [6.4] S. Toyabe, T. Okamoto, T. Watanabe-Nakayama, H. Taketani, S. Kudo, and E. Muneyuki, *Phys. Rev. Lett.* **104**, 198103 (2010).
- [6.5] T. Ariga, M. Tomishige, and D. Mizuno, *Phys. Rev. Lett.* **121**, 218101 (2018).
- [6.6] H. S. Muddana, S. Sengupta, T. E. Mallouk, A. Sen, and P. J. Butler, *J. Am. Chem. Soc.* **132**, 2110 (2010).
- [6.7] R. Golestanian, *Phys. Rev. Lett.* **115**, 108102 (2015).
- [6.8] A.-Y. Jee, S. Dutta, Y.-K. Cho, T. Tlusty, and S. Granick, *Proc. Natl. Acad. Sci. U.S.A.* **115**, 1 (2018).
- [6.9] R. Golestanian and A. Ajdari, *Phys. Rev. E* **77**, 036308 (2008).
- [6.10] A. Shapere and F. Wilczek, *J. Fluid Mech.* **198**, 557 (1989).
- [6.11] I. Sou, Y. Hosaka, K. Yasuda, and S. Komura, *Phys. Rev. E* **100**, 022607 (2019).
- [6.12] I. Sou, Y. Hosaka, K. Yasuda, and S. Komura, *Physica A* **562**, 125277 (2021).
- [6.13] M. Leoni and P. Sens, *Phys. Rev. Lett.* **118**, 228101 (2017).
- [6.14] M. Tarama and R. Yamamoto, *J. Phys. Soc. Jpn.* **87**, 044803 (2018).
- [6.15] K. Dill and S. Bromberg, *Molecular Driving Forces: Statistical Thermodynamics in Biology, Chemistry, Physics, and Nanoscience* (Garland Science, London and New York, 2010).

-
- [6.16] P. Hänggi, P. Talkner, and M. Borkovec, *Rev. Mod. Phys.* **62**, 251 (1990).
- [6.17] M. Doi, *Soft Matter Physics* (Oxford University, Oxford, 2013).
- [6.18] G. Hummer, *J. Chem. Phys.* **120**, 516 (2004).
- [6.19] S. Chaudhury and D. E. Makarov, *J. Chem. Phys.* **133**, 034118 (2010).
- [6.20] W. K. Kim and R. R. Netz, *J. Chem. Phys.* **143**, 224108 (2015).
- [6.21] A. Ghanta, J. C. Neu, and S. Teitworth, *Phys. Rev. E* **95**, 032128 (2017).
- [6.22] M. Laleman, E. Carlon, and H. Orland, *J. Chem. Phys.* **147**, 214103 (2017).
- [6.23] M. Caraglio, T. Sakaue, and E. Carlon, *Phys. Chem. Chem. Phys.* **22**, 3512 (2020).
- [6.24] K. Neupane, D. B. Ritchie, H. Yu, D. A. N. Foster, F. Wang, and M. T. Woodside, *Phys. Rev. Lett.* **109**, 068102 (2012).
- [6.25] H. S. Chung and W. A. Eaton, *Nature* **502**, 685 (2013).
- [6.26] K. Neupane, F. Wang, and M. T. Woodside, *Proc. Natl. Acad. Sci. U.S.A.* **114**, 1329 (2017).
- [6.27] H. S. Chung, J. M. Louis, and W. A. Eaton, *Proc. Natl. Acad. Sci. U.S.A.* **106**, 11837 (2009).
- [6.28] R. Hayashi, K. Sasaki, S. Nakamura, S. Kudo, Y. Inoue, H. Noji, and K. Hayashi, *Phys. Rev. Lett.* **114**, 248101 (2015).
- [6.29] H.-R. Jiang, N. Yoshinaga, and M. Sano, *Phys. Rev. Lett.* **105**, 268302 (2010).
- [6.30] P. Reimann, C. Van den Broeck, H. Linke, P. Hänggi, J. M. Rubi, and A. Pérez-Madrid, *Phys. Rev. Lett.* **87**, 010602 (2001).

- [6.31] K. Hayashi and S.-i. Sasa, Phys. Rev. E **69**, 066119 (2004).
- [6.32] N. Goel and N. Richter-Dyn, *Stochastic Models in Biology* (Academic Press, New York, 1974).

Chapter 7

Anomalous Diffusion Induced by Micromachines in a Structured Fluid

With the use of the “two-fluid model”, I discuss anomalous diffusion induced by active force dipoles in viscoelastic media. Active force dipoles, such as proteins and bacteria, generate non-thermal fluctuating flows that lead to a substantial increment of the diffusion. Using the partial Green’s function of the two-fluid model, I first obtain passive (thermal) two-point correlation functions such as the displacement cross-correlation function between the two point particles separated by a finite distance. I then calculate active (non-thermal) one-point and two-point correlation functions due to active force dipoles. The time correlation of a force dipole is assumed to decay exponentially with a characteristic time scale. I show that the active component of the displacement cross-correlation function exhibits various crossovers from super-diffusive to sub-diffusive behaviors depending on the characteristic time scales and the particle separation. My theoretical results are intimately related to the microrheology technique to detect fluctuations in non-equilibrium environment.

7.1 Introduction

The cytoplasm of living cells is full of proteins and organelles that play important active roles with the aid of chemical fuels such as adenosine triphosphate (ATP) [7.1]. In such a non-equilibrium environment, the transport properties of chemical species drastically deviate from those in static equilibrium conditions. For example, there are several experimental works reporting the anomalous diffusion of a tagged particle in biological cells due to protein activities [7.2–7.6]. In other systems, a large enhancement of diffusion was also observed for a passive particle immersed in a bacterial bath [7.7, 7.8] or in a suspension of algae *Chlamydomonas* [7.9], and such a phenomenon has been also studied theoretically [7.10, 7.11].

The modified diffusion in cells was attributed to non-equilibrium forces generated by molecular motors walking on cytoskeletal networks [7.12, 7.13]. Recently, Mikhailov and Kapral proposed a different mechanism caused by non-equilibrium conformational changes of proteins or enzymes [7.14, 7.15]. They showed that, in addition to thermal fluctuations, active proteins in living cells generate non-thermal fluctuating flows that lead to a substantial increment of the diffusion constant. A chemotaxis-like drift of a passive particle was also predicted when a spatial gradient of active proteins is present [7.14, 7.15]. In these previous works, however, the three-dimensional (3D) cytoplasm and two-dimensional (2D) biomembrane were treated as purely viscous fluids characterized by constant shear viscosities [7.16].

In general, biological cells behave as viscoelastic materials [7.17, 7.18]. Hoffman *et al.* experimentally determined the frequency-dependent shear modulus of cultured mammalian cells by using various methods to measure their viscoelastic properties [7.19, 7.20]. Interestingly, they found two universal (weak) power-law dependencies of the shear modulus at low frequencies corresponding to the cortical and intracellular networks. At high frequencies, on the other hand, they observed an exponent of $3/4$ which was attributed to the mechanical response of

actin fibers. Such an universal behavior of mechanical responses in living cells was also reported in other work [7.21].

Among various methods, microrheology is one of the most useful techniques to measure the rheological properties of living cells [7.22–7.26]. In this method, the local and bulk mechanical properties of a single cell can be extracted from a Brownian motion of probe particles, including both thermal and non-thermal contributions [7.27]. Concerning its theoretical background, the generalized Stokes-Einstein relation (GSER), equivalent to the fluctuation dissipation theorem (FDT), has been used to analyze thermal diffusive motions. In non-thermal situations, the GSER has been further extended to relate particle mean squared displacement (MSD) and non-thermal force fluctuations [7.28, 7.29]. It should be noted, however, that the GSER contains various assumptions which can be violated in several situations [7.27]. Therefore it is necessary to discuss both thermal and non-thermal Brownian motions in a viscoelastic medium which is described by a well-founded theoretical model.

In this chapter, I discuss diffusive motion of passive particles embedded in viscoelastic media that is described by the “two-fluid model” for gels [7.30–7.32]. I especially focus on the effects of non-thermal fluctuations induced by active force dipoles which undergo cyclic motions. I calculate displacement cross-correlation functions (CCF) of two point particles for the passive situation induced by thermal fluctuations and the active situation driven by force dipole fluctuations. My calculation is closely related to the “two-point microrheology” method which has several technical advantages compared to the “one-point microrheology” [7.33]. As for the stochastic property of a force dipole, I consider the case when there is no correlation between different times, and also the case when it decays exponentially with a characteristic time scale. If the dipole time scale is much larger than the viscoelastic time scale, I show that the active contribution of the displacement CCF exhibits all the possible crossover behaviors between super-diffusive and sub-diffusive motions. My predictions can be applied not only for

cells but also for bacterial suspensions and systems containing active colloids.

Since my theory is based on the standard two-fluid model, it has some similarities to the works by Levine and Lubensky [7.34, 7.35] or MacKintosh and Levine [7.12, 7.13]. In the former studies [7.34, 7.35], they investigated the dynamics of rigid spheres embedded in viscoelastic media by using the two-fluid model, but did not consider the effects of non-thermal fluctuations. In the latter studies [7.12, 7.13], on the other hand, they developed a model for F-actin networks driven out of equilibrium by molecular motors. The main difference in my work is that active force dipoles are embedded in the fluid and exert forces on the fluid itself. In this regard, I use the partial Green's function that connects the force acting on the fluid and the fluid velocity as discussed in Refs. [7.36, 7.37]. In these works, they emphasized the role of the intermediate length scale in the analysis of microrheology data. In my separate work, starting from the two-fluid model, we have derived effective equations of motions for tracer particles displaying local deformations and local fluid flows [7.38].

In the next section, I describe the two-fluid model and show its partial Green's function both in the Fourier space and the real space. In Sec. 7.3, I discuss the passive two-point correlation functions. Using the coupling mobilities and the FDT in thermal equilibrium, I calculate the power spectral density of the velocity CCFs and the displacement CCFs. In Sec. 7.4, I shall investigate active one-point correlation functions due to active force dipoles. I calculate the active velocity auto-correlation function of a passive point particle by assuming different time correlations of force dipoles. I then discuss in Sec. 7.5 the active two-point correlation functions which are useful for two-point microrheology. The summary of my work and some discussions related to the recent experiments are given in Sec. 7.6.

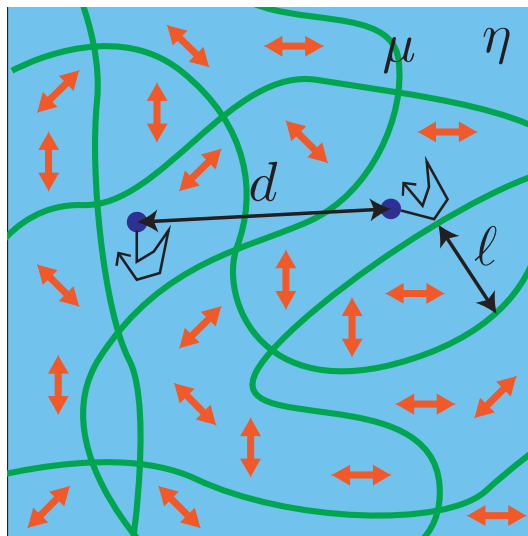


Figure 7.1: Schematic representation of the two-fluid model. The system consists of an elastic network characterized by the Lamé coefficient μ , and a viscous fluid characterized by the shear viscosity η . The elastic and fluid components are coupled through the mutual friction. The length scale ℓ characterizes the typical internal structure of the elastic network. Orange objects represent stochastic force dipoles which are immersed in the fluid component. Two passive point particles separated by a distance d are embedded in the fluid component. These passive particles undergo correlated random Brownian motion due to thermal fluctuations and active stochastic fluctuations induced by active force dipoles.

7.2 Two-fluid model

7.2.1 Model description

To describe viscoelastic media from a general point of view, I employ the two-fluid model that has been broadly used to describe the dynamics of polymer gels [7.30–7.32, 7.39]. As schematically shown in Fig. 7.1, there are two dynamical fields in this model; the displacement field $\mathbf{u}(\mathbf{r}, t)$ of the elastic network and the velocity field $\mathbf{v}(\mathbf{r}, t)$ of the permeating fluid. Here \mathbf{r} is the 3D position vector and t is the time. The coupled dynamical equations for these two field variables are given by

$$\rho_u \frac{\partial^2 \mathbf{u}}{\partial t^2} = \mu \nabla^2 \mathbf{u} + (\mu + \lambda) \nabla (\nabla \cdot \mathbf{u}) - \Gamma \left(\frac{\partial \mathbf{u}}{\partial t} - \mathbf{v} \right) + \mathbf{f}_u, \quad (7.1)$$

$$\rho_v \frac{\partial \mathbf{v}}{\partial t} = \eta \nabla^2 \mathbf{v} - \nabla p - \Gamma \left(\mathbf{v} - \frac{\partial \mathbf{u}}{\partial t} \right) + \mathbf{f}_v. \quad (7.2)$$

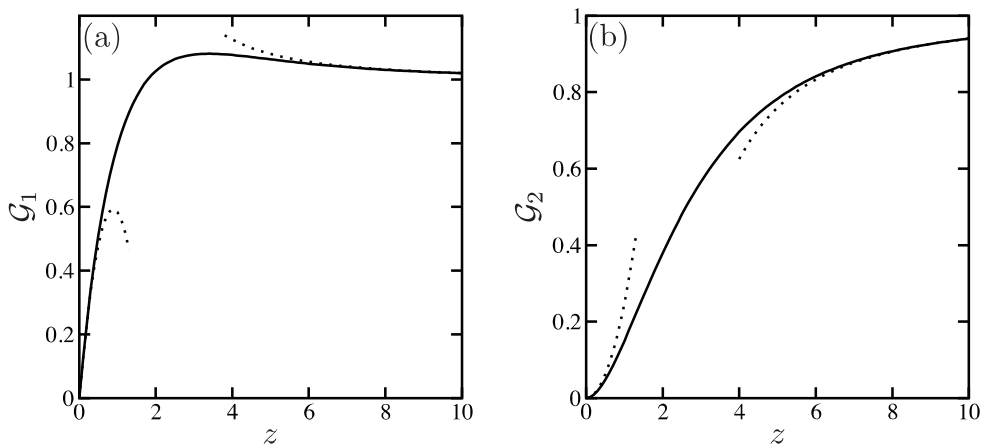


Figure 7.2: Scaling functions (a) \mathcal{G}_1 and (b) \mathcal{G}_2 [see Eq. (7.10) and (7.11), respectively] appearing in the partial Green's function of the two-fluid model. The scaling variable is $z = r/\xi$, where r is the distance and ξ is the frequency-dependent characteristic length scale [see Eq. (7.8)]. The asymptotic behaviors of these scaling functions, as analytically given by Eqs. (7.12) and (7.13), respectively, are plotted with dotted lines.

In the above, ρ_u and ρ_v are the mass densities of the two components, μ and λ are the Lamé coefficients of the elastic network, respectively, η is the shear viscosity of the fluid, $p(\mathbf{r}, t)$ is the pressure field, while \mathbf{f}_u and \mathbf{f}_v are external force densities. The elastic and the fluid components are coupled through the mutual friction characterized by the friction coefficient Γ . We note that μ , λ , η and Γ are constants and do not depend on frequency. When the volume fraction of the network is denoted by ϕ , the above equations are further supplemented by the condition of the total volume conservation

$$\nabla \cdot \left[\phi \frac{\partial \mathbf{u}}{\partial t} + (1 - \phi) \mathbf{v} \right] = 0. \quad (7.3)$$

In the following, I employ several simplifications of the model. (i) I neglect inertial effects, which is justified at sufficiently low frequencies. Hence the l.h.s. of Eqs. (7.1) and (7.2) are both neglected. (ii) I assume that the volume fraction of the network is vanishingly small, i.e., $\phi \ll 1$. In this limit, Eq. (7.3) can be approximated as

$$\nabla \cdot \mathbf{v} \approx 0. \quad (7.4)$$

This equation can be regarded as the incompressibility condition of the fluid component.

7.2.2 Partial Green's function

The above linearized equations can be solved by performing the Fourier transform in space and the Laplace transform in time for any function $f(\mathbf{r}, t)$ as defined by

$$f[\mathbf{q}, s] = \int_{-\infty}^{\infty} d^3r \int_0^{\infty} dt f(\mathbf{r}, t) e^{-i\mathbf{q}\cdot\mathbf{r} - st}. \quad (7.5)$$

Here \mathbf{q} is the 3D wavevector and s the frequency in the Laplace domain. The general Green's function (represented by a 6×6 matrix) connecting \mathbf{u} and \mathbf{v} to \mathbf{f}_u and \mathbf{f}_v was calculated by Levine and Lubensky [7.34, 7.35].

In this chapter, I particularly focus on the response of the fluid velocity \mathbf{v} due to the point force \mathbf{f}_v , and use the partial Green's function defined by

$$v_\alpha[\mathbf{q}, s] = G_{\alpha\beta}[\mathbf{q}, s] f_{v,\beta}[\mathbf{q}, s]. \quad (7.6)$$

Hereafter, the Einstein summation convention over repeated indices is employed. According to Refs. [7.34–7.37], the Green's function is given by

$$G_{\alpha\beta}[\mathbf{q}, s] = \frac{1 + (\eta_b/\eta)\xi^2 q^2}{\eta_b q^2 (1 + \xi^2 q^2)} (\delta_{\alpha\beta} - \hat{q}_\alpha \hat{q}_\beta), \quad (7.7)$$

with $q = |\mathbf{q}|$ and $\hat{\mathbf{q}} = \mathbf{q}/q$ [see Appendix 7.A for a detailed derivation]. In the above, the frequency-dependent bulk viscosity and characteristic length scale are defined by

$$\eta_b = \eta + \frac{\mu}{s}, \quad \xi = \left(\frac{\mu\eta}{s\Gamma\eta_b} \right)^{1/2}, \quad (7.8)$$

respectively. Notice that the above 3×3 matrix is nothing but the part of the general 6×6 matrix [7.35]. In order to study the effects of molecular motors that generate forces in the cytoskeleton, one needs to take into account \mathbf{f}_u as discussed in Refs. [7.12, 7.13] and recently by us [7.38]. I note here that the partial Green's function in Eq. (7.7) does not depend on the compressional Lamé coefficient λ , while it appears in the general 6×6 matrix.

The Green's function in Eq. (7.7) can be inverted back from the Fourier space to the real space (but remaining in the Laplace domain). Following the calculation in the Appendix 7.A, we obtain

$$G_{\alpha\beta}[\mathbf{r}, s] = \frac{1}{8\pi\eta r} \left[\left(1 + \frac{1 - \eta_b/\eta}{\eta_b/\eta} \mathcal{G}_1(r/\xi) \right) \delta_{\alpha\beta} + \left(1 + \frac{1 - \eta_b/\eta}{\eta_b/\eta} \mathcal{G}_2(r/\xi) \right) \hat{r}_\alpha \hat{r}_\beta \right]. \quad (7.9)$$

where $r = |\mathbf{r}|$ and $\hat{\mathbf{r}} = \mathbf{r}/r$. Here we have defined the two scaling functions by

$$\mathcal{G}_1(z) = 1 + \frac{2}{z^2} - 2e^{-z} \left(1 + \frac{1}{z} + \frac{1}{z^2} \right), \quad (7.10)$$

$$\mathcal{G}_2(z) = 1 - \frac{6}{z^2} + 2e^{-z} \left(1 + \frac{3}{z} + \frac{3}{z^2} \right). \quad (7.11)$$

In Fig. 7.2, I plot both $\mathcal{G}_1(z)$ and $\mathcal{G}_2(z)$ as a function of $z = r/\xi$. When $\mathcal{G}_1(z) = \mathcal{G}_2(z) = 0$, the Green's function $G_{\alpha\beta}$ is purely determined by η , whereas it is fully described by η_b when $\mathcal{G}_1(z) = \mathcal{G}_2(z) = 1$.

7.2.3 Asymptotic expressions

Next I discuss the asymptotic behaviors of the partial Green's function and the scaling functions. I first note that the asymptotic expressions of the scaling functions are given by

$$\mathcal{G}_1(z) \approx \begin{cases} 4z/3 - 3z^2/4, & z \ll 1, \\ 1 + 2/z^2, & z \gg 1, \end{cases} \quad (7.12)$$

$$\mathcal{G}_2(z) \approx \begin{cases} z^2/4, & z \ll 1, \\ 1 - 6/z^2, & z \gg 1. \end{cases} \quad (7.13)$$

These asymptotic behaviors are also plotted in Fig. 7.2 by the dotted lines which provide a good approximation especially for $z \gg 1$.

For my later purpose, I focus here on the large scale behavior of the Green's function. For $r \gg \xi$, we obtain

$$G_{\alpha\beta}[\mathbf{r}, s] \approx \frac{1}{8\pi\eta r} \frac{s\tau}{1 + s\tau} (\delta_{\alpha\beta} + \hat{r}_\alpha \hat{r}_\beta) - \frac{\ell^2}{4\pi\eta r^3} \frac{1}{(1 + s\tau)^2} (\delta_{\alpha\beta} - 3\hat{r}_\alpha \hat{r}_\beta), \quad (7.14)$$

where we have introduced the characteristic length and time scales as

$$\ell = (\eta/\Gamma)^{1/2}, \quad \tau = \eta/\mu. \quad (7.15)$$

As argued in Ref. [7.36], the first and the second terms of Eq. (7.14) are proportional to $1/r$ and ℓ^2/r^3 , respectively. The competition between these two terms is characterized by the crossover length ℓ .

7.2.4 Coupling mobilities

In the following sections, I shall consider correlated motions of two point particles embedded in the fluid component. For this purpose, I shall introduce the coupling mobility between the two points $M_{\alpha\beta}[r, s]$ that is directly related to the partial Green's function in Eq. (7.9). Since $G_{\alpha\beta}$ is generally expressed as $G_{\alpha\beta} = C_1\delta_{\alpha\beta} + C_2\hat{r}_\alpha\hat{r}_\beta$, the ‘‘longitudinal’’ and the ‘‘transverse’’ coupling mobilities are given by $M_{xx} = C_1 + C_2$ and $M_{yy} = C_1$, respectively. Hence they are

$$M_{xx}[r, s] = \frac{1}{4\pi\eta r} \left[1 - \frac{\mathcal{G}_1(z) + \mathcal{G}_2(z)}{2(1 + s\tau)} \right], \quad (7.16)$$

$$M_{yy}[r, s] = \frac{1}{8\pi\eta r} \left[1 - \frac{\mathcal{G}_1(z)}{1 + s\tau} \right], \quad (7.17)$$

where $z = r/\xi = (r/\ell)\sqrt{1 + s\tau}$. I shall use these coupling mobilities in order to calculate various correlation functions in the next sections. Since $M_{xy} = 0$ by symmetry, it is sufficient to consider only the above two coupling mobilities [7.36].

7.3 Passive two-point correlation functions

Here I discuss the correlated dynamics of two distinctive passive particles immersed in a viscoelastic gel that is in thermal equilibrium. This situation is relevant to the ‘‘two-point microrheology’’ experiments as discussed before [7.33]. Compared to the ‘‘single-particle microrheology’’ (with the use of a finite size particle), there are several advantages to perform multi-particle microrheology [7.27].

7.3.1 Fluctuation dissipation theorem

Consider a pair of point particles undergoing Brownian motion separated by a distance d as shown in Fig. 7.1 (but without force dipoles). We denote the positions of these two point particles by $\mathbf{R}_1(t) = \mathbf{R}_1 + \Delta\mathbf{R}_1(t)$ and $\mathbf{R}_2(t) = \mathbf{R}_2 + \Delta\mathbf{R}_2(t)$, where $d = |\mathbf{R}_2 - \mathbf{R}_1|$. Then the velocities of these point particles are given by $\mathbf{V}_1(\mathbf{R}_1, t) = \Delta\dot{\mathbf{R}}_1(t)$ and $\mathbf{V}_2(\mathbf{R}_2, t) = \Delta\dot{\mathbf{R}}_2(t)$. The quantities of interest are the velocity cross-correlation function (CCF) $\langle V_{1\alpha} V_{2\alpha'}(t) \rangle_d$, and the displacement CCF $\langle \Delta R_{1\alpha} \Delta R_{2\alpha'}(t) \rangle_d$. Without loss of generality, we define the x -axis to be along the line connecting the two particles, i.e., $\mathbf{R}_2 - \mathbf{R}_1 = d\hat{\mathbf{e}}_x$.

According to the fluctuation dissipation theorem (FDT), the velocity CCFs in thermal equilibrium are related to the coupling mobility in the Laplace domain by [7.27, 7.36]

$$\langle V_{1\alpha} V_{2\alpha'}[s] \rangle_d = k_B T M_{\alpha\alpha'}[r = d, s], \quad (7.18)$$

where k_B is the Boltzmann constant, T the temperature. The power spectral density (PSD) of the passive velocity CCF can be obtained by using the relation

$$\langle V_{1\alpha} V_{2\alpha'}(\omega) \rangle_d = 2\Re \langle V_{1\alpha} V_{2\alpha'}[s = i\omega] \rangle_d, \quad (7.19)$$

where ω is the frequency in the Fourier domain, and \Re indicates the real part.

In Fig. 7.3, I plot the scaled PSDs $\langle V_{1x} V_{2x}(\omega) \rangle_d$ and $\langle V_{1y} V_{2y}(\omega) \rangle_d$ as a function of $\omega\tau$ using the longitudinal and the transverse coupling mobilities obtained in Eqs. (7.16) and (7.17), respectively. Different colors represent different distances, d , between the two points. In Fig. 7.3(a), $\langle V_{1x} V_{2x}(\omega) \rangle_d$ increases for $\omega\tau > \sqrt{2}(\ell/d)$ as $\sim \omega^2$ [see later Eqs. (7.21) and (7.22)], while it saturates for $\omega\tau > 1$. Since $\langle V_{1y} V_{2y}(\omega) \rangle_d$ takes negative values for smaller $\omega\tau$ when $d/\ell = 10$ and 100 , I have plotted its absolute value in Fig. 7.3(b). Notice that in both (a) and (b), the PSDs are scaled by $k_B T / (2\pi\eta d)$, and take the same asymptotic value in the large $\omega\tau$ limit.

The passive displacement CCF in thermal equilibrium as a function of time can be directly obtained by the following inverse Laplace transform of the ve-

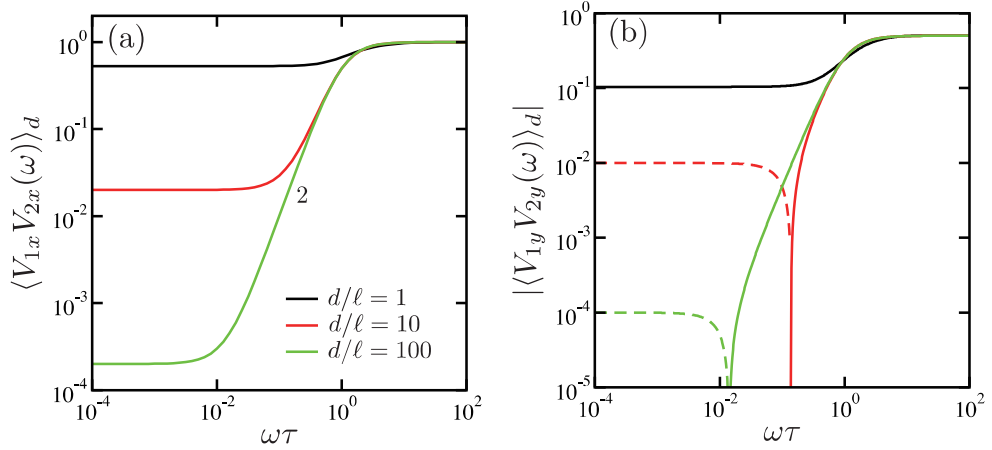


Figure 7.3: The passive component of the power spectral density (PSD) of the two-point velocity cross-correlation functions (CCFs) (a) $\langle V_{1x}V_{2x}(\omega) \rangle_d$ and (b) $|\langle V_{1y}V_{2y}(\omega) \rangle_d|$ [see Eq. (7.19)] as a function of $\omega\tau$ for $d/\ell = 1, 10, 100$. Here $\tau = \eta/\mu$ is the viscoelastic time scale, and d is the distance between the two point particles immersed in viscoelastic media described by the two-fluid model. Both CCFs are scaled by $k_B T/(2\pi\eta d)$ in order to make them dimensionless. Since $\langle V_{1y}V_{2y}(\omega) \rangle_d$ takes negative values for smaller $\omega\tau$ (shown by the dashed lines), I have plotted in (b) its absolute value. The number “2” in (a) indicates the slope representing the exponent of the power-law behaviors.

locity CCF [7.26, 7.27]:

$$\langle \Delta R_{1\alpha} \Delta R_{2\alpha'}(t) \rangle_d = \frac{1}{2\pi i} \int_{c-i\infty}^{c+i\infty} ds \frac{2}{s^2} \langle V_{1\alpha} V_{2\alpha'}[s] \rangle_d e^{st}, \quad (7.20)$$

where c is a real number. Performing the numerical inverse Laplace transform of Eq. (7.20), I plot in Fig. 7.4 the longitudinal and the transverse CCFs $\langle \Delta R_{1x} \Delta R_{2x}(t) \rangle_d$ and $\langle \Delta R_{1y} \Delta R_{2y}(t) \rangle_d$ as a function of t/τ for different distances d between the two points.

In Fig. 7.4(a), the longitudinal CCF is proportional to t for $t/\tau < 1$ and $t/\tau > (d/\ell)^2/2$ [see later Eq. (7.23)]. In the former time region which is smaller than the viscoelastic time scale $\tau = \eta/\mu$, the two point particles interact through the fluid component of the two-fluid model. In the latter long time region, on the other hand, the CCF obeys the normal diffusive behavior as expected for any viscoelastic material with a characteristic relaxation time. Between these crossover time scales, the CCF remains almost constant due to the elastic component that

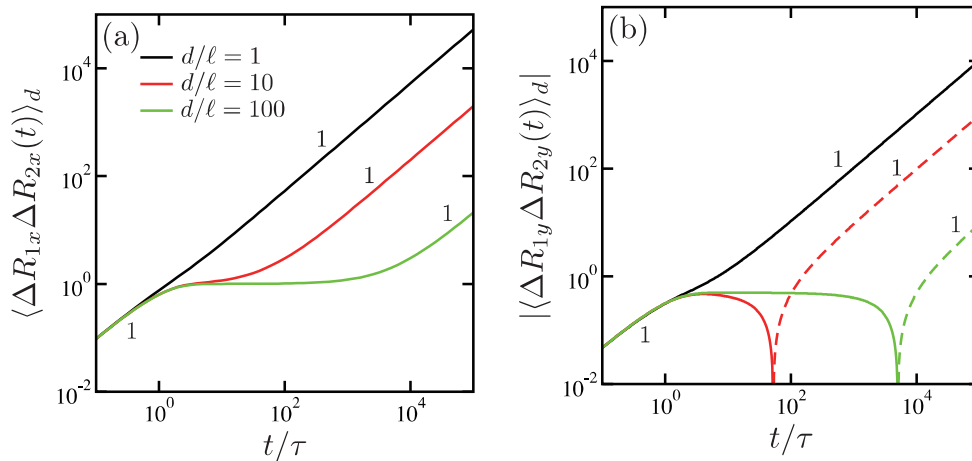


Figure 7.4: The passive component of the two-point displacement cross-correlation functions (CCFs) (a) $\langle \Delta R_{1x} \Delta R_{2x}(t) \rangle_d$ and (b) $|\langle \Delta R_{1y} \Delta R_{2y}(t) \rangle_d|$ [see Eq. (7.20)] as a function of t/τ for $d/\ell = 1, 10, 100$. Here d is the distance between the two point particles immersed in viscoelastic media. Both CCFs are scaled by $k_B T \tau / (2\pi \eta d)$ in order to make them dimensionless. Since $\langle \Delta R_{1y} \Delta R_{2y}(t) \rangle_d$ takes negative values for larger t/τ (shown by the dashed lines), I have plotted in (b) its absolute value. The numbers indicate the slope representing the exponent of the power-law behaviors.

suppresses the motion of the point particles. This is because the elastic property of the medium, representing the polymer network, is pronounced in these time scales. For $d/\ell = 1$, on the other hand, the CCF is almost proportional to t during the entire time region.

In Fig. 7.4(b), the absolute value of $\langle \Delta R_{1y} \Delta R_{2y}(t) \rangle_d$ is plotted because it takes negative values for larger t . This means that the relative transverse motion of the two point particles is anti-correlated when their separation d/ℓ is large enough. Nevertheless, the general time-dependent behavior of the transverse CCF is almost the same as that of the longitudinal one in (a).

The crossover behaviors of the passive displacement CCF for large d/ℓ showing the successive scaling as $t \rightarrow t^0 \rightarrow t$ can explain some of the apparent power-law behaviors of soft matter [7.40] or biological cells [7.20]. It should be noted, however, that the passive displacement CCF in thermal equilibrium exhibits only a sub-diffusive behavior.

7.3.2 Large distance behaviors

In the limit of large distances $d \gg \ell$ between the two points, we can use Eq. (7.14) for the partial Green's function to obtain the PSDs in the Fourier domain as

$$\langle V_{1x}V_{2x}(\omega) \rangle_d \approx \frac{k_B T}{2\pi\eta d} \frac{(\omega\tau)^2}{1 + (\omega\tau)^2} + \frac{k_B T \ell^2}{\pi\eta d^3} \left[\frac{1}{[1 + (\omega\tau)^2]^2} - \frac{(\omega\tau)^2}{[1 + (\omega\tau)^2]^2} \right], \quad (7.21)$$

$$\langle V_{1y}V_{2y}(\omega) \rangle_d \approx \frac{k_B T}{4\pi\eta d} \frac{(\omega\tau)^2}{1 + (\omega\tau)^2} - \frac{k_B T \ell^2}{2\pi\eta d^3} \left[\frac{1}{[1 + (\omega\tau)^2]^2} - \frac{(\omega\tau)^2}{[1 + (\omega\tau)^2]^2} \right]. \quad (7.22)$$

For the large distance behavior of the displacement CCFs, we obtain

$$\langle \Delta R_{1x} \Delta R_{2x}(t) \rangle_d \approx \frac{k_B T \tau}{2\pi\eta d} (1 - e^{-t/\tau}) + \frac{k_B T \tau \ell^2}{\pi\eta d^3} \left[\frac{t}{\tau} (1 + e^{-t/\tau}) - 2(1 - e^{-t/\tau}) \right], \quad (7.23)$$

$$\langle \Delta R_{1y} \Delta R_{2y}(t) \rangle_d \approx \frac{k_B T \tau}{4\pi\eta d} (1 - e^{-t/\tau}) - \frac{k_B T \tau \ell^2}{2\pi\eta d^3} \left[\frac{t}{\tau} (1 + e^{-t/\tau}) - 2(1 - e^{-t/\tau}) \right]. \quad (7.24)$$

In the above expressions, the first term is proportional to t in the short time regime, whereas it saturates in the long time limit. Whereas the second term in each expression is proportional to t in the long time limit, which dominates the large scale behavior. These properties of the displacement CCF can be clearly observed in Fig. 7.4 especially for larger d/ℓ . Although not plotted, Eqs. (7.23) and (7.24) almost completely recover the numerical plots in Fig. 7.4.

7.4 Active one-point correlation functions

In this section, I shall consider the collective advection effects due to active force dipoles on passive particles immersed in viscoelastic media. A simple ‘‘dimer model’’ for a stochastic hydrodynamic force dipole was previously discussed in Refs. [7.14, 7.15]. To investigate the hydrodynamic effects of the force dipoles, I employ the partial Green's function representing the response of the fluid velocity \mathbf{v} due to the force \mathbf{f}_v acting on the fluid component [see Eq. (7.6)].

This is different from Refs. [7.12, 7.13] where they discussed the effects of molecular motors generating forces in the cytoskeleton which corresponds to the elastic component of the two-fluid model. My aim is to focus on the role of active force dipoles that exist in the fluid component. A more unified treatment of these two different sources of active forces has been investigated in my separate publication [7.38].

7.4.1 Velocity induced by active force dipoles

When a point force \mathbf{f}_v is applied to the fluid at a point \mathbf{r} , it induces a fluid velocity at another position \mathbf{R} that advects a point particle located there. As in the previous section, we denote the position of this passive point particle by $\mathbf{R}(t) = \mathbf{R}_0 + \Delta\mathbf{R}(t)$, and its velocity by $\mathbf{V}(\mathbf{R}, t) = \Delta\dot{\mathbf{R}}(t)$. Using the Green's function calculated in Sec. 7.2, we obtain the relation between \mathbf{V} and \mathbf{f}_v as

$$V_\alpha(\mathbf{R}, t) = \int_{-\infty}^t dt' G_{\alpha\beta}(\mathbf{R} - \mathbf{r}, t - t') f_{v,\beta}(\mathbf{r}, t'). \quad (7.25)$$

Consider an oscillating dimer of length $a(t)$ and the force magnitude $f_d(t)$ with its orientation given by the unit vector $\hat{\mathbf{e}}$. In this case, the induced velocity of a passive particle at \mathbf{R} due to the oscillating dimer is given by [7.14]

$$V_\alpha(\mathbf{R}, t) \approx \int_{-\infty}^t dt' \frac{\partial G_{\alpha\beta}(\mathbf{R} - \mathbf{r}, t - t')}{\partial r_\gamma} \hat{e}_\beta \hat{e}_\gamma m(t'), \quad (7.26)$$

where we have used the approximation $a \ll |\mathbf{R} - \mathbf{r}|$, and $m(t) = a(t)f_d(t)$ denotes the magnitude of the force dipole.

I further consider a collection of such active force dipoles, located at positions $\{\mathbf{R}_i\}$ with orientations $\{\hat{\mathbf{e}}_i\}$. By summing up for all the dipoles, the velocity of the passive particle is then given by [7.14]

$$V_\alpha(\mathbf{R}_0, t) \approx \int_{-\infty}^t dt' \int d^3r \frac{\partial G_{\alpha\beta}(\mathbf{r}, t - t')}{\partial r_\gamma} \sum_i \hat{e}_{i,\gamma} \hat{e}_{i,\beta} m_i(t') \delta(\mathbf{R}_i - \mathbf{R}_0 - \mathbf{r}), \quad (7.27)$$

where we have assumed that the displacement of the passive particle is small, and kept only the lowest order term. This equation describes the motion of a passive point particle due to non-thermal active noise arising from the collective

operation of active force dipoles.

Hereafter we introduce the bilateral Fourier transform in time for any function $f(t)$ as

$$f(\omega) = \int_{-\infty}^{\infty} dt f(t)e^{-i\omega t}, \quad (7.28)$$

[cf. Eq. (7.5)]. Performing the bilateral Fourier transform of Eq. (7.27), we obtain

$$V_{\alpha}(\mathbf{R}_0, \omega) \approx \int d^3r \frac{\partial G_{\alpha\beta}[\mathbf{r}, \omega]}{\partial r_{\gamma}} \sum_i \hat{e}_{i,\gamma} \hat{e}_{i,\beta} m_i(\omega) \delta(\mathbf{R}_i - \mathbf{R}_0 - \mathbf{r}), \quad (7.29)$$

where $G_{\alpha\beta}[\mathbf{r}, \omega] = G_{\alpha\beta}[\mathbf{r}, s = i\omega]$. We shall use this expression to calculate the velocity correlation functions and the mean squared displacement (MSD) of the passive particle.

7.4.2 Active auto-correlation functions

I now calculate the velocity auto-correlation function (ACF) of a passive particle located on average at \mathbf{R}_0 . If the correlation between different force dipoles vanishes, i.e., $\langle m_i m_j(\omega) \rangle = \langle m^2(\omega) \rangle \delta_{ij}$, we get from Eq. (7.29)

$$\begin{aligned} & \langle V_{\alpha} V_{\alpha'}(\mathbf{R}_0, \omega) \rangle \\ &= \int d^3r \frac{\partial G_{\alpha\beta}[\mathbf{r}, \omega]}{\partial r_{\gamma}} \frac{\partial G_{\alpha'\beta'}[\mathbf{r}, -\omega]}{\partial r_{\gamma'}} \sum_i \langle \hat{e}_{i,\gamma} \hat{e}_{i,\beta} \hat{e}_{i,\gamma'} \hat{e}_{i,\beta'} \rangle \langle m_i^2(\omega) \rangle \langle \delta(\mathbf{R}_i - \mathbf{R}_0 - \mathbf{r}) \rangle \\ &= \Omega_{\beta\beta'\gamma\gamma'} \langle m^2(\omega) \rangle \int d^3r \frac{\partial G_{\alpha\beta}[\mathbf{r}, \omega]}{\partial r_{\gamma}} \frac{\partial G_{\alpha'\beta'}[\mathbf{r}, -\omega]}{\partial r_{\gamma'}} c(\mathbf{R}_0 + \mathbf{r}), \end{aligned} \quad (7.30)$$

where $c(\mathbf{r}) = \sum_i \langle \delta(\mathbf{R}_i - \mathbf{r}) \rangle$ is the local concentration of force dipoles at a point \mathbf{r} in the fluid component. In the above, a symbol

$$\Omega_{\beta\beta'\gamma\gamma'} = \langle \hat{e}_{\beta} \hat{e}_{\beta'} \hat{e}_{\gamma} \hat{e}_{\gamma'} \rangle = \frac{1}{15} (\delta_{\beta\beta'} \delta_{\gamma\gamma'} + \delta_{\beta\gamma} \delta_{\beta'\gamma'} + \delta_{\beta\gamma'} \delta_{\beta'\gamma}), \quad (7.31)$$

has been defined, and we have assumed that the orientations of active force dipoles are not correlated with their positions. In other words, we do not consider any nematic ordering of force dipoles [7.14].

When active force dipoles are uniformly distributed in space with a constant concentration, $c(\mathbf{r}) = c_0$, the velocity ACF $\langle V_{\alpha} V_{\alpha'}(\omega) \rangle$ is isotropic, i.e., $\langle V_x^2(\omega) \rangle = \langle V_y^2(\omega) \rangle = \langle V_z^2(\omega) \rangle$ and vanishes otherwise. Hence it is enough to

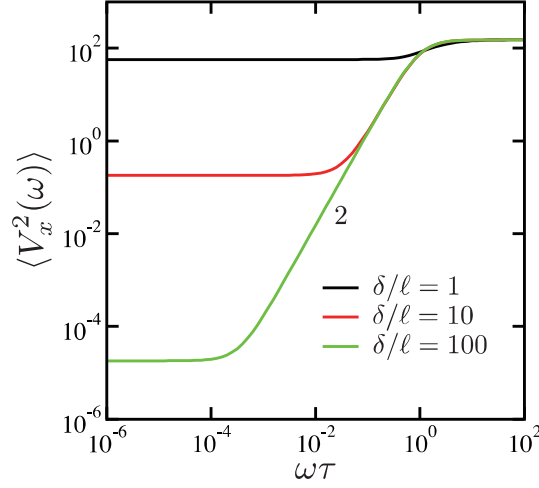


Figure 7.5: The active component of the power spectral density (PSD) $\langle V_x^2(\omega) \rangle$ [see Eq. (7.32)] as a function of $\omega\tau$ for $\delta/\ell = 1, 10, 100$. Here a single point particle is immersed in viscoelastic media described by the two-fluid model, and δ is the cutoff length corresponding to the particle size. In the plot, the PSD is scaled by $c_0 \langle m^2(\omega) \rangle / (2880\pi^2 \eta^2 \delta)$ in order to make it dimensionless. The number indicates the slope representing the exponent of the power-law behavior.

consider only the x -direction, and we obtain the active PSD as

$$\begin{aligned} \langle V_x^2(\omega) \rangle &= \frac{c_0}{3} \Omega_{\beta\beta'\gamma\gamma'} \langle m^2(\omega) \rangle \int d^3r \frac{\partial G_{\alpha\beta}[\mathbf{r}, \omega]}{\partial r_\gamma} \frac{\partial G_{\alpha\beta'}[\mathbf{r}, -\omega]}{\partial r_{\gamma'}} \\ &= \frac{1}{3 \cdot 8^2 \cdot 15\pi^2 \eta^2 \ell} c_0 \langle m^2(\omega) \rangle \mathcal{I}(\omega). \end{aligned} \quad (7.32)$$

Here we have introduced the scaled PSD defined by

$$\mathcal{I}(\omega) = 15\Omega_{\beta\beta'\gamma\gamma'} \int d^3\bar{r} \frac{\partial g_{\alpha\beta}[\mathbf{r}, \omega]}{\partial \bar{r}_\gamma} \frac{\partial g_{\alpha\beta'}[\mathbf{r}, -\omega]}{\partial \bar{r}_{\gamma'}}, \quad (7.33)$$

together with $g_{\alpha\beta}[\mathbf{r}, \omega] = 8\pi\eta\ell G_{\alpha\beta}[\mathbf{r}, s = i\omega]$ and $\bar{r} = r/\ell$. Since the above integral diverges for short length scales, we need to introduce a small cutoff length δ . Physically, δ can be regarded as the size of the passive particle. In Fig. 7.5, I numerically plot the scaled PSD, $\mathcal{I}(\omega)$, as a function of $\omega\tau$ for different cutoff lengths $\delta/\ell = 1, 10$ and 100 . These values correspond to the situation when the passive particle is larger than the mesh size. For $\omega\tau > 2\sqrt{3}(\ell/\delta)^2$, the PSD increases as $\sim \omega^2$ and saturates for $\omega\tau > 1$ [see later Eq. (7.34)]. Note that the asymptotic value of the scaled PSD for large $\omega\tau$ is independent of δ .

If we use Eq. (7.14) for the partial Green's function $G_{\alpha\beta}$ in the large distance

limit $r \gg \ell$, the scaled PSD can be approximately calculated as

$$\mathcal{I}(\omega) \approx 48\pi \left[\frac{(\omega\tau)^2}{1 + (\omega\tau)^2} \left(\frac{\ell}{\delta}\right) - \frac{4(\omega\tau)^2}{[1 + (\omega\tau)^2]^2} \left(\frac{\ell}{\delta}\right)^3 + \frac{12}{[1 + (\omega\tau)^2]^2} \left(\frac{\ell}{\delta}\right)^5 \right]. \quad (7.34)$$

The detailed derivation of this expression is given in the Appendix 7.B. Although not plotted, we have confirmed that Eq. (7.34) perfectly reproduces the curve of $\delta/\ell = 100$ in Fig. 7.5. We should keep in mind, however, that to regard the cutoff length δ as the particle size is only an approximation, and hence the numerical prefactor should not be taken as accurate when we compare with experiments.

7.4.3 Uncorrelated force dipoles

In order to further calculate the active PSD, the statistical property for the time correlation of a force dipole needs to be specified. First I assume that it is only δ -correlated in time and is given by

$$\langle m(t)m(t') \rangle = S\delta(t - t'), \quad (7.35)$$

where S fixes the fluctuation amplitude. In the Fourier representation, this simply means that $\langle m^2(\omega) \rangle = S$. Once we know the active PSD of the velocity ACF, the corresponding MSD of a passive particle in the x -direction can be obtained by the inverse Fourier transform:

$$\langle (\Delta R_x)^2(t) \rangle = \int_{-\infty}^{\infty} \frac{d\omega}{2\pi} \frac{2}{(i\omega)^2} \langle V_x^2(\omega) \rangle e^{i\omega t}. \quad (7.36)$$

In contrast to the inverse Laplace transform in Eq. (7.20), we also take into account the initial condition by including a constant term in the above transformation. In Fig. 7.6(a), I numerically plot the scaled $\langle (\Delta R_x)^2(t) \rangle$ as a function of t/τ for $\delta/\ell = 1, 10$ and 100 . Here the MSD is proportional to t both for short time scales $t/\tau < 1$ and for long time scales $t/\tau > (\delta/\ell)^4/12$ [see later Eq. (7.38)]. For the intermediate time range $1 < t/\tau < (\delta/\ell)^4/12$, on the other hand, the MSD is strongly suppressed due to the elastic component of the two-fluid model, and it remains almost constant.

If we use the asymptotic expression Eq. (7.14) for the partial Green's function

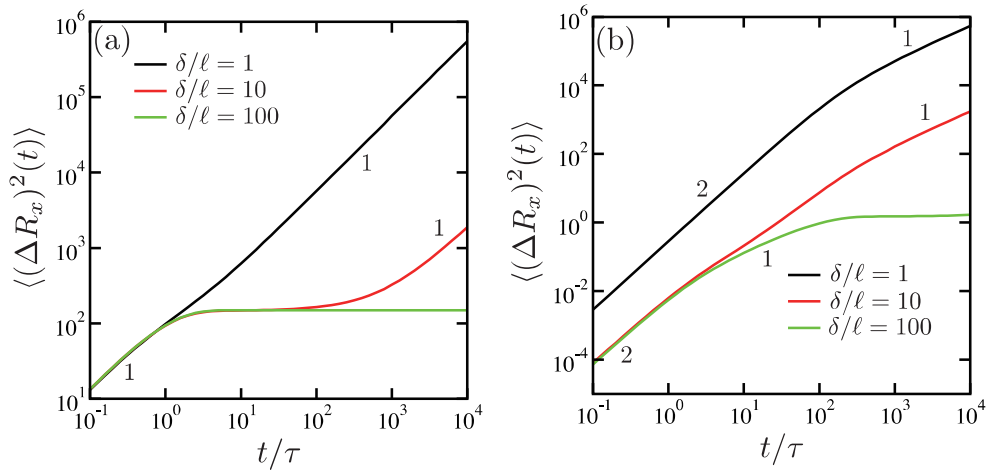


Figure 7.6: The active component of the mean squared displacement (MSD) $\langle(\Delta R_x)^2(t)\rangle$ [see Eq. (7.36)] as a function of t/τ for $\delta/\ell = 1, 10, 100$. Here a single point particle is immersed in viscoelastic media, and δ is the cutoff length. (a) The case when the time correlation of the force dipole is δ -correlated [see Eq. (7.35)]. (b) The case when the time correlation of the force dipole decays exponentially with a characteristic relaxation time τ_d [see Eq. (7.39)], and I set here $\tau_d/\tau = 100$. In these plots, $\langle(\Delta R_x)^2(t)\rangle$ is scaled by $c_0 S \tau / (2880 \pi^2 \eta^2 \delta)$ in order to make it dimensionless. The numbers indicate the slope representing the exponent of the power-law behavior.

as before, the PSD can be obtained from Eqs. (7.32) and (7.34) as

$$\langle V_x^2(\omega) \rangle \approx \frac{1}{60\pi} \frac{c_0 S}{\eta^2 \ell} \left[\frac{(\omega\tau)^2}{1 + (\omega\tau)^2} \left(\frac{\ell}{\delta}\right) - \frac{4(\omega\tau)^2}{[1 + (\omega\tau)^2]^2} \left(\frac{\ell}{\delta}\right)^3 + \frac{12}{[1 + (\omega\tau)^2]^2} \left(\frac{\ell}{\delta}\right)^5 \right]. \quad (7.37)$$

Then, with the use of Eq. (7.36), the asymptotic MSD can be analytically obtained as

$$\langle(\Delta R_x)^2(t)\rangle \approx \frac{1}{60\pi} \frac{c_0 S \tau}{\eta^2 \ell} \left[(1 - e^{-t/\tau}) \left(\frac{\ell}{\delta}\right) + 2[e^{-t/\tau}(t/\tau + 1) - 1] \left(\frac{\ell}{\delta}\right)^3 + 6[e^{-t/\tau}(t/\tau + 3) + 2t/\tau - 3] \left(\frac{\ell}{\delta}\right)^5 \right]. \quad (7.38)$$

The first term in the r.h.s. of the above equation indicates that the normal diffusion occurs for the short time scale $t \ll \tau$, while it saturates in the longer times. In the long time limit, on the other hand, we can set $e^{-t/\tau} \approx 0$, and one finds that MSD is proportional to t for $t \gg (\delta/\ell)^4/12$ [see the third line of Eq. (7.38)], as mentioned above.

7.4.4 Exponentially correlated force dipoles

Next I calculate the PSD and the MSD when the time correlation of a force dipole decays exponentially with a characteristic relaxation time τ_d , i.e.,

$$\langle m(t)m(t') \rangle = \frac{S}{2\tau_d} e^{-|t-t'|/\tau_d}. \quad (7.39)$$

In this case, we have $\langle m^2(\omega) \rangle = S/[1 + (\omega\tau_d)^2]$ in the Fourier representation. Some justification of the above simple expression will be separately discussed in Sec. 7.6. Mathematically, Eq. (7.39) reduces to Eq. (7.35) in the limit of $\tau_d \rightarrow 0$. Then the active PSD is given by

$$\langle V_x^2(\omega) \rangle = \frac{1}{2880\pi^2} \frac{c_0 S}{\eta^2 \ell} \frac{1}{1 + (\omega\tau_d)^2} \mathcal{I}(\omega), \quad (7.40)$$

where $\mathcal{I}(\omega)$ was defined before in Eq. (7.33).

In Fig. 7.6(b), I numerically plot the scaled $\langle (\Delta R_x)^2(t) \rangle$ as a function of t/τ when $\tau_d/\tau = 100$ for $\delta/\ell = 1, 10$ and 100 , i.e., the distance between the two points is larger than the mesh size. For $\delta/\ell = 1$, we find that the active MSD is proportional to t^2 and exhibits a super-diffusive behavior within the time region $t < \tau_d$. For $\delta/\ell = 100$, such a super-diffusive behavior is observed only up to the viscoelastic time scale $t/\tau < 1$, and the MSD exhibits a normal diffusive behavior for $t/\tau > 1$. The active MSD for $\delta/\ell = 100$ is further suppressed for larger time scales. In the very long time limit, the active MSD will be again proportional to t [7.38].

Using the asymptotic expression Eq. (7.14), the active PSD is now given by

$$\langle V_x^2(\omega) \rangle \approx \frac{1}{60\pi} \frac{c_0 S}{\eta^2 \ell} \frac{1}{1 + (\omega\tau_d)^2} \left[\frac{(\omega\tau)^2}{1 + (\omega\tau)^2} \left(\frac{\ell}{\delta}\right) - \frac{4(\omega\tau)^2}{[1 + (\omega\tau)^2]^2} \left(\frac{\ell}{\delta}\right)^3 + \frac{12}{[1 + (\omega\tau)^2]^2} \left(\frac{\ell}{\delta}\right)^5 \right]. \quad (7.41)$$

Then the corresponding active one-point MSD can be obtained up to the lowest order in ℓ/δ as

$$\langle (\Delta R_x)^2(t) \rangle \approx \frac{1}{60\pi} \frac{c_0 S \tau}{\eta^2 \ell} \frac{1}{1 + \tau_d/\tau} \left[1 + \frac{(\tau_d/\tau)e^{-t/\tau_d}}{1 - \tau_d/\tau} - \frac{e^{-t/\tau}}{1 - \tau_d/\tau} \right] \left(\frac{\ell}{\delta}\right). \quad (7.42)$$

This equation reduces to the first line of Eq. (7.38) in the limit of $\tau_d \rightarrow 0$. By

Taylor expanding the above expression for small t , one can indeed show that the linear term in t vanishes, and the active MSD increases as $\sim t^2$. The full expression of the active one-point MSD including higher order terms is provided in the Appendix 7.C. The analytic expressions in Eqs. (7.41) and (7.42) are the general and important results of this chapter.

7.5 Active two-point correlation functions

7.5.1 Velocity cross-correlation functions

In this section, I consider the active velocity CCF between the two points at \mathbf{R}_1 and \mathbf{R}_2 that are separated by a distance d , as shown in Fig. 7.1 and also discussed in Sec. 7.3. With the use of Eq. (7.27), the active two-point velocity CCF can be evaluated by

$$\begin{aligned}
& \langle V_{1\alpha} V_{2\alpha'}(\mathbf{R}_1, \mathbf{R}_2, \omega) \rangle_d \\
&= \int d^3r \frac{\partial G_{\alpha\beta}[\mathbf{r}, \omega]}{\partial r_\gamma} \left(\frac{\partial G_{\alpha'\beta'}[\mathbf{r}', -\omega]}{\partial r'_{\gamma'}} \right)_{\mathbf{r}'=\mathbf{r}-(\mathbf{R}_2-\mathbf{R}_1)} \\
&\times \sum_i \langle \hat{e}_{i,\gamma} \hat{e}_{i,\beta} \hat{e}_{i,\gamma'} \hat{e}_{i,\beta'} \rangle \langle m_i^2(\omega) \rangle \langle \delta(\mathbf{R}_i - \mathbf{R}_1 - \mathbf{r}) \rangle \\
&= \Omega_{\beta\beta'\gamma\gamma'} \langle m^2(\omega) \rangle \int d^3r \frac{\partial G_{\alpha\beta}[\mathbf{r}, \omega]}{\partial r_\gamma} \left(\frac{\partial G_{\alpha'\beta'}[\mathbf{r}', -\omega]}{\partial r'_{\gamma'}} \right)_{\mathbf{r}'=\mathbf{r}-(\mathbf{R}_2-\mathbf{R}_1)} c(\mathbf{R}_1 + \mathbf{r}).
\end{aligned} \tag{7.43}$$

As before, we can generally set $\mathbf{R}_2 - \mathbf{R}_1 = d\hat{\mathbf{e}}_x$ without loss of generality. We also assume that the active force dipoles are uniformly distributed in space with a constant concentration, c_0 . Then one can further rewrite as

$$\langle V_{1\alpha} V_{2\alpha'}(\omega) \rangle_d = \frac{1}{8^2 \cdot 15\pi^2} \frac{c_0}{\eta^2 \ell} \langle m^2(\omega) \rangle \mathcal{I}_{\alpha\alpha'}(d, \omega), \tag{7.44}$$

where

$$\mathcal{I}_{\alpha\alpha'}(d, \omega) = 15\Omega_{\beta\beta'\gamma\gamma'} \int d^3\bar{r} \frac{\partial g_{\alpha\beta}[\mathbf{r}, \omega]}{\partial \bar{r}_\gamma} \left(\frac{\partial g_{\alpha'\beta'}[\mathbf{r}', -\omega]}{\partial \bar{r}'_{\gamma'}} \right)_{\mathbf{r}'=\mathbf{r}-\mathbf{d}}, \tag{7.45}$$

with $g_{\alpha\beta} = 8\pi\eta\ell G_{\alpha\beta}$ as defined before.

In Fig. 7.7, I numerically plot the scaled active PSDs $\langle V_{1x} V_{2x}(\omega) \rangle_d$ and

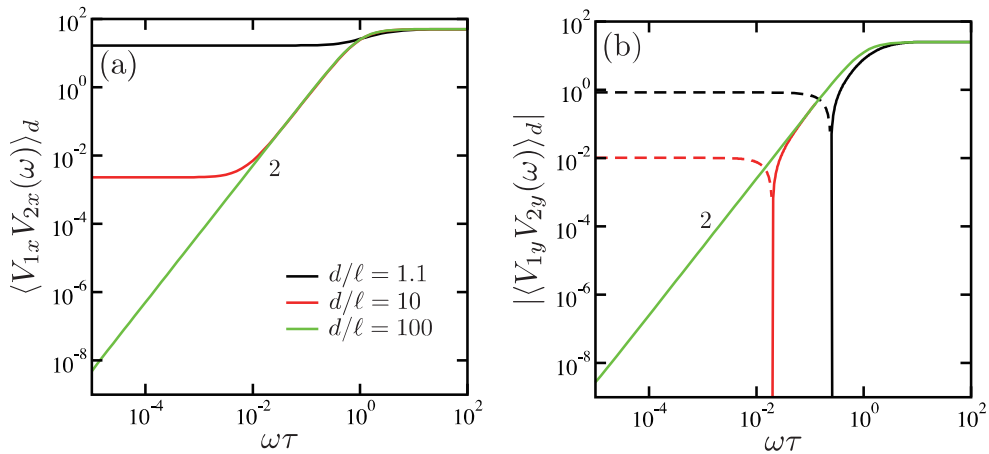


Figure 7.7: The active component of the scaled power spectral density (PSD) (a) $\langle V_{1x}V_{2x}(\omega) \rangle_d$ and (b) $|\langle V_{1y}V_{2y}(\omega) \rangle_d|$ [see Eq. (7.44)] as a function of $\omega\tau$ for $d/\ell = 1.1, 10, 100$. Here d is the distance between the two point particles immersed in viscoelastic media. Both PSDs are scaled by $c_0 \langle m^2(\omega) \rangle / (960\pi^2 \eta^2 d)$ in order to make them dimensionless. Since $\langle V_{1y}V_{2y}(\omega) \rangle_d$ takes negative values for smaller $\omega\tau$ (shown by the dashed lines), I have plotted in (b) its absolute value. The numbers indicate the slope representing the exponent of the power-law behaviors.

$\langle V_{1y}V_{2y}(\omega) \rangle_d$ as a function of $\omega\tau$ for different distances $d/\ell = 1.1, 10$ and 100 , as before. (The reason that we chose here $d/\ell = 1.1$ is that there was a numerical stability issue exactly at $d/\ell = 1$.) The PSD increases as $\sim \omega^2$ for the intermediate frequency range. Within the lowest order term in Eq. (7.14), the asymptotic expressions of the active PSDs can be obtained as

$$\mathcal{I}_{xx}(d, \omega) \approx \frac{16\pi\ell}{d} \frac{(\omega\tau)^2}{1 + (\omega\tau)^2}, \quad (7.46)$$

$$\mathcal{I}_{yy}(d, \omega) = \mathcal{I}_{zz}(d, \omega) \approx \frac{8\pi\ell}{d} \frac{(\omega\tau)^2}{1 + (\omega\tau)^2}. \quad (7.47)$$

7.5.2 Displacement cross-correlation functions

Performing the inverse Fourier transform of the active two-point PSDs as before [see Eq. (7.36)], we obtain the corresponding longitudinal and transverse displacement CCFs $\langle \Delta R_{1x} \Delta R_{2x}(t) \rangle_d$ and $\langle \Delta R_{1y} \Delta R_{2y}(t) \rangle_d$ for the distances $d/\ell = 1.1, 10$ and 100 . In Fig. 7.8(a) and (b), I plot these quantities when the time correlation of a force dipole is δ -correlated as assumed in Eq. (7.35). Fig. 7.8

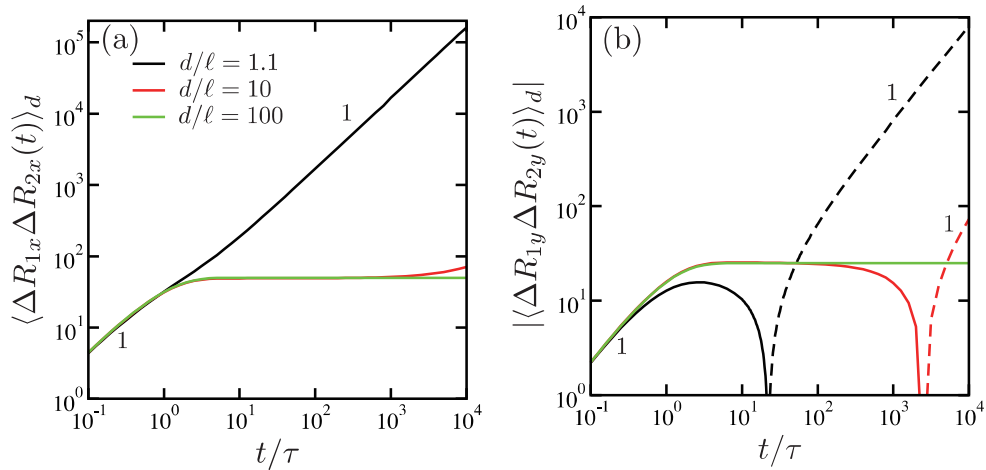


Figure 7.8: The active component of the two-point displacement cross-correlation functions (CCFs) (a) $\langle \Delta R_{1x} \Delta R_{2x}(t) \rangle_d$ and (b) $|\langle \Delta R_{1y} \Delta R_{2y}(t) \rangle_d|$ as a function of t/τ for $d/\ell = 1.1, 10, 100$. Here d is the distance between the two point particles immersed in viscoelastic media, and the time correlation of the force dipole is δ -correlated [see Eq. (7.35)]. Both CCFs are scaled by $c_0 S \tau / (960 \pi^2 \eta^2 d)$ in order to make them dimensionless. Since $\langle \Delta R_{1y} \Delta R_{2y}(t) \rangle_d$ takes negative values for larger t/τ (shown by the dashed lines), I have plotted in (b) its absolute value. The numbers indicate the slope representing the exponent of the power-law behaviors.

should be compared with Fig. 7.6(a) where I have shown the MSD for the active one-point case. Both longitudinal and transverse displacement CCFs are proportional to t for short time scales $t/\tau < 1$ and also for longer time scales. For the intermediate time range, however, these CCFs are strongly suppressed and become constant due to the elastic component of the two-fluid model.

In Fig. 7.9(a) and (b), on the other hand, I consider the case when the time correlation of a force dipole is characterized by a relaxation time $\tau_d/\tau = 100$ [see Eq. (7.39)]. These figures should be compared with Fig. 7.6(b) because the overall behavior is similar. For $\delta/\ell = 1.1$, the active displacement CCFs are proportional to t^2 when $t < \tau_d$, showing a strong super-diffusive behavior. For $\delta/\ell = 100$, however, this super-diffusive behavior is observed only within the time region smaller than the viscoelastic time scale, $t/\tau < 1$, and the CCFs increase as $\sim t$ for $t/\tau > 1$. For much longer time scales, the active CCFs are further suppressed because of the elasticity. In the long time limit, the active

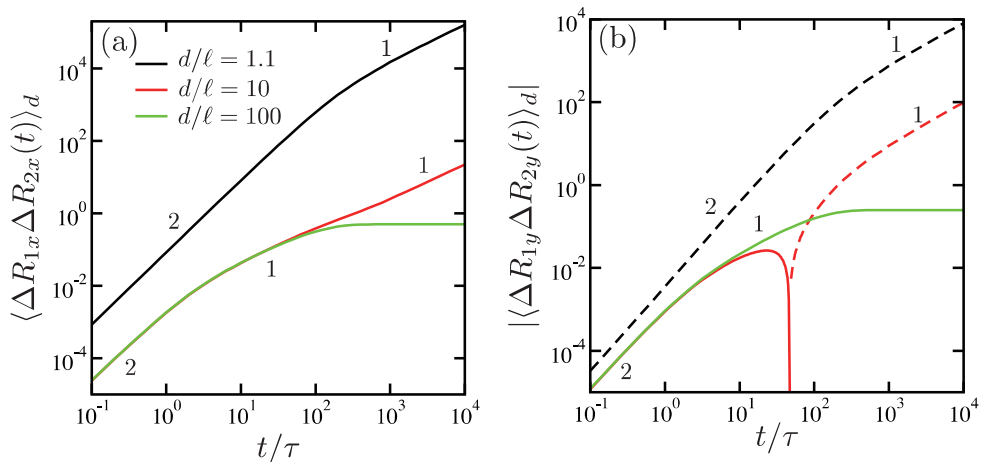


Figure 7.9: The active component of the two-point displacement cross-correlation functions (CCFs) (a) $\langle \Delta R_{1x} \Delta R_{2x}(t) \rangle_d$ and (b) $|\langle \Delta R_{1y} \Delta R_{2y}(t) \rangle_d|$ as a function of t/τ for $d/\ell = 1.1, 10, 100$. Here d is the distance between the two point particles immersed in viscoelastic media. The time correlation of the force dipole decays exponentially with a characteristic relaxation time τ_d [see Eq. (7.39)], and I set here $\tau_d/\tau = 100$. Both CCFs are scaled by $c_0 S \tau / (960 \pi^2 \eta^2 d)$ in order to make them dimensionless. Since $\langle \Delta R_{1y} \Delta R_{2y}(t) \rangle_d$ takes negative values for larger t/τ (shown by the dashed lines), I have plotted in (b) its absolute value. The numbers indicate the slope representing the exponent of the power-law behaviors.

CCFs are both proportional to t .

7.6 Summary and discussion

In this chapter, I have discussed anomalous diffusion induced by active force dipoles in viscoelastic media that is described by the standard two-fluid model for gels. I first reviewed the two-fluid model and showed its partial Green's function both in the Fourier and the real spaces. With the use of the coupling mobilities and the FDT in thermal equilibrium, I have calculated the PSD of the velocity CCFs and the displacement CCFs between the two point particles both for the longitudinal and the transverse directions. The obtained results are useful to interpret the data obtained by two-point microrheology experiments. The passive (thermal) two-point CCF increases linearly with time at shorter and longer time scales, while it is suppressed and remains almost constant at intermediate time scales [see Fig. 7.4].

Moreover, I have calculated active (non-thermal) one-point and two-point correlation functions due to active force dipoles. I have used the relation between the velocity and the dipole strength, as given by Eq. (7.26), and the formulation in Ref. [7.14] in order to further calculate the active PSD of the velocity CCFs. For the one-point case, one needs to introduce a cutoff length scale, δ , in evaluating the integrals, whereas a finite distance, d , between the two point particles plays the role of the cutoff length in the two-point case. As for the statistical property of force dipoles, I considered the case when their magnitude is uncorrelated in time [see Eq. (7.35)] and the case when it decays exponentially with a characteristic time τ_d [see Eq. (7.39)].

For the active case, the important results can be summarized as follows. As shown in Fig. 7.6(b) (one-point case) or Fig. 7.9 (two-point case), I have found that the active MSD or the displacement CCFs exhibits various crossovers from super-diffusive to sub-diffusive behaviors depending on the characteristic time scales ($\tau = \eta/\mu$ and τ_d) and the particle separation d (or the cutoff length δ for the one-point case). I emphasize that the active displacement CCF is proportional to t^2 for time scales shorter than the viscoelastic time scale, $t < \tau$, and it is proportional to t for the intermediate time scales, $\tau < t < \tau_d$. Within the present model, the passive contribution only describes sub-diffusion, whereas the active contribution is responsible for both sub-diffusion and super-diffusion. My results are useful in understanding active properties of the cytoplasm using force spectrum microscopy combined with the microrheology experiment [7.6], as further discussed below.

In Ref. [7.6], Guo *et al.* measured the MSD of microinjected tracer particles in melanoma cells. They showed that the MSD was nearly constant at shorter time scales ($t < 0.1$ s), while it exhibited a slightly super-diffusive behavior at longer time scales ($t > 0.1$ s), i.e., $\langle(\Delta R)^2\rangle \sim t^\beta$ with $\beta \approx 1.2$. However, when they inhibited motor and polymerization activity by depleting cells of ATP, the MSD was almost constant in time, i.e., $\beta \approx 0$. Such an ATP-dependent

Brownian motion was also observed in prokaryotic cells and yeast [7.4, 7.5]. In addition to the MSD measurement, Guo *et al.* performed active microrheology experiment [7.24, 7.25], and found that the frequency-dependent elastic modulus follows a power-law form, i.e., $|G(\omega)| \sim \omega^\alpha$ with $\alpha \approx 0.15$ [7.6].

For simplicity, one may assume that PSD of the active force also obeys a power-law behavior, i.e., $\langle m^2(\omega) \rangle \sim \omega^{-\gamma}$ with a different exponent γ . Among these three exponents, the following scaling relation should hold [7.6, 7.28]:

$$\beta = 2\alpha + \gamma - 1. \quad (7.48)$$

In thermal equilibrium, $\gamma = -\alpha + 1$ holds according to the FDT and hence $\beta = \alpha$. In this case, the anomalous diffusion purely reflects the viscoelasticity of the surrounding media. The exponentially correlated force dipoles in Eq. (7.39) leads to the active PSD in Eq. (7.40), and hence $\gamma = 2$ for $\omega\tau_d \gg 1$. Experimentally, the value $\gamma \approx 2$ was observed by Lau *et al.* [7.28] and later reconfirmed by Guo *et al.* [7.6]. When $\alpha \approx 0.15$ and $\gamma \approx 2$, Eq. (7.48) gives $\beta \approx 1.3$ which is almost consistent with the MSD measurement mentioned above ($\beta \approx 1.2$). In the older experiment [7.28], on the other hand, the measured exponents were $\alpha \approx 0.25$, $\gamma \approx 2$ and hence $\beta \approx 1.5$. In both of these experiments, they claimed that active forces dominate the low-frequency regime, whereas thermal forces dominate the high-frequency regime [7.6, 7.28].

It should be reminded, however, that different values of γ were reported by different groups [7.42–7.44]. For example, a combination of active and passive microrheology measurements using PC3 tumor cells resulted in $\alpha \approx 0.4$, $\beta \approx 1.3$ and $\gamma \approx 1.5$, satisfying also the scaling relation Eq. (7.48). They argued that such a difference can arise because active and passive measurements were done in Ref. [7.28] with different probes and at very different locations in the cell. In Refs. [7.42–7.44], they performed dual passive-active measurements with a unique probe. Given these situations, we consider that the power-law behavior of the force fluctuations and its exponent require further experimental and

theoretical investigations.

I also point out that Eq. (7.48) cannot be always true because the exponents can take values only $0 \leq \beta \leq 2$ and $0 \leq \alpha \leq 1$. Hence, if $\gamma = 2$ holds, one should always observe a super-diffusive behavior because $\beta = 2\alpha + 1 \geq 1$. However, sub-diffusive behaviors ($\beta < 1$) in cells have been observed in many cases [7.45–7.47]. Moreover, the above relation also restricts the value of α to $0 < \alpha \leq 0.5$ because $\beta < 2$, which is not always the case [7.19, 7.20].

In my work, I have assumed that the time correlation of a force dipole is an exponentially decaying function with a characteristic time τ_d , as given in Eq. (7.39). Hence its Fourier transform has a Lorentzian form, and decays as ω^{-2} for $\omega\tau_d \gg 1$. A similar Lorentzian form of force fluctuations was discussed by Levine and MacKintosh [7.12, 7.13]. While some of the experiments which reported the exponent $\gamma = 2$ [7.6, 7.28] justify my assumption, different values of γ found in the other experiments [7.42–7.44] indicate that the dipole correlation cannot be a simple exponentially decaying function. Hence a more detailed investigation for the statistical property of a fluctuating force dipole is required. Currently, I am analyzing the stochastic properties of a simple model of a catalytically active bidomain protein [7.14]. In this model, the two protein domains are represented by beads connected by an elastic spring, and the two internal states, namely, free protein and ligand-protein complex, are assumed.

Although my theory is general and can be applied not only for cells but also for other macroscopic systems, it is useful to give some typical parameter values corresponding to a cell. Since the characteristic length scale $\ell = (\eta/\Gamma)^{1/2}$ roughly corresponds to the mesh size of a polymer gel, it is roughly given by $\ell \sim 10^{-7}$ m for a typical cell. Hence the distance between the two point particles such as $d/\ell = 100$ means $d \sim 10^{-5}$ m. According to Ref. [7.6], I also have $\eta \sim 10^{-3}$ Pa·s and $\mu \sim 1$ Pa so that the viscoelastic time scale can be estimated as $\tau = \eta/\mu \sim 10^{-3}$ s. This means that the dipole time scale $\tau_d/\tau = 100$ used in Figs. 7.6(b) and 7.9 corresponds to $\tau_d \sim 10^{-1}$ s. Although this time scale

is somewhat larger than the cycle time of a single protein machine [7.14], it still gives a good estimate to characterize the collective dynamics of a protein complex.

Recently, Fodor *et al.* [7.48] have made an attempt to theoretically reproduce the MSD data measured in the cytoplasm of living A7 [7.6]. They used one-dimensional Langevin equation in the presence of a random active force to calculate both the thermal and non-thermal MSD. Their theory has a similarity to the present work because they also introduce two time scales which are analogous to $\tau = \eta/\mu$ and τ_d in my theory. An important new aspect in the present chapter is that the internal structure of the viscoelastic medium is properly taken into account. Both thermal and non-thermal MSDs exhibit complicated time sequences depending on the length-scale of the observation relative to the mesh size ℓ . In Ref. [7.48], the size of tracer particles was assumed to be always larger than the mesh size of the cytoskeletal network.

In my separate work, I have considered the two-fluid model where active macromolecules, described as force dipoles, cyclically operate both in the elastic and the fluid components [7.38]. Through coarse-graining, we have derived effective equations of motions for tracer particles displaying local deformations and local fluid flows. The equation for deformation tracers coincides with the phenomenological model by Fodor *et al.* [7.48] (see also the related publication [7.49]). My analysis reveals that localization and diffusion phenomena are generally involved. The motion of tracers immobilized within the elastic subsystem is localized in the long-time limit, but it can show a diffusion-like behavior at the intermediate time scales shorter than the cooperative correlation times of molecular motor aggregates operating in the active gels [7.38].

Recently, Bruinsma *et al.* [7.50] investigated a large scale correlated motion of chromatin inside the nuclei of living cells by using another “two-fluid model” for polymer solutions [7.51] (but not for gels). They derived the response functions that connect the chromatin density and velocity correlation function to

the correlation functions of the active sources that are either scalar or vector quantities. One of the differences in their theory is that the form of the complex viscoelastic moduli needs to be specified in order to compare with experiments, whereas the viscoelasticity naturally arises from the present two-fluid model. It is interesting to note that their active PSD also contains Lorentzian type frequency dependence as I have obtained such as in Eq. (7.40). It would be interesting to calculate the active MSD based on this different two-fluid model.

Finally, I mention that anomalous diffusion observed in colloidal gels has been also explained in terms of force dipoles due to structural inhomogeneities [7.52, 7.53]. Assuming that such inhomogeneities are randomly distributed, it was shown that the relaxation time of the dynamic structure factor is inversely proportional to the wavenumber. In Ref. [7.54], the MSD exhibits diffusive motion at short times and super-diffusive motion at long times.

7.A Partial Green's function

In this appendix, I show the derivation of Eqs. (7.7) and (7.9) [7.34–7.37]. By using the Fourier transform in space and the Laplace transform in time, Eqs. (7.1), (7.2) and (7.4) can be represented in the steady state as

$$0 = -\mu q^2 \mathbf{u}[\mathbf{q}, s] - (\mu + \lambda) \mathbf{q}(\mathbf{q} \cdot \mathbf{u}[\mathbf{q}, s]) - \Gamma (s \mathbf{u}[\mathbf{q}, s] - \mathbf{v}[\mathbf{q}, s]), \quad (7.49)$$

$$0 = -\eta q^2 \mathbf{v}[\mathbf{q}, s] - i \mathbf{q} p[\mathbf{q}, s] - \Gamma (\mathbf{v}[\mathbf{q}, s] - s \mathbf{u}[\mathbf{q}, s]) + \mathbf{f}_v[\mathbf{q}, s], \quad (7.50)$$

$$\mathbf{q} \cdot \mathbf{v}[\mathbf{q}, s] = 0. \quad (7.51)$$

Taking the inner products of both Eqs. (7.49) and (7.50) with \mathbf{q} , and using Eq. (7.51), we obtain

$$p[\mathbf{q}, s] = -\frac{i \mathbf{q} \cdot \mathbf{f}_v[\mathbf{q}, s]}{q^2}. \quad (7.52)$$

From Eq. (7.49), we can solve for \mathbf{u} as

$$u_\alpha[\mathbf{q}, s] = \left(\frac{\Gamma}{\mu q^2 + s\Gamma} \delta_{\alpha\beta} - \frac{\Gamma(\mu + \lambda)q^2}{(\mu q^2 + s\Gamma)(2\mu q^2 + \lambda q^2 + s\Gamma)} \hat{q}_\alpha \hat{q}_\beta \right) v_\beta[\mathbf{q}, s]. \quad (7.53)$$

Substituting Eqs. (7.52) and (7.53) into Eq. (7.50), we obtain the following

equation

$$\left(\frac{q^2[\eta\mu q^2 + (s\eta + \mu)\Gamma]}{\mu q^2 + s\Gamma} \delta_{\alpha\beta} - \frac{s\Gamma^2(\mu + \lambda)q^2}{(\mu q^2 + s\Gamma)(2\mu q^2 + \lambda q^2 + s\Gamma)} \hat{q}_\alpha \hat{q}_\beta \right) v_\beta[\mathbf{q}, s] \\ = (\delta_{\alpha\beta} - \hat{q}_\alpha \hat{q}_\beta) f_{v,\beta}[\mathbf{q}, s]. \quad (7.54)$$

Then we can solve for \mathbf{v} as

$$v_\alpha[\mathbf{q}, s] = \frac{\mu q^2 + s\Gamma}{q^2[\eta\mu q^2 + (s\eta + \mu)\Gamma]} (\delta_{\alpha\beta} - \hat{q}_\alpha \hat{q}_\beta) f_{v,\beta}[\mathbf{q}, s]. \quad (7.55)$$

In terms of η_b and ξ defined in Eq. (7.8), we finally obtain Eq. (7.7).

Next, I derive the real space representation of the partial Green's function [7.41]. I first assume that it has the form of

$$G_{\alpha\beta}[\mathbf{r}, s] = C_1 \delta_{\alpha\beta} + C_2 \hat{r}_\alpha \hat{r}_\beta, \quad (7.56)$$

so that

$$G_{\alpha\alpha}[\mathbf{q}, s] = 3C_1 + C_2, \quad (7.57)$$

$$G_{\alpha\beta}[\mathbf{q}, s] \hat{r}_\alpha \hat{r}_\beta = C_1 + C_2. \quad (7.58)$$

Hence we have

$$3C_1 + C_2 = 2 \int \frac{d^3q}{(2\pi)^3} \frac{1 + (\eta_b/\eta)\xi^2 q^2}{\eta_b q^2 (1 + \xi^2 q^2)} e^{i\mathbf{q}\cdot\mathbf{r}}, \\ = \frac{1}{2\pi\eta r} \left[1 + \frac{1 - \eta_b/\eta}{\eta_b/\eta} (1 - e^{-r/\xi}) \right], \quad (7.59)$$

$$C_1 + C_2 = \int \frac{d^3q}{(2\pi)^3} \frac{1 + (\eta_b/\eta)\xi^2 q^2}{\eta_b q^2 (1 + \xi^2 q^2)} [1 - (\hat{\mathbf{q}} \cdot \hat{\mathbf{r}})^2] e^{i\mathbf{q}\cdot\mathbf{r}} \\ = \frac{1}{4\pi\eta r} \left[1 + \frac{1 - \eta_b/\eta}{\eta_b/\eta} \left(1 - 2(\xi/r)^2 + 2e^{-r/\xi} [(\xi/r) + (\xi/r)^2] \right) \right]. \quad (7.60)$$

Solving for C_1 and C_2 , we finally arrive at Eq. (7.9) with Eqs. (7.10) and (7.11).

7.B Derivation of Eq. (7.34)

In this appendix, I show the derivation of Eq. (7.34). Here I use the dimensionless form of the Green's function $g_{\alpha\beta} = 8\pi\eta\ell G_{\alpha\beta}$, and consider its asymptotic

expression [see Eq. (7.14)]

$$\begin{aligned} g_{\alpha\beta}[\mathbf{r}, \omega] &= \frac{i\omega\tau\ell}{r(1+i\omega\tau)}(\delta_{\alpha\beta} + \hat{r}_\alpha\hat{r}_\beta) - \frac{2\ell^3}{r^3(1+i\omega\tau)^2}(\delta_{\alpha\beta} - 3\hat{r}_\alpha\hat{r}_\beta) \\ &\equiv A_{\alpha\beta}(\mathbf{r}, \omega) - B_{\alpha\beta}(\mathbf{r}, \omega), \end{aligned} \quad (7.61)$$

where we have defined the functions $A_{\alpha\beta}$ and $B_{\alpha\beta}$ in the last equation. The spatial derivatives of these functions with respect to $\bar{r} = r/\ell$ are

$$\frac{\partial}{\partial \bar{r}_\gamma} A_{\alpha\beta}(\mathbf{r}, \omega) = \frac{i\omega\tau}{1+i\omega\tau} \left(\frac{\bar{r}_\alpha\delta_{\beta\gamma} + \bar{r}_\beta\delta_{\alpha\gamma} - \bar{r}_\gamma\delta_{\alpha\beta}}{\bar{r}^3} - 3\frac{\bar{r}_\alpha\bar{r}_\beta\bar{r}_\gamma}{\bar{r}^5} \right), \quad (7.62)$$

$$\frac{\partial}{\partial \bar{r}_\gamma} B_{\alpha\beta}(\mathbf{r}, \omega) = \frac{2}{(1+i\omega\tau)^2} \left(-3\frac{\bar{r}_\alpha\delta_{\beta\gamma} + \bar{r}_\beta\delta_{\alpha\gamma} + \bar{r}_\gamma\delta_{\alpha\beta}}{\bar{r}^5} + 15\frac{\bar{r}_\alpha\bar{r}_\beta\bar{r}_\gamma}{\bar{r}^7} \right). \quad (7.63)$$

Using these results, we can further calculate the following quantities

$$15\Omega_{\beta\beta'\gamma\gamma'} \frac{\partial}{\partial \bar{r}_\gamma} A_{\alpha\beta}(\mathbf{r}, \omega) \frac{\partial}{\partial \bar{r}_{\gamma'}} A_{\alpha\beta'}(\mathbf{r}, -\omega) = 12 \frac{(\omega\tau)^2}{1+(\omega\tau)^2} \bar{r}^{-4}, \quad (7.64)$$

$$15\Omega_{\beta\beta'\gamma\gamma'} \frac{\partial}{\partial \bar{r}_\gamma} A_{\alpha\beta}(\mathbf{r}, \omega) \frac{\partial}{\partial \bar{r}_{\gamma'}} B_{\alpha\beta'}(\mathbf{r}, -\omega) = -72 \frac{i\omega\tau - (\omega\tau)^2}{[1+(\omega\tau)^2]^2} \bar{r}^{-6}, \quad (7.65)$$

$$15\Omega_{\beta\beta'\gamma\gamma'} \frac{\partial}{\partial \bar{r}_\gamma} B_{\alpha\beta}(\mathbf{r}, \omega) \frac{\partial}{\partial \bar{r}_{\gamma'}} A_{\alpha\beta'}(\mathbf{r}, -\omega) = -72 \frac{-i\omega\tau - (\omega\tau)^2}{[1+(\omega\tau)^2]^2} \bar{r}^{-6}, \quad (7.66)$$

$$15\Omega_{\beta\beta'\gamma\gamma'} \frac{\partial}{\partial \bar{r}_\gamma} B_{\alpha\beta}(\mathbf{r}, \omega) \frac{\partial}{\partial \bar{r}_{\gamma'}} B_{\alpha\beta'}(\mathbf{r}, -\omega) = \frac{720}{[1+(\omega\tau)^2]^2} \bar{r}^{-8}. \quad (7.67)$$

Hence the dimensionless PSD in Eq. (7.33) can be obtained as

$$\begin{aligned} \mathcal{I}(\omega) &= 15\Omega_{\beta\beta'\gamma\gamma'} \int d^3\bar{r} \frac{\partial g_{\alpha\beta}[\mathbf{r}, \omega]}{\partial \bar{r}_\gamma} \frac{\partial g_{\alpha\beta'}[\mathbf{r}, -\omega]}{\partial \bar{r}_{\gamma'}} \\ &= 4\pi \int_{\delta/\ell}^{\infty} d\bar{r} \bar{r}^2 \left(12 \frac{(\omega\tau)^2}{1+(\omega\tau)^2} \bar{r}^{-4} - 144 \frac{(\omega\tau)^2}{[1+(\omega\tau)^2]^2} \bar{r}^{-6} + \frac{720}{[1+(\omega\tau)^2]^2} \bar{r}^{-8} \right) \\ &= 48\pi \left[\frac{(\omega\tau)^2}{1+(\omega\tau)^2} \left(\frac{\ell}{\delta} \right) - 4 \frac{(\omega\tau)^2}{[1+(\omega\tau)^2]^2} \left(\frac{\ell}{\delta} \right)^3 + \frac{12}{[1+(\omega\tau)^2]^2} \left(\frac{\ell}{\delta} \right)^5 \right]. \end{aligned} \quad (7.68)$$

Hence we finally obtain Eq. (7.34).

7.C Full expression of Eq. (7.42)

The full expression of Eq. (7.42) including higher order terms in ℓ/δ is given as follows

$$\begin{aligned}
& \langle (\Delta R_x)^2(t) \rangle \\
& \approx \frac{1}{60\pi} \frac{c_0 S \tau}{\eta^2 \ell} \left[\left(\frac{1}{1 + \tau_d/\tau} + \frac{(\tau_d/\tau) e^{-t/\tau_d}}{1 - (\tau_d/\tau)^2} - \frac{e^{-t/\tau}}{1 - (\tau_d/\tau)^2} \right) \left(\frac{\ell}{\delta} \right) \right. \\
& + \left(\frac{[-2(t/\tau)(\tau_d/\tau)^2 + 2t/\tau - 6(\tau_d/\tau)^2 + 2] e^{-t/\tau}}{[1 - (\tau_d/\tau)^2]^2} + \frac{4(\tau_d/\tau)^3 e^{-t/\tau_d}}{[1 - (\tau_d/\tau)^2]^2} \right. \\
& \left. \left. - \frac{2(2\tau_d/\tau + 1)}{[1 + \tau_d/\tau]^2} \right) \left(\frac{\ell}{\delta} \right)^3 \right. \\
& + \left(\frac{6[-(t/\tau)(\tau_d/\tau)^2 + t/\tau - 5(\tau_d/\tau)^2 + 3] e^{-t/\tau}}{[1 - (\tau_d/\tau)^2]^2} + \frac{12(\tau_d/\tau)^5 e^{-t/\tau_d}}{[1 - (\tau_d/\tau)^2]^2} \right. \\
& \left. \left. - \frac{6[2(\tau_d/\tau)^3 + 4(\tau_d/\tau)^2 + 6\tau_d/\tau + 3]}{[1 + \tau_d/\tau]^2} + \frac{12t}{\tau} \right) \left(\frac{\ell}{\delta} \right)^5 \right]. \tag{7.69}
\end{aligned}$$

References

- [7.1] B. Alberts, A. Johnson, P. Walter, J. Lewis, and M. Raff, *Molecular Biology of the Cell* (Garland Science, New York, 2008).
- [7.2] C. P. Brangwynne, G. H. Koenderink, F. C. MacKintosh, and D. A. Weitz, *J. Cell Biol.* **183**, 583 (2008).
- [7.3] F. C. MacKintosh, *Proc. Nat. Acad. Sci. USA* **109**, 7138 (2012).
- [7.4] S. C. Weber, A. J. Spakowitz, and J. A. Theriot, *Proc. Nat. Acad. Sci. USA* **109**, 7338 (2012).
- [7.5] B. R. Parry, I. V. Surovtsev, M. T. Cabeen, C. S. O'Hern, E. R. Dufresne, and C. Jacobs-Wagner, *Cell* **156**, 183 (2014).
- [7.6] M. Guo, A. J. Ehrlicher, M. H. Jensen, M. Renz, J. R. Moore, R. D. Goldman, J. Lippincott-Schwartz, F. C. MacKintosh, and D. A. Weitz, *Cell* **158**, 822 (2014).

- [7.7] X.-L. Wu and A. Libchaber, *Phys. Rev. Lett.* **84**, 3017 (2000).
- [7.8] D. T. N. Chen, A. W. C. Lau, L. A. Hough, M. F. Islam, M. Goulian, T. C. Lubensky, and A. G. Yodh, *Phys. Rev. Lett.* **99**, 148302 (2007).
- [7.9] K. C. Leptos, J. S. Guasto, J. P. Gollub, A. I. Pesci, and R. E. Goldstein, *Phys. Rev. Lett.* **103**, 198103 (2009).
- [7.10] Y. Hatwalne, S. Ramaswamy, M. Rao, and R. A. Simha, *Phys. Rev. Lett.* **92**, 118101 (2004).
- [7.11] P. T. Underhill and M. D. Graham, *Phys. Fluids* **23**, 121902 (2011).
- [7.12] F. C. MacKintosh and A. J. Levine, *Phys. Rev. Lett.* **100**, 018104 (2008).
- [7.13] A. J. Levine and F. C. MacKintosh, *J. Phys. Chem. B* **113**, 3820 (2009).
- [7.14] A. S. Mikhailov and R. Kapral, *Proc. Nat. Acad. Sci. USA* **112**, E3639 (2015).
- [7.15] R. Kapral and A. S. Mikhailov, *Physica D* **318**, 100 (2016).
- [7.16] Y. Koyano, H. Kitahata, and A. S. Mikhailov *Phys. Rev. E* **94**, 022416 (2016).
- [7.17] B. Fabry, G. N. Maksym, J. P. Butler, M. Glogauer, D. Navajas, and J. J. Fredberg, *Phys. Rev. Lett.* **87**, 148102 (2001).
- [7.18] P. Kollmannsberger and B. Fabry, *Annu. Rev. Mater. Res.* **41**, 75 (2011).
- [7.19] B. D. Hoffman, G. Massiera, K. M. Van Citters, and J. C. Crocker, *Proc. Nat. Acad. Sci. USA* **103**, 10259 (2006).
- [7.20] B. D. Hoffman and J. C. Crocker, *Annu. Rev. Biomed. Eng.* **11**, 259 (2009).
- [7.21] X. Trepatt, L. Deng, S. S. An, D. Navajas, D. J. Tschumperlin, W. T. Gerthoffer, J. P. Butler, and J. J. Fredberg, *Nature* **447**, 592 (2007).

-
- [7.22] T. G. Mason and D. A. Weitz, *Phys. Rev. Lett.* **74**, 1250 (1995).
- [7.23] T. G. Mason, K. Ganesan, J. H. van Zanten, D. Wirtz, and S. C. Kuo, *Phys. Rev. Lett.* **79**, 3282 (1997).
- [7.24] F. Gittes, B. Schnurr, P. D. Olmsted, F. C. MacKintosh, and C. F. Schmidt, *Phys. Rev. Lett.* **79**, 3286 (1997).
- [7.25] B. Schnurr, F. Gittes, F. C. MacKintosh, and C. F. Schmidt, *Macromolecules* **30**, 7781 (1997).
- [7.26] T. G. Mason, *Rheol. Acta* **39**, 371 (2000).
- [7.27] T. M. Squires and T. G. Mason, *Annu. Rev. Fluid Mech.* **42**, 413 (2010).
- [7.28] A. W. C. Lau, B. D. Hoffman, A. Davies, J. C. Crocker, and T. C. Lubensky, *Phys. Rev. Lett.* **91**, 198101 (2003).
- [7.29] A. W. C. Lau and T. C. Lubensky, *Phys. Rev. E* **80**, 011917 (2009).
- [7.30] P. G. de Gennes, *Macromolecules* **9**, 587 (1976).
- [7.31] P. G. de Gennes, *Macromolecules* **9**, 594 (1976).
- [7.32] F. Brochard and P. G. de Gennes, *Macromolecules* **10**, 1157 (1977).
- [7.33] J. C. Crocker, M. T. Valentine, E. R. Weeks, T. Gisler, P. D. Kaplan, A. G. Yodh, and D. A. Weitz, *Phys. Rev. Lett.* **85**, 888 (2000).
- [7.34] A. J. Levine and T. C. Lubensky, *Phys. Rev. Lett.* **85**, 1774 (2000).
- [7.35] A. J. Levine and T. C. Lubensky, *Phys. Rev. E* **63**, 041510 (2001).
- [7.36] A. Sonn-Segev, A. Bernheim-Groswasser, H. Diamant, and Y. Roichman, *Phys. Rev. Lett.* **112**, 088301 (2014).
- [7.37] A. Sonn-Segev, A. Bernheim-Groswasser, and Y. Roichman, *Soft Matter* **10**, 8324 (2014).

- [7.38] K. Yasuda, R. Okamoto, S. Komura, and A. S. Mikhailov, *EPL* **117**, 38001 (2017).
- [7.39] H. Diamant, *Eur. Phys. J. E* **38**, 32 (2015).
- [7.40] D. T. N. Chen, Q. Wen, P. A. Janmey, J. C. Crocker, and A. G. Yodh, *Annu. Rev. Condens. Matter Phys.* **1**, 301 (2010).
- [7.41] M. Doi and S. F. Edwards, *The Theory of Polymer Dynamics*, (Clarendon Press, Oxford, 1986).
- [7.42] C. Wilhelm, *Phys. Rev. Lett.* **101**, 028101 (2008).
- [7.43] F. Gallet, D. Arcizet, P. Bohec, and A. Richert, *Soft Matter* **5**, 2947 (2009).
- [7.44] D. Robert, T.-H. Nguyen, F. Gallet, and C. Wilhelm, *PLoS ONE* **5**, e10046 (2010).
- [7.45] I. M. Tolić-Nørrelykke, E.-L. Munteanu, G. Thon, L. Oddershede, and K. Berg-Sørensen *Phys. Rev. Lett.* **93**, 078102 (2004).
- [7.46] I. Golding and E. C. Cox, *Phys. Rev. Lett.* **96**, 098102 (2006).
- [7.47] S. C. Weber, A. J. Spakowitz, and J. A. Theriot, *Phys. Rev. Lett.* **104**, 238102 (2010).
- [7.48] É. Fodor, M. Guo, N. S. Gov, P. Visco, D. A. Weitz, and F. van Wijland, *EPL* **110**, 48005 (2015).
- [7.49] É. Fodor, W. W. Ahmed, M. Almonacid, M. Bussonnier, N. S. Gov, M.-H. Verlhac, T. Betz, P. Visco, and F. van Wijland, *EPL* **116**, 30008 (2016).
- [7.50] R. Bruinsma, A. Y. Grosberg, Y. Rabin, and A. Zidovska, *Biophys. J.* **106**, 1871 (2014).
- [7.51] M. Doi and A. Onuki, *J. Phys. II (France)* **2**, 1631 (1992).

-
- [7.52] L. Cipelletti, S. Manley, R. C. Ball, and D. A. Weitz, *Phys. Rev. Lett.* **84**, 2275 (2000).
- [7.53] A. Duri and L. Cipelletti, *EPL* **76**, 972 (2006).
- [7.54] Y. Gao, J. Kima, and M. E. Helgeson, *Soft Matter* **11**, 6360 (2015).

Chapter 8

Concluding Remarks

In Chap. 1, I explained the general background of micromachines. Micromachines mean small machines such as motor proteins, metabolic enzymes, and bacteria. In the concept of Micromachine, their universal physicochemical properties are attracting attention. In discussing micromachines, non-equilibrium statistical mechanics plays an important role in dealing with non-equilibrium fluctuations. In addition, micromachines often function in fluids, and the effects of fluids need to be examined in detail. Among micromachines, the concept of microswimmers that swim in fluid has also been actively studied in recent years.

To summarize Chap. 2, I have discussed the Najafi–Golestanian three-sphere swimmer in the homogeneous viscoelastic fluids. I calculated the frequency dependence of the average swimming speed with the complex shear viscosity of the surrounding viscoelastic medium. Here the viscous contribution can exist only when the time-reversal symmetry of the swimmer is broken, whereas the elastic contribution is present only if its structural symmetry is broken. Even though the argument in Chap. 2 is restricted to the artificial three-sphere swimmer, I expect that my basic concept can still be applied to more complex biological processes such as the motion of bacteria, flagellated cellular swimming, and the beating of cilia. Since most of these phenomena take place in a viscoelastic environment, I hope that the concept of my new active microrheology will be used

in the future to reveal their mechanical and dynamical properties.

In summary of Chap. 3, I have proposed a model of 2D three-disk micro-machine swimming in a quasi-2D supported membrane. In particular, I have obtained the average swimming velocity as a function of the disk size and the arm length. Due to the presence of the hydrodynamic screening length in the quasi-2D fluid, κ^{-1} , the geometric factor in the average velocity exhibits various asymptotic behaviors depending on the microswimmer size and the screening length. My result has been confirmed by the scaling argument for the geometric factor.

In Chap. 4, I discussed the locomotion of a three-sphere microswimmer in a viscoelastic structured fluid with typical length and time scales. We derived a general expression for the average swimming velocity, which includes both viscous and elastic contributions. To illustrate our result, we used the two-fluid model for a polymer gel and demonstrated that the average velocity exhibits various asymptotic behaviors depending on the swimmer size. The importance of our work is not restricted to these specific models. The prediction of the average velocity is applicable to any structured viscoelastic fluid that has an intermediate length scale and a characteristic time scale.

To summarize Chap. 5, I have discussed the locomotion of a generalized three-sphere microswimmer in which the spheres are connected by two elastic springs and the natural length of each spring is assumed to undergo a prescribed cyclic change. I have analytically obtained the average swimming velocity \bar{V} as a function of the frequency Ω of cyclic change in the natural length. In the low-frequency region, the swimming velocity increases with frequency and reduces to the original three-sphere model by Najafi and Golestanian. Conversely, in the high-frequency region, the velocity decreases with increasing frequency.

In Chap. 6, I have discussed a cyclic state transition of a micromachine driven by a chemical reaction. I have proposed a minimum model to evaluate the state cyclone to quantify the functionality of a general micromachine. My model in-

cludes the reaction variable θ and the state variable s_i which are coupled to each other through the free energy. The tilted periodic potential for θ is characterized by the nonequilibrium force F and the energy barrier A . In the analysis, I have assumed that θ obeys a deterministic stepwise dynamics characterized by the mean first passage time τ_p and the mean first transition path time τ_t . Calculating the state cyclone analytically, we obtain the scaling relation $C_{12} \sim (\gamma\tau_t)^2$ for $\tau_t/\tau_p \ll 1$. In the small coupling limit, I have further obtained τ_p and τ_t in terms of the potential parameters.

In Chap. 7, I have discussed anomalous diffusion induced by active force dipoles in viscoelastic media that is described by the standard two-fluid model for gels. The passive (thermal) two-point CCF increases linearly with time at shorter and longer time scales, while it is suppressed and remains almost constant at intermediate time scales. For the active case, I have found that the active MSD or the displacement CCFs exhibits various crossovers from super-diffusive to sub-diffusive behaviors depending on the characteristic time scales and the particle separation d .

The research in this thesis has been consistently conducted using minimum model of a micromachine. By considering the minimum structure of a micromachine, the structure that exists universally in the micromachine is extracted. Specifically, in Chaps. 2–5, the universal properties are extracted by using a three-sphere swimmer model, which is one of the minimum models of microswimmers. In Chap. 6, I examined a minimum model constructed with the minimum variables to represent the state cycle. In Chap. 7, I adopted a minimum model called force-dipole as a model of a micromachine that causes non-equilibrium fluctuations. Through research using the minimum model as described above, I aimed to clarify the universal properties of micromachines.